# POLITECNICO DI TORINO

Corso di Laurea in Ingegneria Biomedica

Tesi di Laurea Magistrale

## Effect Of The Presence Of Different Surface Patterns And Microstructures At The Micro And Nanoscale On The Biological Response Of Titanium Alloys


**Relatori:**

Prof.ssa Silvia Spriano
Dott.ssa Sara Ferraris

**Candidata:**

Laura Lochi

**Tutor:**

Dr.techn. Fernando Gustavo Warchomicka

*Institute of Materials Science, Joining and Forming*
*Graz University of Technology*


**Ottobre 2018**

# INTRODUCTION

This thesis work is aimed at studying the effect of microstructure and the micro and nano topography, obtained on Titanium alloy surfaces by means of Electron Beam structuring, on the behavior of primary Human Gingival Fibroblast (HGFs), and *Staphylococcus aureus* (SA, commercial, multi-drug resistant, ATCC 43300). Ti6Al4V, Ti15Mo and CP Titanium (grade2) were investigated as substrates.

The first part of the work was carried out at the Institute of Materials Science, Joining and Forming (IMAT-TUGraz) in Graz, for the production of oriented micro-grooves on substrates of Ti6Al4V, Ti15Mo and Tigrade2.
The techniques used to create superficial microtopography was the Electron Beam structuring, while thermal treatments (using different heating temperatures, heating and cooling rates) were employed to obtain different micro and nanostructures, and etching treatment (HF) was used to create superficial nanotopographies. Through these techniques, samples with different surfaces characteristics were produced.

A first characterization of the samples surfaces and cross sections was performed at IMAT-TUGraz by means of Field Emission Scanning Electron Microscope (FESEM).

The second part of the work was carried out at the Politecnico di Torino (Dipartimento di Scienza Applicata e Tecnologia-DISAT), in order to characterize the surface of the samples. A complete characterization was performed on the Ti6Al4V samples. The samples surface were observed by using FESEM and light optical microscope, and then surface wettability was tested by contact angle measurements (water), crystalline phases and roughness were investigated by means of XRD and surface profile measurements.

At last, biological tests (in collaboration with Eastern Piedmont University) were performed focusing on the influence of different surface treatments on cell and bacterial behavior.
Cell and bacterial cultures were then performed by using Gingival Fibroblast (HGFs) and *Staphylococcus aureus* (SA, commercial, multi-drug resistant, ATCC 43300). The viability of both was evaluated through AlamarBlue test and CFU count method, while cells and bacteria morphology was observed using fluorescent microscope and FESEM.

## BIOMATERIAL

The term biomaterial was first defined in 1987 by Williams [1], as *"non-viable material used in a medical device, intended to interact with biological systems"*. Subsequently, the term has evolved over the past 30 years, and biomaterials are nowadays defined as "*materials intended to interface with biological systems to evaluate, treat, argument or replace any tissue or function of the body*" [2].

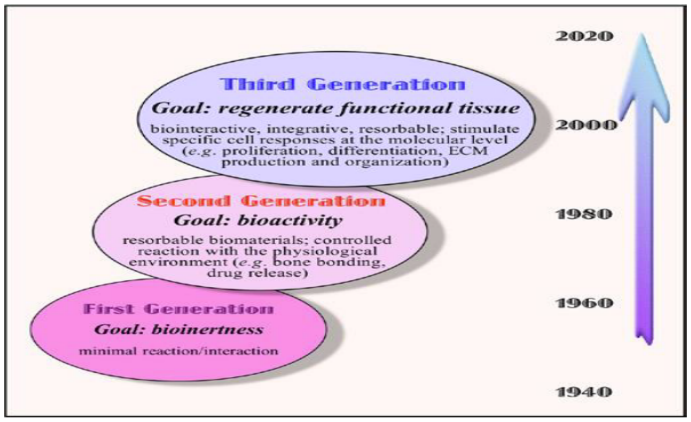


***Fig.1.1*** *Evolution of biomaterial [3].*

- The *first generation* includes materials that were not developed specifically for medical uses but showed interesting mechanical properties and were bioinert, that is they induced a minimal response from the host tissues, and therefore they were considered biocompatible.
- The *second generation* of biomaterials improved the characteristics of the first generation ones (resorbable materials are also included) and present themselves as bioactive. They were capable to induce a controlled reaction and specific therapeutic effects in the host tissues.
- The *third generation* of biomaterials presents the ability to support and stimulate tissue regeneration Fig.1.1.

The ideal biomaterial for bone contact applications must show the following characteristics:

- biocompatibility in order to avoid adverse tissue reactions
- excellent resistance to degradation
- good resistance to cyclic loads

- low elastic modulus in order to avoid bone resorption
- high wear resistance (if employed under wear or fretting conditions). [4]

Biomaterials used for medical applications can be divided into the following categories (Fig.1.2):

- Polymers (PMMA for contact lenses, UHMWPE for polyethylene liner in hip prosthetic,…).
- Metals (stainless steels, cobalt base alloys, titanium and titanium alloys).
- Glasses, glass-ceramic and ceramics (alumina Al2O3, zirconia ZrO2, alumina-zirconia composites, hydroxyapatite).
- Biological materials (allogeneic, autologous and heterologous material). [4]

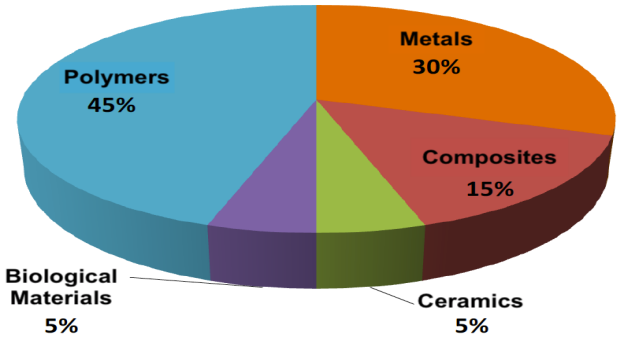


***Fig.1.2*** *Biomaterials categories [5].*

## METALS IN BIOMEDICAL APPLICATIONS

Metals and their alloys are widely used as biomedical materials (especially in orthopedic and dental implants), because of their good mechanical properties that can't be achieved by ceramics or polymers nowadays. It is estimated that 70%–80% of biomedical implants are made of metallic materials [6]. Among metallic biomaterials, stainless steels, Co-Cr alloys, commercially pure titanium and its alloys are extensively employed for their excellent mechanical properties. Nevertheless metals are subject to corrosion, although they form a passive surface film, therefore they sometimes show toxicity because of the release of incompatible metal ions that can cause inflammation or allergic reactions in the human body [7].

Metallic implants must possess excellent key properties, including high wear resistance (if employed under wear or fretting conditions), suitable mechanical properties, excellent biocompatibility, high corrosion resistance and promote osseointegration when employed in bone contact applications [8].

Table 1.1 shows the advantages and disadvantages of metals used in the biomedical field.

| | *Stainless steel* | *Co base alloys* | *Ti and Ti alloys* |
|---|---|---|---|
| *Advantages* | Cost, availability<br>Biocompatibility<br>Processing | Wear resistance<br>Corrosion resistance<br>Fatigue strenght | Biocompatibility<br>Corrosion resistance<br>Minimum Young's modulus<br>Fatigue strenght |
| *Disadvantages* | Long term corrosion behaviour<br>High Young's modulus | High Young's modulus<br>No biocompatibility of ions or released particles | Poor wear resistance<br>Low shear strenght |

***Tab. 1.1*** *Advantages and disadvantages of metals used in biomedical field [8].*

Another important aspect to be taken into account is the mechanical performance of the metal at the interface between the implant and the bone. It's desirable that the Young's modulus of the implant material be similar to bone to avoid the "stress shielding effect" [8]. This allows to have a better stress transmission between the bone and the implant and to avoid bone resorption.

Table 1.2 reports the Young modulus and the ultimate tensile strength of cortical bone compared to some metals used in biomedical applications. It is possible to observe how the elastic modulus of titanium alloys, although it is greater, is the one that comes closest to the elastic modulus of cortical bone.

| Materials | Young's Modulus [Gpa] | Ultimate Tensile Strenghth |
|---|---|---|
| CoCrMo alloys | 240 | 900-1540 |
| 316L stainless steel | 200 | 540-1000 |
| Ti alloys | 78-125 | 900 |
| Cortical bone | 10-30 | 130-150 |

***Tab. 1.2*** *Young's Modulus and UTS of the principal metals used in biomedical filed compared with those of the cortical bone.*

## THE IMPORTANCE OF TITANIUM AND ITS ALLOYS IN MEDICAL APPLICATIONS

Among metallic materials, titanium and its alloys are considered as the most suitable materials for biomedical applications for their superior properties that satisfy the mechanical requirements (stiffness, strength, fracture toughness, fatigue strength, corrosion resistance) and the biological requirements (biocompatibility, negligible ion release) [9] [10] of implantation materials listed above, better than other competing materials, such as stainless steels, Cr-Co alloys, CP niobium and tantalum [11]. However titanium presents low shear strength and wear/fretting resistance [9].

# TITANIUM AND ITS ALLOYS

Titanium was discovered in 1791 by the mineralogist and chemist William Gregor, examining the magnetic sand from the local river Helford, in Cornwall, England.

Titanium is the fourth most abundant structural metal in Earth exceeded only by aluminum, iron and magnesium, however it is seldom found in high concentrations and never found in a pure state; the difficulty in processing this material makes it expensive. [12]

## CRYSTAL STRUCTURE

Titanium can crystallize in two crystal structures, each of which is stable only within specific temperature ranges. At low temperatures, pure titanium, and the majority of titanium alloys, crystallizes in a hexagonal close packed structure (hcp), called α titanium. At high temperatures, it crystallizes in a body-centered cubic (bcc) structure, called β titanium (Fig.2.1) [13].

The temperature at which the allotropic transformation takes place is called β-transus temperature ($T_\beta$) and for pure titanium is 882±2 °C.

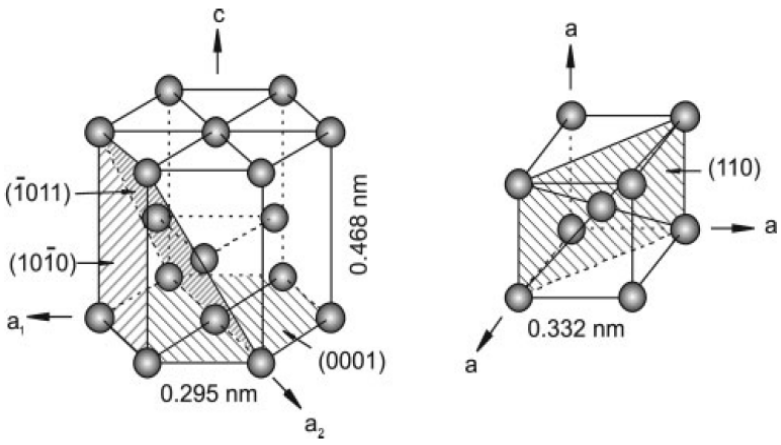


***Fig. 2.1*** *Crystal structure of hcp α and bcc β phase [12].*

## CLASSIFICATION OF TITANIUM ALLOYS

Titanium alloys contain different elements that, according to the influence on β-transus temperature, are classified as neutral, α-stabilizers, or β-stabilizers. The α-stabilizing elements extend the α phase field to higher temperatures, β-stabilizing elements extend the β phase field to lower temperatures, while neutral elements have minor influence on the β-transus temperature. [12] [13]

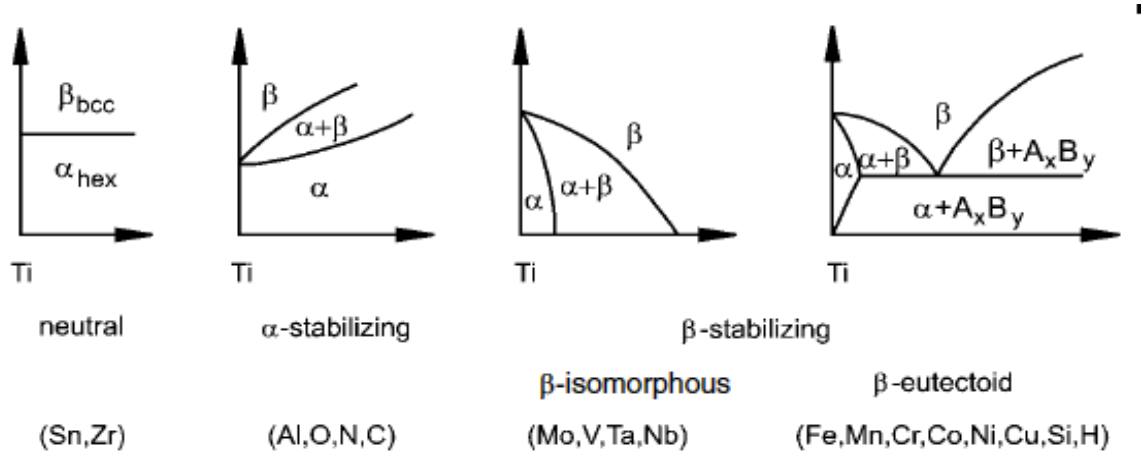


***Fig. 2.2*** *Influence of alloying elements on phase diagrams of Ti alloys [12].*

Moreover, the addition of α stabilizers leads to the formation of a two phase α+β field that includes alloys in which alpha and beta stabilizers coexist, as it occurs when beta stabilizers are added and β phase are retained under the β-transus temperature.

β-stabilizing elements are subdivided into β-isomorphous elements, e.g. Mo, V, and Ta, that are important due to their much higher solubility in titanium, and β-eutecticoid elements, e.g. Fe, Mn, Cr, Co, Ni, Cu, Si, and H, that even at very low volume fractions, can lead to the formation of intermetallic compounds (Fig.2.2).

Usually titanium alloys are classified as α, α+β (these alloys have a β volume fraction ranging from about 5 to 40% at room temperature), β alloys, near-α alloys (small fractions of β-stabilizing elements added) and metastable β alloys (where β no longer transforms to martensite upon fast quenching) (Fig.2.3).

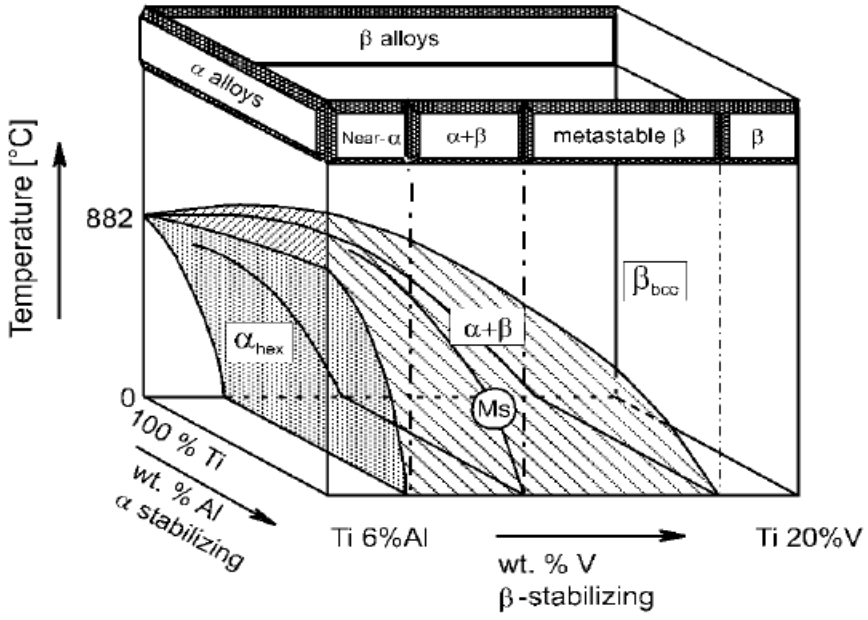


***Fig. 2.3*** *Three dimensional phase diagram to classify Ti alloys.*

Each titanium alloy class is characterized by different properties, listed in Tab. 2.1, that influence its behavior. α alloys have a lower density than β alloys due to the lower specific weight of aluminum compared to β alloying elements (such as Mo or V). Usually α alloys show only moderate strength, while α+β alloys and β alloys can be respectively hardened to high and very high strength levels respectively. In β alloys this can result in low ductility, while, if they are not age-hardened, they show relatively good ductility similar to that of and α+β alloys. The fracture toughness of titanium alloys is strongly dependent on the microstructure. In particular, coarse and lamellar microstructures show a higher values than fine and equiaxed ones. This can be explained by the ability of coarse and lamellar structures to deflect propagating cracks along differently oriented lamella packets, consuming energy for crack propagation.

Because of the densely packed atoms in α titanium, diffusion is considerably lower than in β titanium, and this is the major reason for the superior creep behavior of α compared to α+β and β alloys. High creep resistance is also observed for two-phase microstructures with a discontinuous distribution of β, such as lamellar and bimodal structures.

Titanium shows a high affinity for oxygen which leads to the formation of a very thin, dense oxide layer (TiO2) on its surface, and this is the reason for the excellent corrosion behavior of titanium alloys. Among the alloy classes, α is more stable to oxidation than β. The poor oxidation behavior of titanium alloys limited the maximum operating temperature above which a degradation of the mechanical loading capabilities occurs. Here, β is more susceptible than α. High reactivity with oxygen and hydrogen can cause the alloy embrittlement. Therefore, welding of titanium alloys has to be performed either in vacuum or an inert gas atmosphere. α and α+β alloys are easier to weld than β alloys. α and α+β alloys can only be deformed at high temperatures due to the more limited deformation capability.

The deformation temperature decreases with increasing β volume fraction.

| | α | α+β | β |
|---|---|---|---|
| Density | – | + | + |
| Strength | – | + | ++ |
| Ductility | –/+ | + | +/– |
| Fracture toughness | + | –/+ | +/– |
| Creep strength | + | +/– | – |
| Corrosion behavior | ++ | + | +/– |
| Oxidation behavior | ++ | +/– | – |
| Weldability | + | +/– | – |
| Cold formability | – – | – | –/+ |

***Tab. 2.1*** *Properties of α, α+β and β Ti alloys [12].*

### α ALLOYS

Pure titanium belongs to the class of α alloys, and it's available in four different grades, from 1 to 4, that differ in oxygen content, increasing from grade 1 to 4. CP titanium has been widely used for its corrosion resistance, ductility and strength for biomedical devices, as cardiovascular stents and lead wires but it is also used in the dental field [14] [15] [16]. The alloying oxygen increases strength but decrease the ductility.

### α+β ALLOYS

The α+β titanium alloys exhibit excellent mechanical and biological properties, as for example fatigue behavior, which led to the application of these alloys in the total joint replacement sector, high-corrosion resistance and low toxicity of ions released from the surface [13] [12].

Ti-6Al-4V has been the main biomedical α+β alloy for a long period.

Recently other titanium V-free alloys, such as Ti-6Al-7Nb and Ti-5Al-2.5Fe, which exhibit similar properties and microstructure as Ti6Al4V, have been developed because of the potential cytotoxicity of Al and V elements in Ti-6Al-4V.

### β ALLOYS

β titanium alloys exhibit much greater biocompatibility compared to α and α+β titanium alloys because of their much lower elastic modulus values (between 55 to 85 GPa for recently developed b-alloys) which are more similar to that of bone [16].

In recent years, have been developed new β-titanium alloys composed of non-toxic elements (Nb, Ta, Zr, Mo) as implant materials. The β phase can be completely retained at room temperature upon a sufficiently fast cooling, following solution treatment. β alloys show higher strength and toughness balance in comparison to α+β alloys.

## THE MICROSTRUCTURE OF TITANIUM ALLOYS

Generally, different microstructures are generated by thermomechanical treatments, that consist of a complex sequence of deformation, solution annealing and aging (Fig. 2.4).

The two extreme cases of phase arrangements are the lamellar microstructure, generated upon cooling from the β phase field, and the equiaxed microstructure, which is a result of a recrystallization process. Both types of microstructures can have a fine or a coarse arrangement of their two phases. [13] [12]

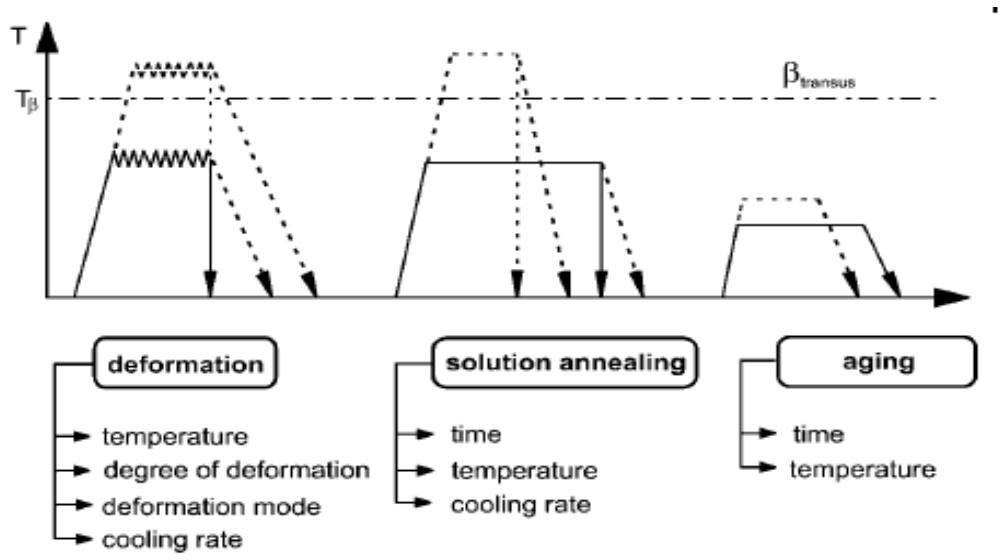


***Fig. 2.4*** *Thermomechanical treatment of titanium alloys [12].*

## THERMAL TREATMENTS

Upon cooling from the β phase field of titanium, the bcc structure (β phase) transforms to the hexagonal structure of α phase (Fig.2.5). The distance between the basal lattice planes in α is slightly larger than the corresponding distance between the lattice planes in β. Therefore, the phase transformation causes a slight atomic distortion (Fig. 2.6), caused by a slight contraction of a-axis in the hexagonal atomic structure.

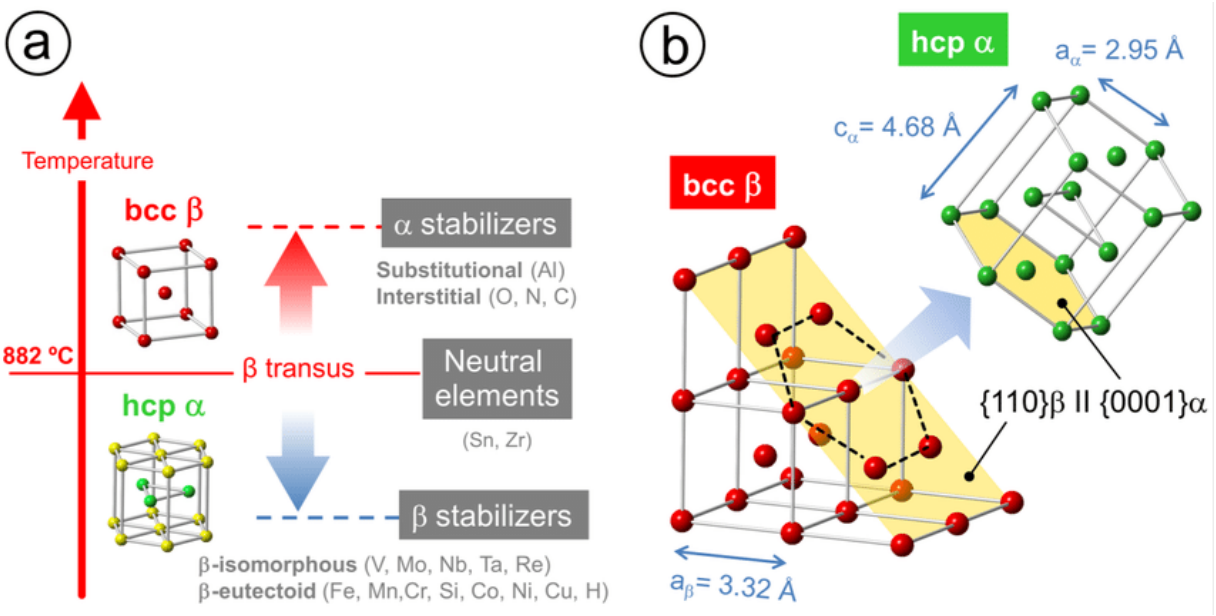


***Fig. 2.5*** *Crystalline structure transformation .*

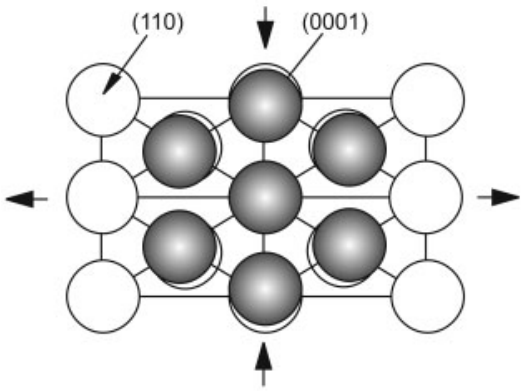


***Fig. 2.6*** *Atomic structure distortion during β/α transformation [12].*

It is possible to macroscopically observe a slight increase in volume during cooling through the β/α transformation temperature.

β decomposes by a diffusional process (nucleation and growth) or by a diffusionless process (martensitic transformation) [17].

The diffusion coefficient varies according to the microstructure. Below the β-transus temperature, slow cooling leads to a coarse lamellar structure that becomes finer by increasing the cooling rate. These lamellae are arranged in colonies or packets, which are similarly aligned and have a common crystallographic orientation. The α lamellae develop along the β grains boundaries and finally, α lamellae colonies form within the β grains [8] [12]. This type of α phase structure, obtained at low

cooling rates, is the well-known Widmanstätten α phase that forms as plates or needles (Fig.2.7) [17].

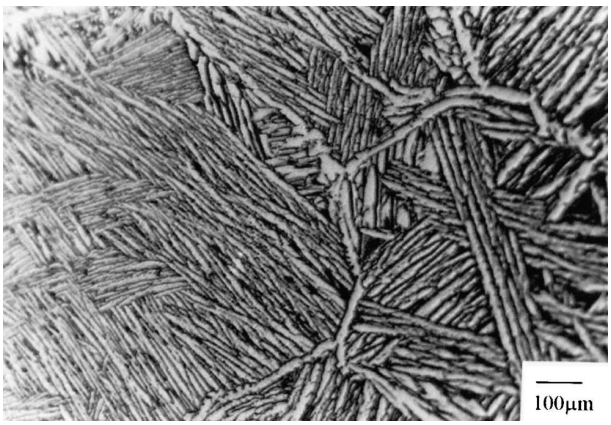


***Fig.2.7*** *Widmanstätten microstructure [17].*

As a general rule, α lamellae obtained at slow cooling rates, through the α+β phase region, are thicker than the lamellae obtained at faster cooling rates.

At high cooling rates, starting form temperatures above the martensite start temperature (MS), the bcc β is transformed completely into the hcp α, by a diffusionless transformation process, producing a metastable martensitic microstructure characterized by a very fine needle-like structure (Fig.2.8). The martensitic start temperature varies depending on the starting structure and the homogeneity of the microstructure.

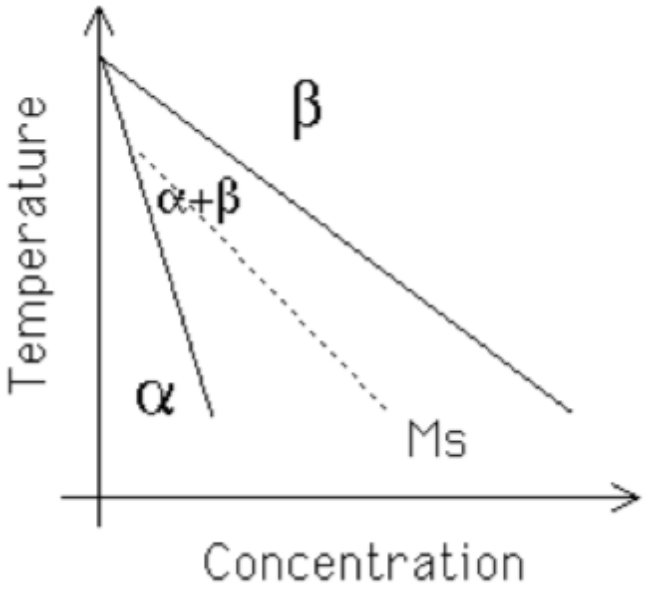


***Fig.2.8*** *Martensitic transformation from β [18].*

The martensite can be split into hexagonal α' martensite and orthorhombic α" (ω) martensite (Fig.2.9 and Fig.2.10). [8] [12]

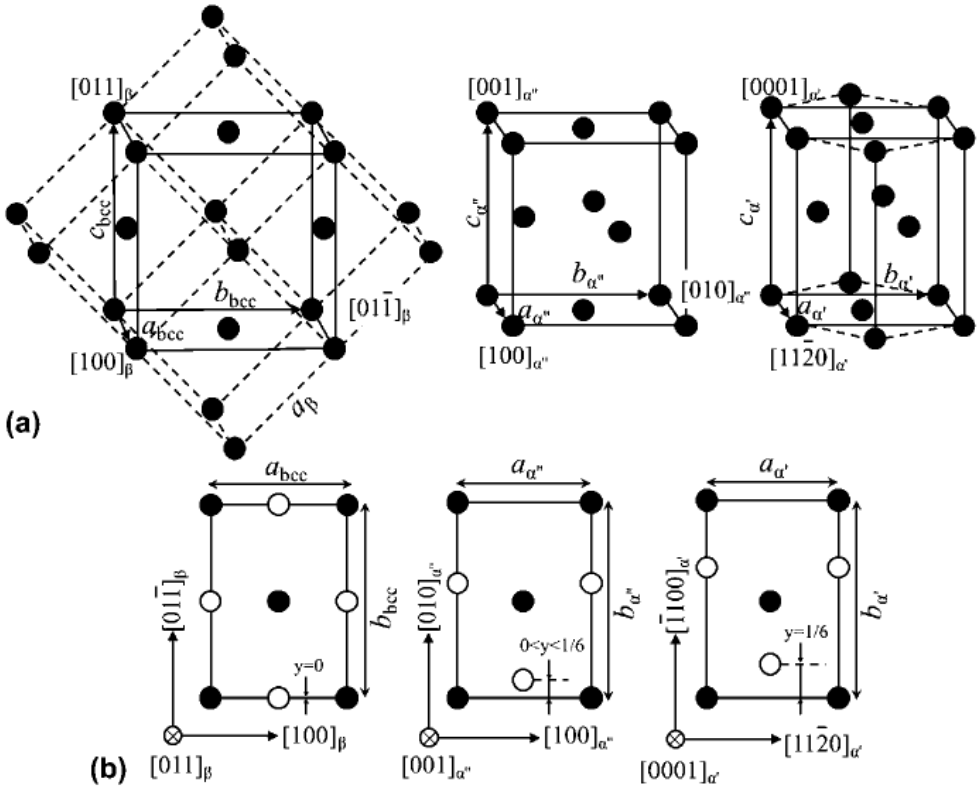


***Fig.2.9*** *(a) Schematic representation of the crystal structures of β, α" and α' phases (Conventional unit cells are indicated by dashed lines) and (b) their lattice correspondences (the solid and empty circles located respectively, at adjacent $(011)_\beta$ basal planes for the β phase, $(001)_{\alpha''}$ for the α"phase and $(0001)_{\alpha'}$ for the α' phase) [19].*

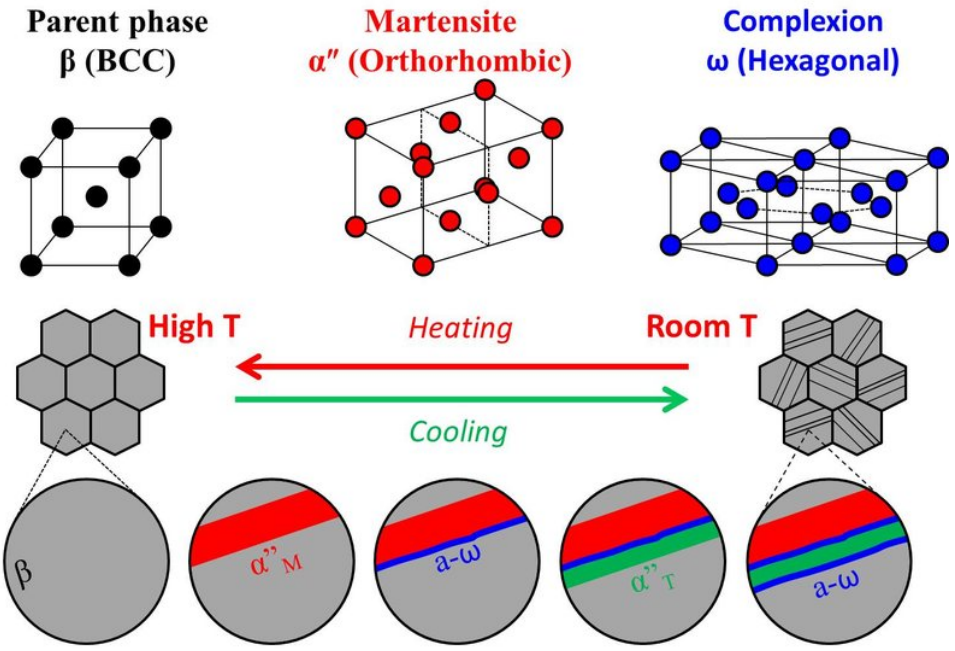


***Fig.2.10*** *Crystal structure of the different phases of titanium alloy involved during heat treatment [20].*

- Low amount of β stabilizing elements → hexagonal martensite.
- High amount of β stabilizing elements →orthorhombic martensite.
- Low amount of alloying elements, and high martensitic transformation temperature → massive martensite.
- High amount of alloying elements and low martensitic transformation temperature → acicular martensite. [8]

**Lamellar microstructure** is generated with simple cooling by decreasing the temperature from above the β-transus temperature. In this way α nucleates at grain boundaries and grows as lamellae into the (prior) β grain (Fig.2.11). Depending on the cooling rate, the lamellae are either fine or coarse (Fig.2.12).

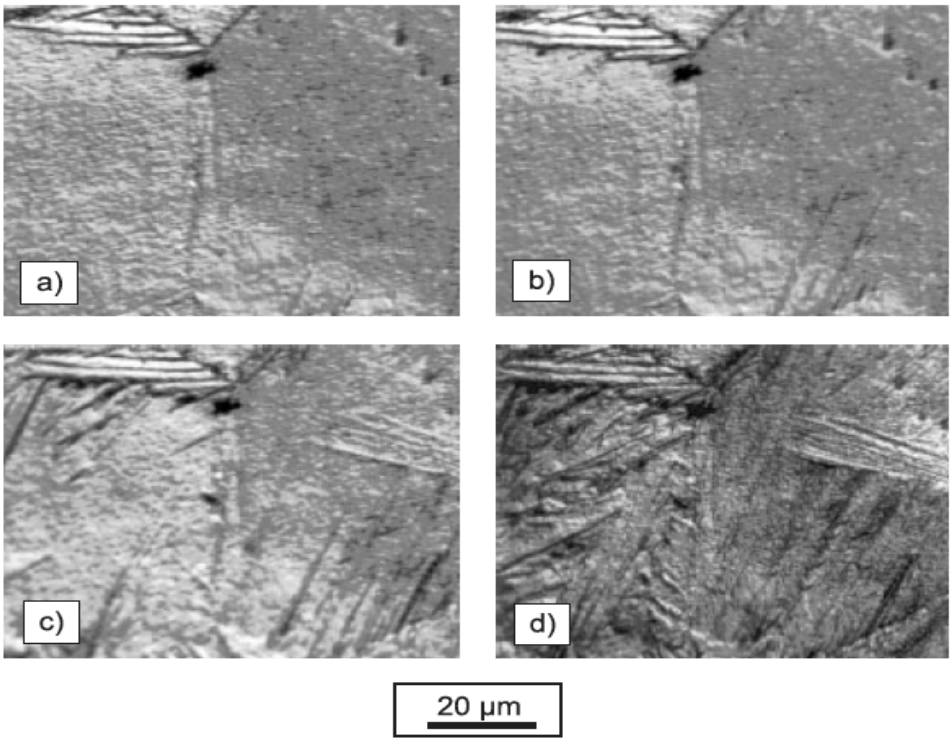


***Fig. 2.11*** *Example of nucleation and growth of the alpha phase into the (prior) β grains with cooling from the β-phase field. [12]*

Slow cooling from the β phase field, results in pure lamellar microstructures (Fig. 2.12 a). The lamellae become coarser by decreasing the cooling rate.

The metallographic figures show β as a small seam around the α lamellae (Fig. 2.12 a, c, e in gray). Rapid quenching leads to a very fine needle-like martensitic microstructure (Fig. 2.12 b). At lower temperatures below MS, the β volume fraction decreases and no longer transforms to martensite occurs (Fig. 2.12 f). [12]

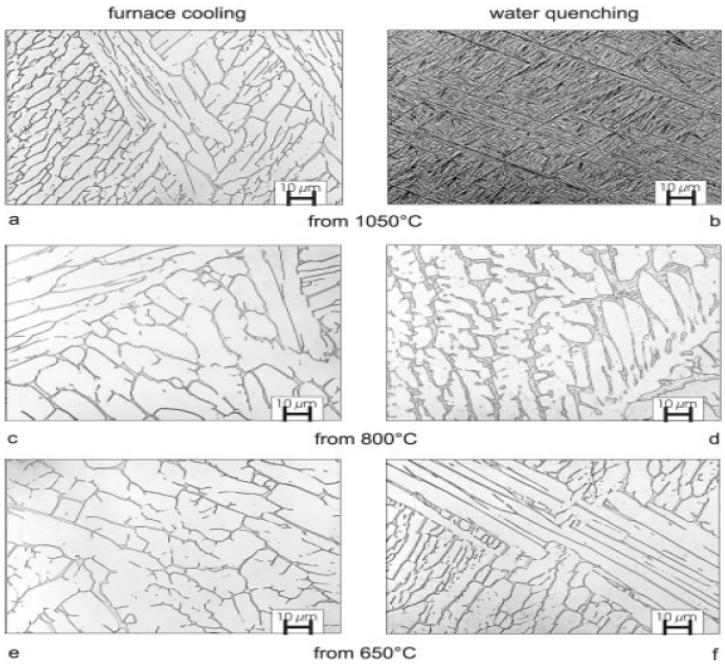


***Fig. 2.12*** *Schematic ternary phase diagram Ti-6Al-4V (MS: martensite start temperature); microstructure of Ti-6Al-4V after slow cooling (50°C/h) and after quenching from 1050°C, 800°C, and 650°C. [12]*

**Equiaxed microstructures** is generated by a recrystallization process. The first step is an highly deformation in the α+β field to introduce enough cold work into the material, followed by a solution heat treatment at temperatures in the two phase field (Fig. 2.13 a). Extended annealing makes the equiaxed microstructure coarser (Fig. 2.13 b). The heat treatment below the β-transus temperature results in bimodal microstructure that can be considered as a combination of lamellar and equiaxed microstructure (Fig. 2.13 c,d). [12]

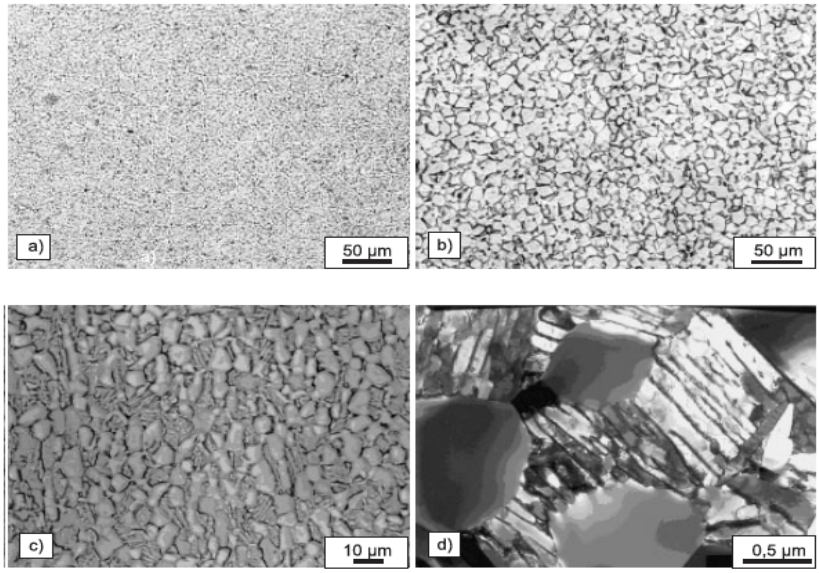


***Fig. 2.13*** *Equiaxed microstructures of Ti-6Al-4V via recrystallization: a) fine equiaxed; b) coarse equiaxed; c,d) bimodal [12].*

## SURFACE MODIFICATIONS OF TITANIUM AND TITANIUM ALLOYS

Surface modifications are often performed to improve the chemical, biological and mechanical properties of titanium and titanium alloys in order to obtain the clinical requirements for biomedical applications, although not all the requirements can be met.

Recent studies have shown that the corrosion resistance, wear resistance and biological properties can be improved by using the appropriate surface treatment techniques without changing the bulk attributes of titanium and its alloys [21].

The various surface treatment techniques can be divided in mechanical, chemical and physical methods.

- Mechanical methods

  Machining, grinding, polishing and blasting are used to produce specific surface topographies that improve adhesion in bonding by removal or by shaping of the material surface [21].

- Chemical methods

  They include biochemical modification, electrochemical (anodic oxidation) and chemical treatment. During these processes biochemical, electrochemical and chemical reactions at the titanium/solution interface lead to removal of the oxide layer and contamination, and to improvement of biocompatibility, bioactivity or bone conductivity [22].

- Physical methods

  The thermal, electrical and kinetic energy involved in these processes produce a surface modified films, coatings or layers on titanium or titanium alloys that improve wear resistance, corrosion resistance and biological properties [22].

Among physical methods, electron beam treatment could be a more suitable technique to obtain a precise surface topography, avoiding the contamination compared with the others techniques.

*Claudia Ramskogler et al.* worked on surface structuring of Ti6Al4V using an electron beam welding machine. By varying and optimizing the processing parameters, it was possible to obtained an hexagonal structures on the surface (Fig.2.14). They found out that, by EB technique, it is possible to produce complicate surface topography with good reproducibility, and to improve tribological behavior of Ti6Al4V (increase of the hardness) [23].

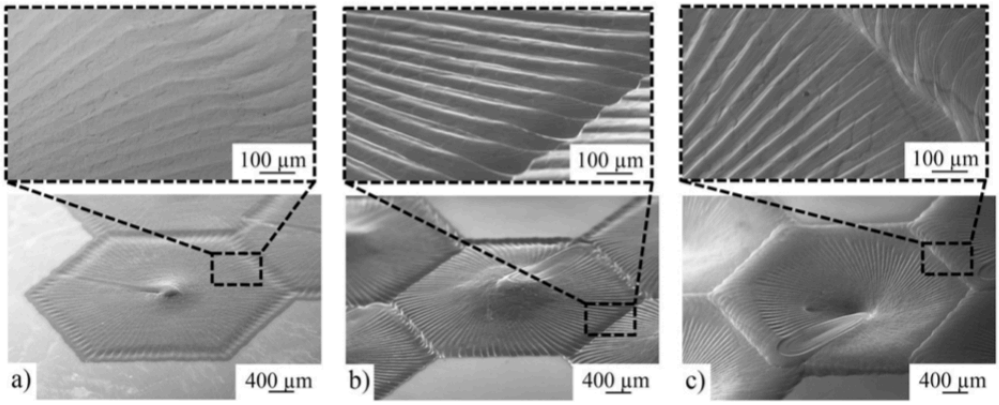


***Fig.2.14*** *SE-SEM images a) hexagonal pin array I = 0.8 mA v = 341 mm/s, b) hexagonal pin array I = 2.5 mA v = 698 mm/s, c) hexagonal wall array I = 2.5 mA v = 698 mm/s.*

*G. Camera et al.* studied the surface modification of Ti15Mo using the electron beam technique. The aim of the work was to obtained a surface micro topography characterized by different sized grooves (10 µm and 30 µm) in order to influence and study the behavior of cells and bacteria. They found out that 10 µm grooves were the best to obtain adhesion and cell alignment, while bacteria are not affected [24].

To ensure the efficacy and safety of implants over their useful life, it is necessary a good integration with the surrounding tissue, in which the surface topography of the implant has the important role [25] [26].

Studies revealed that there is a relationship between surface morphology and cell behaviour. Cells can sense macro and microtopography of the implant [27] but they can also sense and respond to nanotopography, since they live inside an extracellular matrix (ECM) containing nanoscale collagen fibrils and since their own surface is nanostructured (receptors and filopodia), but the way they do it is not yet fully understood.

It is important to remember that nanotopography as well as microtopography may induce surface energy differences. The presence of microstructures increases the air content of the surface, which increases the hydrophobicity of the surface, as described by the Cassie–Baxter equation [28] [29]. This effect may be more pronounced at the nanoscale level [30].

## CELL RESPONSE TO MICROTOPOGRAPHY

Cells are capable of sensing and responding to a large amount of biochemical and biophysical signals, over a wide range of length scales [31].

The ECM, through its structure and composition, presents a variety of physical cues on the order of micron and sub-micron scale, known as topographies [32] [33] [34]. The interaction and response of cells with these topographies are mediated through a phenomenon called *contact guidance* [35]. Contact guidance is known to affect cellular behaviors such as adhesion, morphology, migration, and differentiation [36] [37] [38] [39]. However, the underlying mechanism of how physical stimuli influence cellular behaviors has yet to be fully understood.

The majority of cells in the body necessitate to adhere to the ECM or other cells to survive and to function in a physiological manner [40].

Different cellular structures are involved in probing and sensing of the microenvironment and in cell attachment, these include integrins in cell-ECM contact [41], cadherins in celle-cell adhesion [42], stretch-sensitive ion channels [43], Tyr kinase receptors [44], and G protein-coupled receptors [45]. Integrins are part of a larger complex, known as focal adhesion (FA), that link the ECM to intracellular components (Fig.3.1). Substrate topography, imparted by ECM or micro fabricated substrates, influences the organization, arrangement, and distribution of integrins. Upon integrin engagement with the underlying substrate, cells start to spread and sense the topographical features of the substrate [46] [47]. This leads to alter the cytoskeletal organization, which in turn changes cell morphology and function [48].

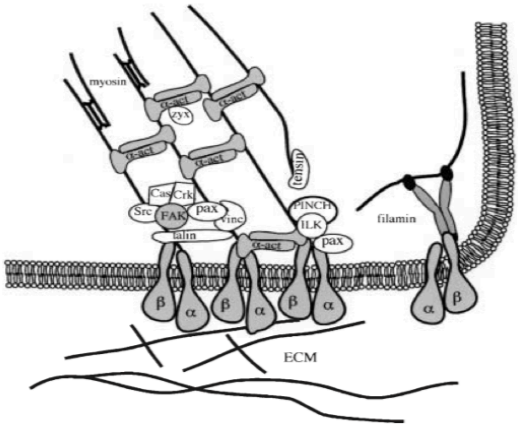


***Fig.3.1*** *Schematic representation of a focal adhesion. Transmembrane integrins bind to the extracellular matrix and associate within the cell with a complex of cytoskeletal proteins that link them to the actin filaments. The composition of focal contacts may vary depending on the function of cell, the extracellular matrix (ECM) component to which the cell is attached, and the integrin it expresses [41].*

Microscale grooves are among the most common fabricated topographical features that have been employed to control cell behavior. The majority of cell types, such us neurites, epithelial cells, fibroblast, osteoblast, cultured on these topographies align along the major axis of grooves, and their alignment and orientation enhanced on decreasing groove width and increasing groove depth (Fig.3.2) [49] [50]. In addition, alignment and localization of the FA complexes has been shown to be directly correlated with the cytoskeletal organization of cell [51]. Microtubules were the first cytoskeletal component to orient along the direction of grooves, followed by actin fibers. The response of cells to microscale topographies is highly dependent on the cell type, and on the geometry and dimension of the substrate's topography.

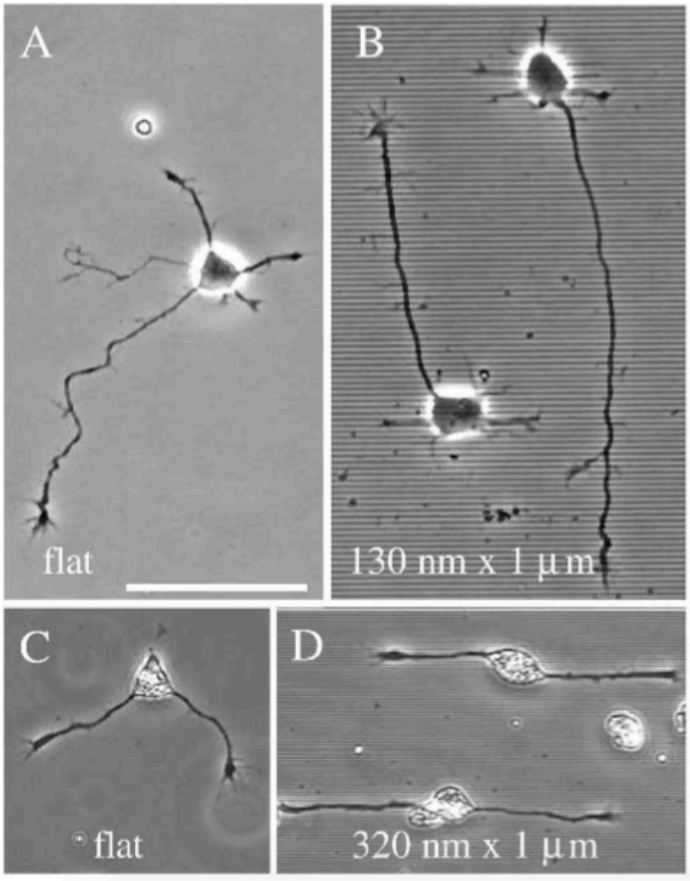


***Fig.3.2*** *Phase contrast micrographs of E16 rat hippocampal neurons (A and B) and Xenopus spinal cord neurons (C and D). Rat and Xenopus neurons had been growing for 24 and 4 hours, respectively. Cells are growing on flat quartz (A and C) or on grooves 1 µm wide and 130 nm deep (B) or 320 nm deep (D). In phase contrast micrographs of grooved surfaces the ridges appear as phase dark stripes and the grooves appear as phase bright stripes. Bars: (A,B) 50 µm; (C,D) 100 µm [49].*

ECM topography is one of the many factors that can influence the orientation of cell migration. In general, it is understood that cells migrate using a leading protrusion rich in actin (lamellipodium) [52]. It is possible that the physical structure and geometry of the ECM restrict sites of adhesion and directs migration through contact guidance [53].

It has been shown that cells cultured on grooved-topographies exhibit a higher migration speeds on narrower grooves [54]. In one study, groove topographies were micromachined from a titanium

alloy (Ti4Al6V) with groove, ridge, and depth dimensions ranging from 5 to 30 µm (Fig.3.3). It has been observed that fibroblasts were oriented parallel to the ridges's long axis with the highest migration velocity on 5 µm-wide ridges [55].

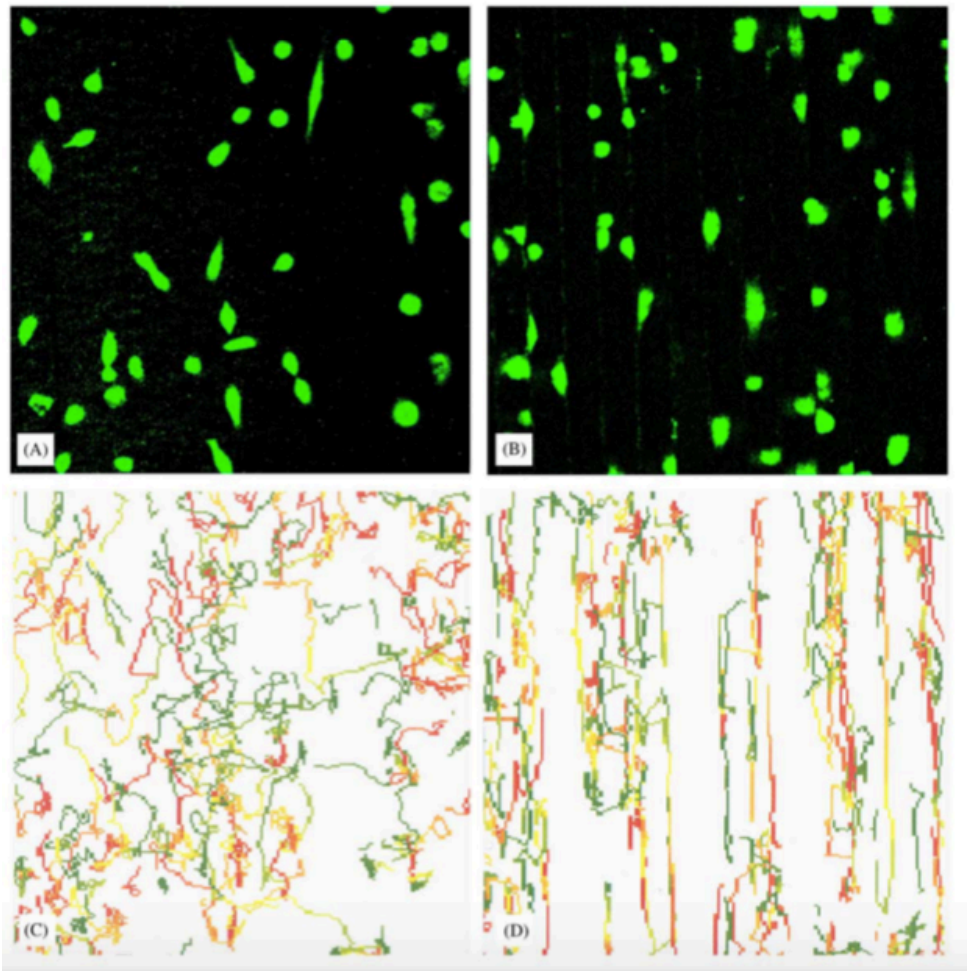


***Fig.3.3*** *Analysis of cell behaviour. One representative picture of a series made of DiI-labelled 3T3 fibroblast cells on the plane surface (A) and on the structured surface (B) (grooves depth:22µm; ridges width:22µm; spaced grooves: 18µm). The covered trails (trajectories) of the cells migrating on a plane surface (C) and structured surface (D) over an observation period of 24 h was drawn [55].*

## CELL RESPONSE TO NANOTOPOGRAPHY

Cells attach to a surface thanks to several biological molecules, most common of which are integrins [27]. Integrins are heterodimeric proteins which are constituted of two subunits. Upon attachment to a surface the integrin receptors cluster together and recruit cytoplasmic proteins to form a complex known as a focal contact. A distinction can be made between:

- focal complexes measuring <1µm
- focal adhesions measuring from 1 to 5µm
- super-mature adhesions measuring >5µm.

These complexes are on the micrometer scale, but integrins are on the nanometer scale (8–12nm), so they can be affected by surface nanotopography [56]. Additionally, an important factor in recruiting integrins, is the surface chemistry on the nanometer scale, that influence the adsorbed proteins. Hence nano-structured surfaces seem to have a significant impact on the organization and type of focal adhesions formed.

Before creating focal adhesions, the cell probes its environment and moves using projections such as filopodia and lamellipodia. These structures are nanosized (250–400 nm) [57] so it is likely that they will be influenced by nanotopography. The quality of the focal adhesions created has an important role on the cell alignment on nanogrooves.

Satoshi Fujita et al. studied the behaviour of mesenchimal stem cells on a nanogrooved surface with a 200nm groove depth, an 870nm ridge width and a 670nm groove width, and they found out that focal adhesions formed and extended in the direction of the ridges of the grooves were more stable and resulted in less filopodia retraction than when the focal adhesions were formed perpendicularly to the direction of the ridge (Fig.3.4) [58].

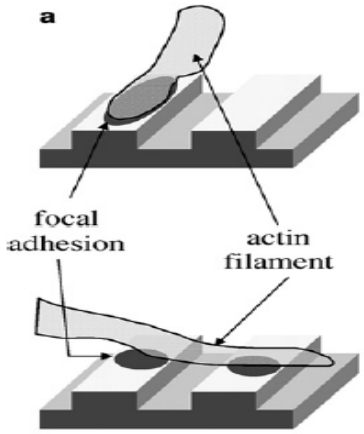


***Fig.3.4*** *in the image above the filopodia, parallel to the grooves, form wide focal adhesion. In the image below, focal adhesion is smaller because the filopodia is perpendicular to the grooves [58].*

This means that surface nanotopography can affect the shape and assembly of focal adhesions.

Nanotopography can be sensed as a barrier to the movement of cell projections (receptor clustering, filopodia) or can be sensed through the deformation of cell membrane (elongation and stretching on nanogrooves). It has been shown that changes in surface topography induce changes in the morphology of the cell. This causes a cascade of chemical signals that reaches the nucleus and modifies the gene expression as well as the cell behaviour [59] [60] [61].

There are a multitude of factors that will affect the behaviour of cells in response to surface topography, such as height, width and shape, but also the organization of the nanofeatures, the chemistry and rigidity of the surfaces and the type of cell used in the study.

- Influence of size

  From different studies, it has been observed that the effect of nanotopography on cells can be higly effective. It is usually reported that osteoblast are rugophilic (higher adhesion on rough surfaces) while fibroblast are rugophobic (higher adhesion on smooth surfaces), but this is probably not true on the nanoscale.

  M.J. Dalby et al. demonstrate that different type of cells (endothelial cells, fibroblasts, osteoblasts, leucocytes and platelets) strongly respond to a nano-islands topography 13nm tall in a Poly(styrene)- poly(p-bromostyrene) (PS/PBrS) substrate, increasing spread and proliferation [62]. In a further study they observed there was an interaction between 10 nm high nano-topography and fibroblast filopodia [63]. Therefore it could be that cells can sense features less than 10 nm high, but it is necessary an improvement in the resolution of the nanofabrication techniques to better study it.

  A nanosized topography greater than 30 nm seems to have a negative impact on cell adhesion and spreading. Dalby et al. studied the response of fibroblasts to polymer demixed nanocolumns 160 nm high and 100 nm in diameter and they observed decrease of cell adhesion and spread (Fig.3.5 and Fig.3.6). From these results Dalby et al. proposed a generalized cell response to changes in feature size: features <25 nm tall increased cell adhesion, whereas features in the range 40-160 nm decreased fibroblast adhesion [64] [65].

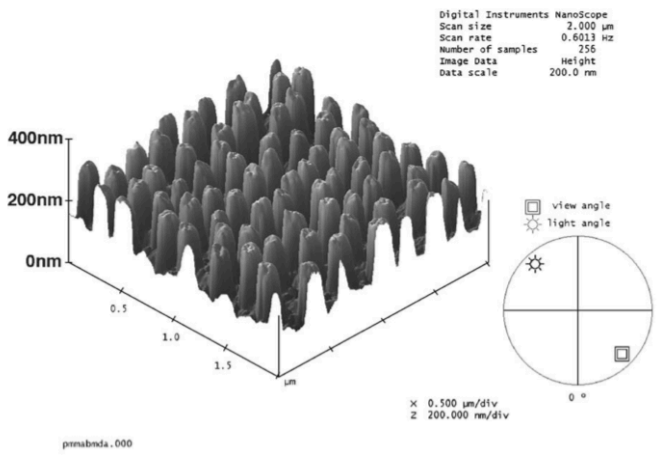


***Fig.3.5*** *Atomic force microscopical image of the 160 nm high nanocolumns [65].*

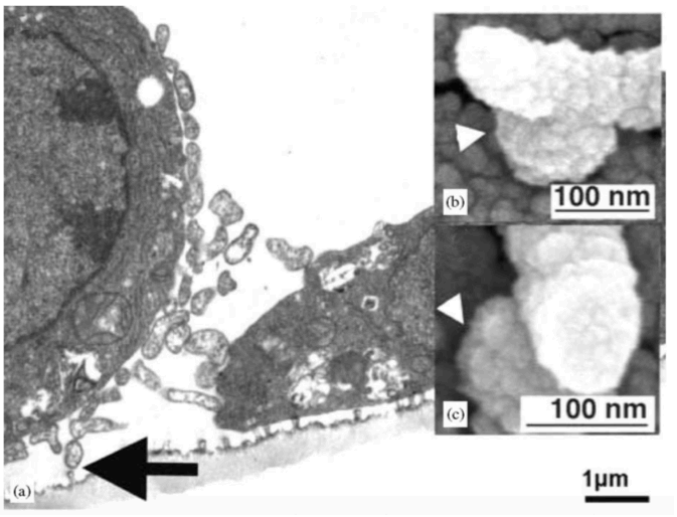


***Fig.3.6*** *Electron micrographs of filopodia reacting to nano-columns. (a) TEM section of a rounded cell with many filopodia, arrow shows filopodia/ nano-column interaction. (b and c) High magnification SEM's of filopodia bending upon contacting nanocolumns (nano-columns shown by arrowhead).*

Others studies have shown an increase of cell elongation and differentiation on larger nanotubes (70nm and 100nm) rather than on smaller nanotubes (30nm and 50nm) [66] [67]. A much detailed research is needed on these topics, because there are different studies that showed contradictory results.

Therefore, it is not possible to predict the effect of the nanotopography based only on size, but it is necessary to consider other parameters, such as morphology, organization and distance between nanofeatures.

- Influence of shape

Several studies demonstrated that cell responses were modified by the shape of nanofeatures and that these changes are related to the interactions of filopodia and focal adhesion complexes with the nanofeatures.

Ana I. Teixeira et al. investigate the response of human corneal epithelial cells to a lithographically defined substrates, and they found that cells elongated and aligned along patterns of grooves and ridges with feature dimensions as small as 70 nm (Fig.3.7) [51].

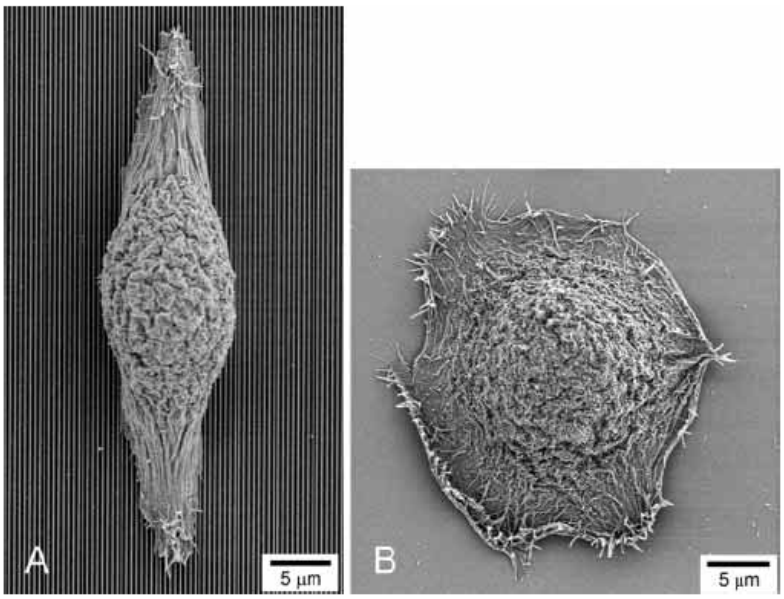


***Fig.3.7*** *SEM images of human corneal epithelial cells. (A) Cell cultured on a silicon oxide substrate patterned with 70 nm wide ridges, on a 400 nm pitch. The groove depth was 600 nm. (B) Cell on a smooth silicon oxide substrate [51].*

Matthew JohnDalby et al. studied the effect of topographies produced by colloidal lithography and polymer demixing on silicon down to 10 nm in size, on primary human osteoprogenitor cell populations. The results demostrated that the nanotopographies stimulated the osteoprogenitor cell differentiation towards an osteoblastic phenotype [68].

- Influence of the distance between nanofeatures

Spatz group. used hexagonally spaced gold nanoparticles spaced ranging from 28 to 110 nm. The size of each nanoparticle is 8 nm and allowed the binding of only one integrin. They demonstrated that osteoblasts grown on surfaces with a gold nanoparticle spacing of 58 nm or less, whereas on the sample with a gold nanoparticle spacing of 73 nm or more there was limited cell attachment and spreading, and a reduction in focal adhesion. This work demonstrates that the minimum spacing required for the clustering of integrins and activation of focal complexes is in the range 58–73 nm in the case of osteoblasts [69].

The spacing between nanofeatures is also important in order to permit the cell membrane to bend between the nanofeatures.

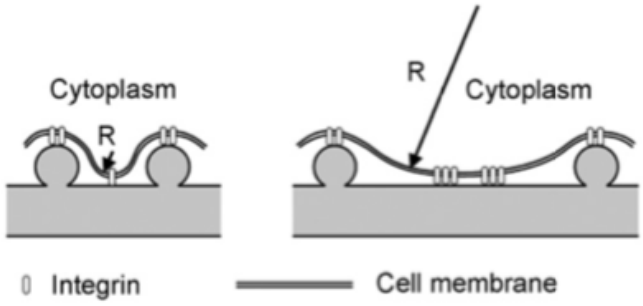


***Fig.3.8*** *Schematic drawing of bending of the cell membrane for different particle spacings [70].*

The cell distort its membrane in order to establish more integrin bindings with the surface between the particles. The energy needed to bend the membrane depends on the radius of curvature R. For a small radius of curvature (Fig.3.8 left) more work is needed than for a larger radius of curvature (Fig.3.8 right). In addition, there is more space to form integrin clusters between larger particles than between particles that are close together [70].

- Influence of the organization of nanofeatures

  The organization of microfeatures influences cell response. It has been demonstrated that by Bigerelle M Et al. that isotropic rough metallic surfaces are more favourable to human osteoblast cell adhesion than anisotropic ones [71]. The study result show that it is possible to influence the differentiation of stem cells using only the organization at the nanoscale of the surface on which they are grown.

- Influence of cell type

  S.Buttiglieri et al. observed the responses of three different endothelial cell lines grown on polymeric nanostructured surfaces consisting of nanohills with increasing hill height (13, 35 and 95 nm) (Fig.3.9). The 13 nm structures showed higher endothelization of all three cell lines [72].

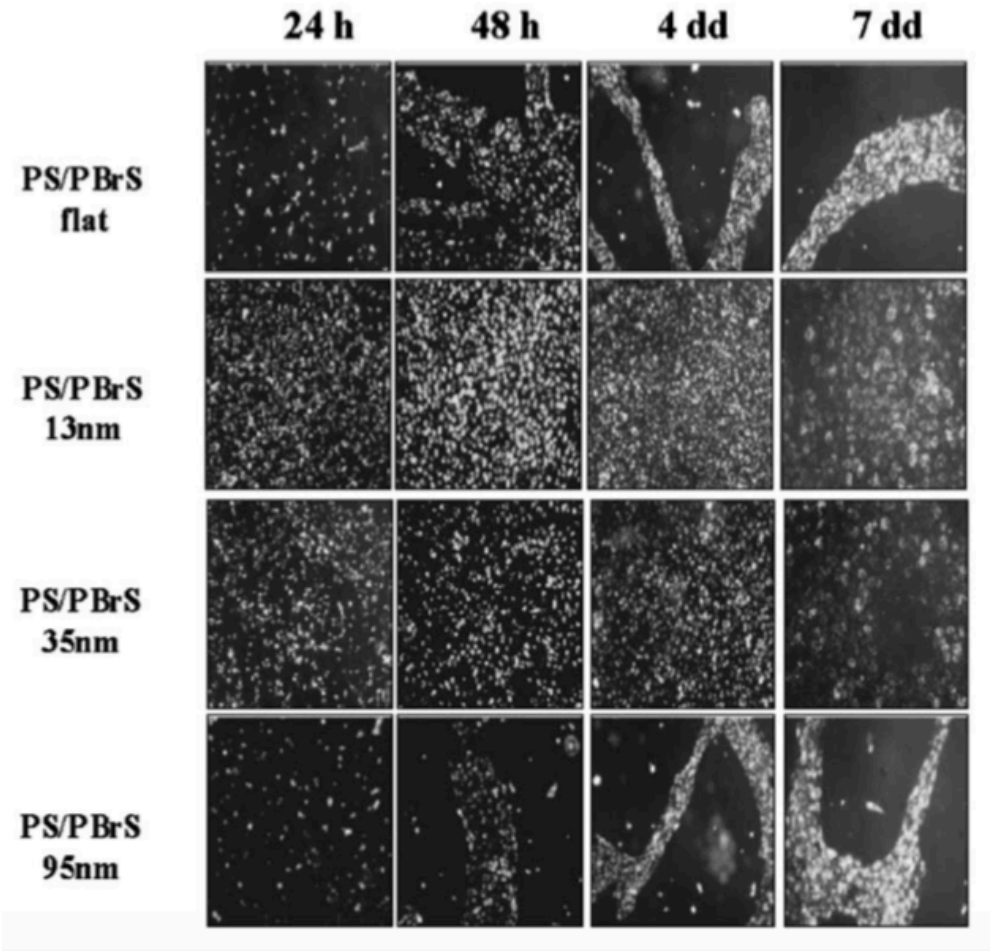


***Fig.3.9*** *Endothelization of Human umbilical vein-derived endothelial cells (HUVEC).*

Kwon, Keon Woo et al. used nanostructured polymer surfaces (400 nm pillars, 400 nm perpendicular, or 400 nm parallel lines) to study the adhesion difference between normal human breast epithelial (MCF10A) and cancer cells (MCF7). It was found that MCF10A cells showed higher adhesion than MCF7 cells regardless of culture time and surface nanotopography [73]. According to these studies, it is possible to deduce that cell of different phenotype detect and react in different ways to nanotopographies.

- Influence of chemical structuring on cell response

Dirk Lehnert et al. used microcontact printing to produce regular patterns of ECM protein patch (0.3-3μm$^2$ and a centre-to-centre distance of 1-30μm between the dots) separated by non-adhesive regions. Cells (Mouse B16F1 melanoma cells, buffalo rat liver cells and NIH 3T3 fibroblasts ) cultured on these substrata adhere to and spread on ECM regions (Fig.3.10). The extent of cell spreading is directly correlated to the total substratum covered with ECM-proteins, but independent of the geometrical pattern [74].

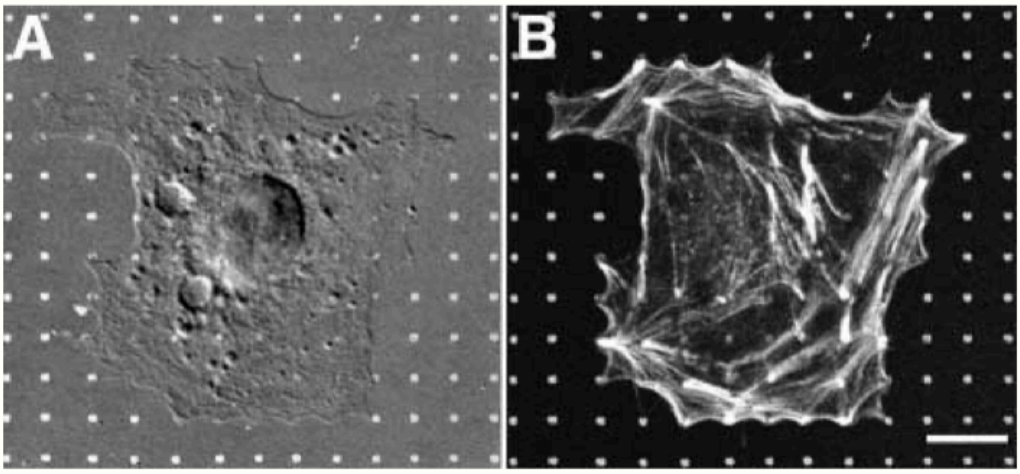


***Fig.3.10*** *Cell spreading on micropatterned substrata. A B16 mouse melanoma cell cultured for 1 hour on a patterned substratum of fibronectin. (A) Overlay of fibronectin immunofluorescence (white dots: 1 µm2; dot distance centre to centre: 5 µm) on a differential interference contrast image. The substratum determines the cell shape, resulting in a rectangular morphology. (B) Overlay of the fibronectin pattern and phalloidin staining reveals that most actin fibres terminate at fibronectin dots [74].*

Slater et al. have presented the fabrication and characterization of the surfaces with fibronectin 90–400 nm nano-patches, created using colloidal lithography, that provide well-defined cellular adhesion sites against a non-adhesive PEG background. They found that endothelial cells grown on control glass had larger focal adhesions around the periphery of the cell, whereas cells grown on the nano-patterns had smaller focal adhesions more distributed in correspondence with the pattern sites [75].

These studies allow to understand that it is possible to create nanoscale chemical patterns on surfaces that interact with cell integrins.

## INFLUENCE OF MICRO AND NANO STRUCTURES ON HGFS (Human Gingival Fibroblasts)

The following are some studies concerning the behavior of HGF (Human Gingival Fibroblast) on different structured substrates. This cell type is here described in details because it was used in this thesis work.

*C. Oakley and D. M. Brunette* studied the effect of grooved substrata on fibroblast and examined the sequence in which microtubules, focal contacts and microfilament bundles become aligned to the substratum topography. They used a grooved titanium-coated micromachined silicon wafer. The micromachined surface used had 3 µm-deep grooves with a 30 µm pitch comprising a 15 µm -wide groove and a 15 µm -wide ridge (Fig. 3.11). They found that microtubules were first aligned with

the direction of the grooves and then were followed by microfilament bundles and focal contacts so that after 6 h the cytoskeletal elements as well as the cell itself were aligned with the grooves [76].

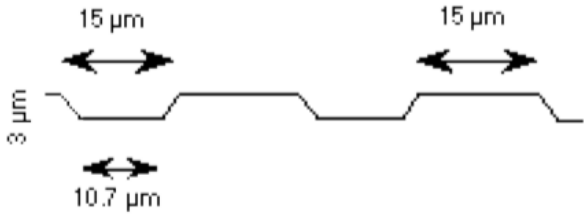


***Fig.3.11*** *30 µm pitch groove pattern in cross section [76].*

*E. Eisenbarth et al.* worked on cp-titanium, Ti6Al4V and TiTa30 grounded and polished to determine the influence of the surface structure on fibroblasts. They observed that the orientation of the cells along the marks increased with increasing surface roughness from 0.04µm (polished surface) to 1.36µm (grinded) (Fig.3.12) [77].

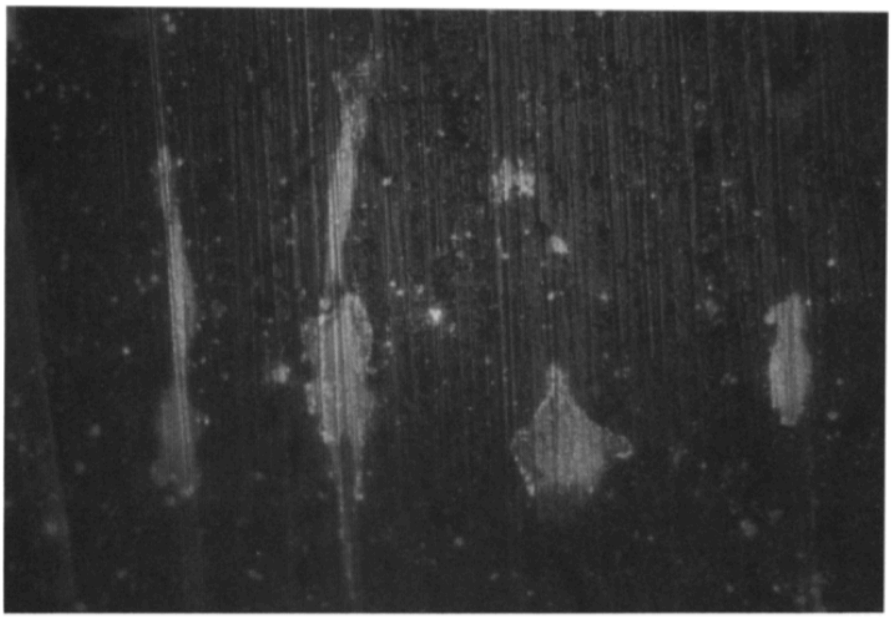

***Fig. 3.12*** *Fibroblast on ground Ti sample [77].*

*Xiao Wang et al.* investigated the biological behaviors of human gingival fibroblasts (HGFs) and oral pathogens on carbon-fiber-reinforced polyetheretherketone (CFRPEEK) surface modified by titanium plasma immersion ion implantation (PIII) technique to construct a multilevel $TiO_2$ nanostructure (Fig.3.13). They found that the nanoscale surface can greatly influence the synthesis of ECM and so regulate cell behaviors, such as migration, proliferation and focal adhesion formation. Furthermore, sustained and stable antibacterial activities against S. mutans, F. nucleatum and P. gingivalis are observed [78]. This last issue is of great relevance, because micro and nano topographies can potentially affect bacterial adhesion: modification of surface topography and its effect have to be studied both on cells and bacteria, even if this has been seldom done.

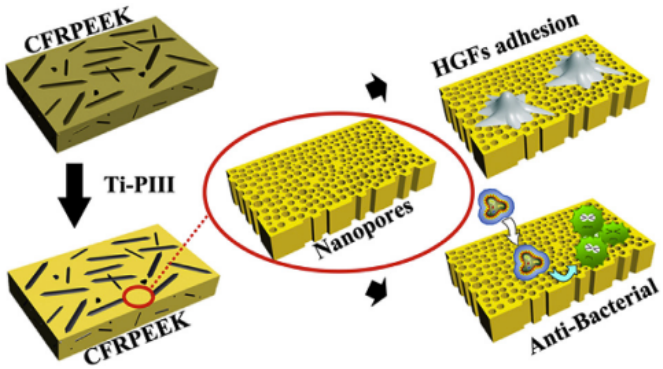


***Fig. 3.13*** *CFRPEEK with multilevel nanostructured TiO [78].*

*S. Ferraris et al.* studied the influence of nanogrooves (0.1-0.2µm) and keratin electrospun nanofibers on titanium surface on HGF. The results showed the capability of nanogrooves to drive fibroblast alignment, while keratin nanofibers increase their adhesion and proliferation (Fig.3.14) [79].

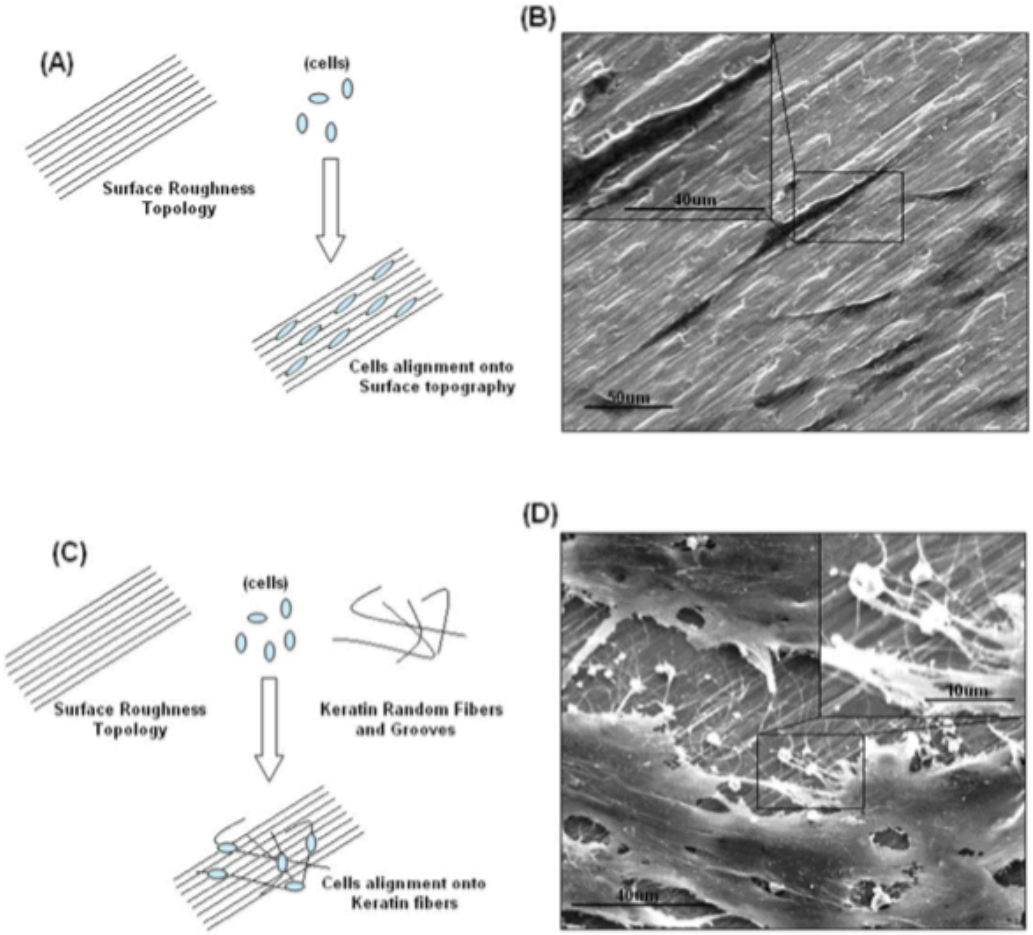


***Fig.3.14*** *Nanogrooves and keratin effects. Cells are able to feel and follow the surface grooves produced onto Ti-rough specimens (A–B); however, when the keratin was deposited onto the rough surfaces, cells were more influenced by the latter, thus spreading in a random arrangement (C–D) [79].*

*Xiaochong Jian et al*. observed the effect of fibronectin (FN)-coated micro grooved titanium plates on the alignment, spread, adhesion, and proliferation of human gingival fibroblasts (HGFs). Micro-grooved titanium (with 35 μm width, 15 μm bridge, 10 μm depth) plates were fabricated, and FN was immobilized onto the micro-grooved surfaces using silanization. The micro-grooved surface guides the HGFs to align along the grooves, and promotes cell spread, adhesion and proliferation [80].

*G. Camera et al.* worked on micro and nanostructured Ti15Mo surfaces, modified by electron beam structuring technique, thermal treatment and chemical etching, to evaluate their influence on fibroblasts and bacteria adhesion. They observed that 10 μm grooves EB are the better than 30 μm sized grooves to obtain adhesion and cell alignment. In addition, the Ti15Mo structured samples do not show an increase in bacterial adhesion compared to the smooth surface. [24].

In conclusion, based on literature data, an optimal groove size was supposed to improve fibroblast adhesion and alignment to substrate.

Grooves must have a width higher than 100 nm and less than 70 μm so that the cells themselves (fibroblasts) can reach the bottom, if the grooves are tighter, the cell alignment is higher, but takes longer time.

Regarding the depth of grooves, it must be less than 0.2 μm to avoid an increase of bacterial adhesion, and greater than 35 nm to be larger than the collagen fibrils. To ensure that cells adhering to different grooves are interconnected, grooves ridges must be smaller than 2 μm. Fibroblasts are also rough-phobic cells, hence a smooth bottom and rounded edges would therefore be better (Fig.3.15) [81].

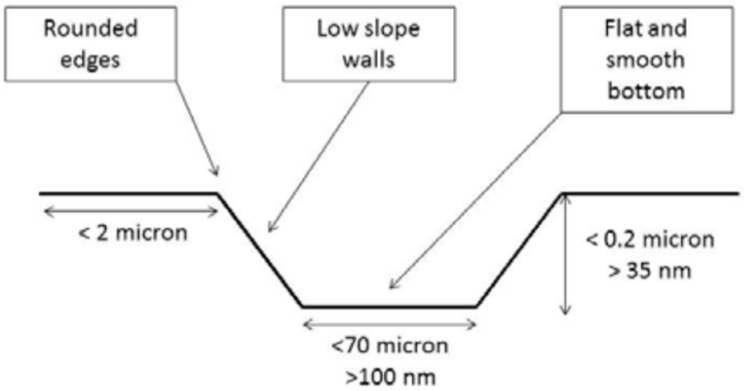


***Fig.3.15*** *Optimal size of grooves [81].*

These characteristics of the grooves maximize the contact guidance effect on fibroblasts, promoting cell adhesion and reducing bacterial adhesion.

## BACTERIA AND BIOFILM FORMATION

Bacteria are prokaryotic cells and differ from eukaryotic cells in several aspects. Their cell wall is composed of phospholipids, like eukaryotic cells, but they are much more rigid. This is in part due to an external layer of peptidoglycan, which is thick in Gram-positive bacteria whereas Gram-negative bacteria have a thin peptidoglycan layer which is covered by an additional polysaccharide outer layer (Fig.3.16) [82].

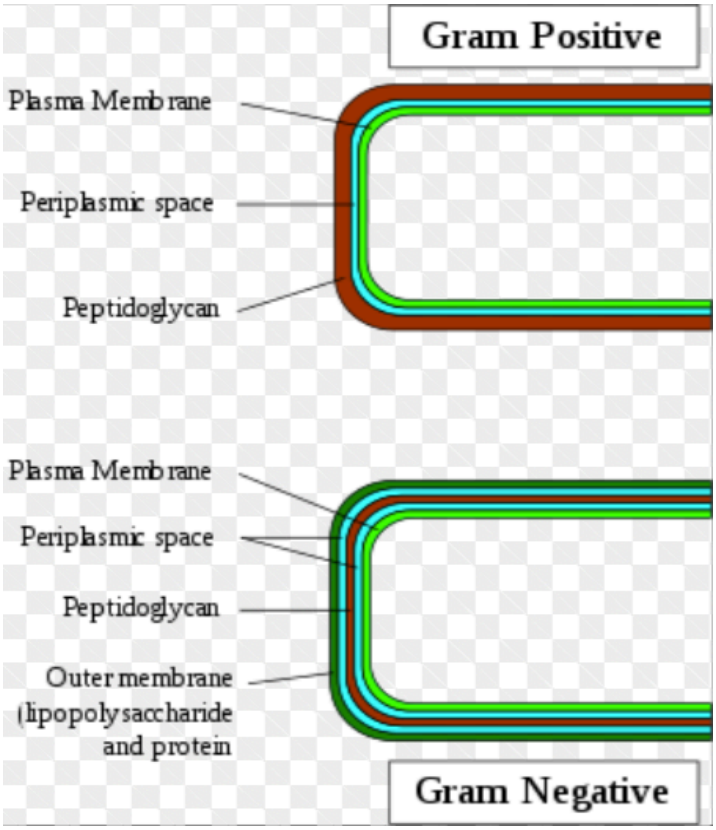


***Fig.3.16*** *Gram Positive and Gram Negative bacteria cell wall structure [82].*

They vary in size (from under μm to several tens of microns) and shape [83]. Some bacteria can express flagella, which render them very motile. Bacteria may also have fimbriae, also called pili or curli depending on species and strain, which aid in attachment to surfaces (Fig.3.17) [84].

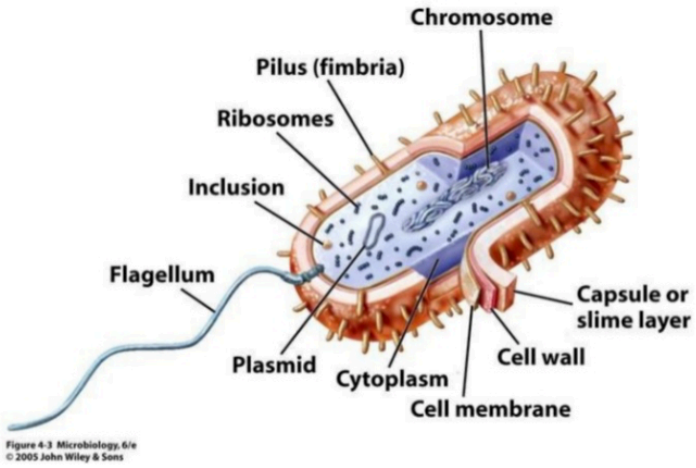


***Fig.3.17*** *Prokaryotic cel .*

Bacterial adhesion is an extremely complicated process, not very well know, that is affected by many factors including the environmental factors, such as the associated flow conditions, temperature, bacterial concentration, time of exposure, the presence of serum proteins or antibiotics, the bacterial properties including its structural features, such as flagellae, fimbriae and lipopolysaccharides [85], and the material surface characteristics [86].

Bacteria live as a community within a extracellular polymeric substance termed a biofilm, in which interact with other bacteria through membrane organelles and biochemical signals [87]. The biofilm develops in different steps (Fig.3.18).

1. The formation of a biofilm begins with the attachment of free-floating microorganisms to a surface.
2. The second step consists of adhesion of the bacteria to the surface. The first colonist bacteria adhere to the surface initially through weak, reversible adhesion via van der Waals forces and hydrophobic effects. If the colonists are not immediately separated from the surface, they can anchor themselves more permanently using cell adhesion structures such as pili. Usually these adhesions are described as ‘reversible adhesion’ and ‘irreversible adhesion’ [88]. Most authors consider that this is the step most influenced by topographical and chemical features of the surface.
3. The third step of biofilm formation consists of proliferation of the adherent bacteria and, synthesis of the biofilm matrix [89].

4. The final stage of biofilm formation is known as dispersion, and is the stage in which the biofilm is established and may only change in shape and size [90].

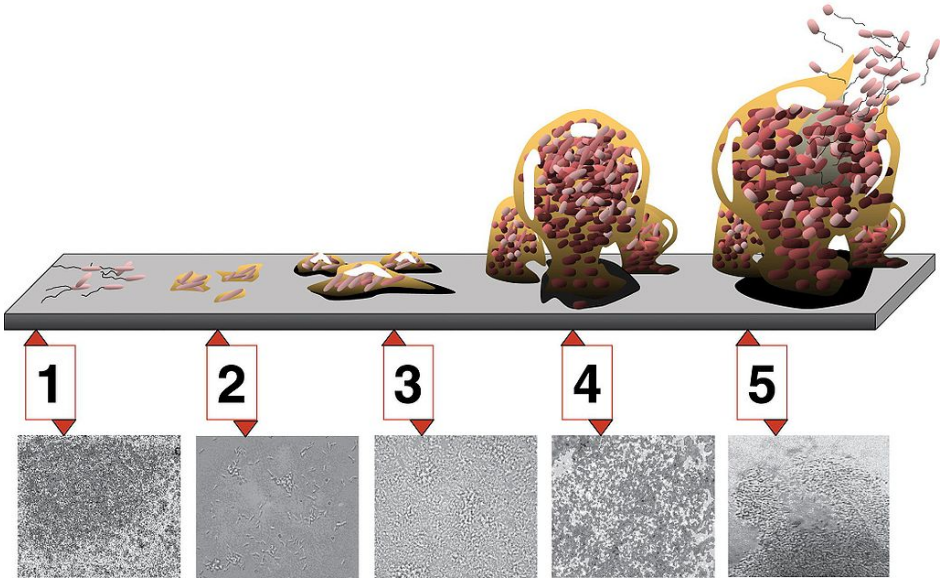


***Fig.3.18*** *Biofilm formation [91].*

Indirect experimental results support the idea that bacteria are able to use molecular features of their cell membrane as sensors and implement intracellular signaling pathways to sense the surface and to react to the stimuli created by the surface [92] [93]. The molecular and/or mechanical sensors that may be used by bacteria for surface sensing, as well as the intracellular signalling pathways that may allow bacteria to modify their metabolism in response to surface-related stimuli, are so far unknown. However, some features of the bacterial membrane, such as flagella, pili, curli and other fimbriae, have been shown to play a role in bacterial adhesion to surfaces [84] [94] and it has been suggested that they may also act as surface sensors when a bacterium is in contact with a surface.

A literature review by Teughels et al. focused on the trans-mucosal portion of the dental implant and concluded that a higher surface roughness (above of 0.2μm) increased biofilm formation and maturation, independent of the material [95].

## BACTERIA RESPONSE TO MICRO AND NANOTOPOGRAPHY

The small size of bacteria compared with eukaryotic cells might be a favourable factor to sense submicrometer and nanometer topographical features. However, bacteria are much less deformable than eukaryotic cells and upon attachment to a surface they will maintain their shape. This will hinder the interaction between a bacterium and a surface with topographical surface features with

typical dimensions smaller than the size of the bacterium, thus limiting the possibility for bacteria to detect them.

The bacteria membrane features (flagellae pili, curli and other fimbriae) may play an important role in bacterial attachment due to their small size: fimbriae have diameters less than 10 nm and are of varying lengths, from a few hundred nanometers to a few micrometres [83], while flagellae are thicker (some tens of nanometres in diameter) filamentous protein structure. Therefore, thanks to these membrane features it may be possible for the bacteria to adhere to surfaces with nanometric topographies. However, evidence of this has yet to be demonstrated.

It is widely accepted that bacteria react to surface topography that is larger than bacterial cells, adhering preferentially to the bottom of crevices [96], rather than to the top.

Whitehead et al. work's aim was to better understand the effect of the size and the morphology of surface features on bacterial retention. Surface features (pits) were produced with diameters of 0.2, 0.5, 1 and 2 µm. *Staphylococcus aureus* and *Candida albicans* were used. *S.aureus* (1µm diameter) were retained in the highest numbers, *C.albicans* (4µm × 5µm diameter) were retained in the lowest numbers [97]. It can be concluded, that bacteria significantly larger than the pits cannot be retained in large amount on the surface.

However, the bacterial response to microscale surface features has yet to be extensively studied and the effects at the nanoscale level are even less well understood.

Campoccia et al. studied the behavior of *Staphylococcus aureus* on polyethylene terephthalate (PET) surfaces either cylindrically nanostructured (PET-N) or flat ion-etched (PET-F), and on polystyrene (PS). In the absence of serum, all the materials showed a very high adhesivity to microbial cells and both PET surfaces exhibited greater adhesion than PS, while the presence of 10% serum in solution reduced the number of microbial cells on all the surfaces and PET surfaces became less adhesive than PS. The cylindrical nanostructures created on PET did not significantly influence microbial behavior [98]. It can be concluded, that protein adsorption can have a significant effect on reducing bacteria adhesion and sometimes this effect can be larger than what is related to topography.

Enhanced adhesion and retention of bacteria is expected with increasing surface roughness above 0.2 micron and this effect can be explained with the higher surface area available for attachment, protection from shear forces and the increase in convection mass transport due to the topographical features .

In any case, bacteria adhesion is not always greater on surfaces with a higher roughness.

Mitik-Dineva et al. studied the influence of very small topographical changes on bacterial adhesion. The surfaces were non etched and etched (smooth) glass surfaces obtained by chemical etching using hydrofluoric acid, characterized by a lower roughness ($R_a$ M = 2.13) (Fig.3.19). This study demonstrated an increase in the number of attached bacteria (marine bacteria) on the etched (smooth) glass surfaces. This results concerning the enhanced attachment of selected marine bacteria to smooth glass surfaces are novel [99].

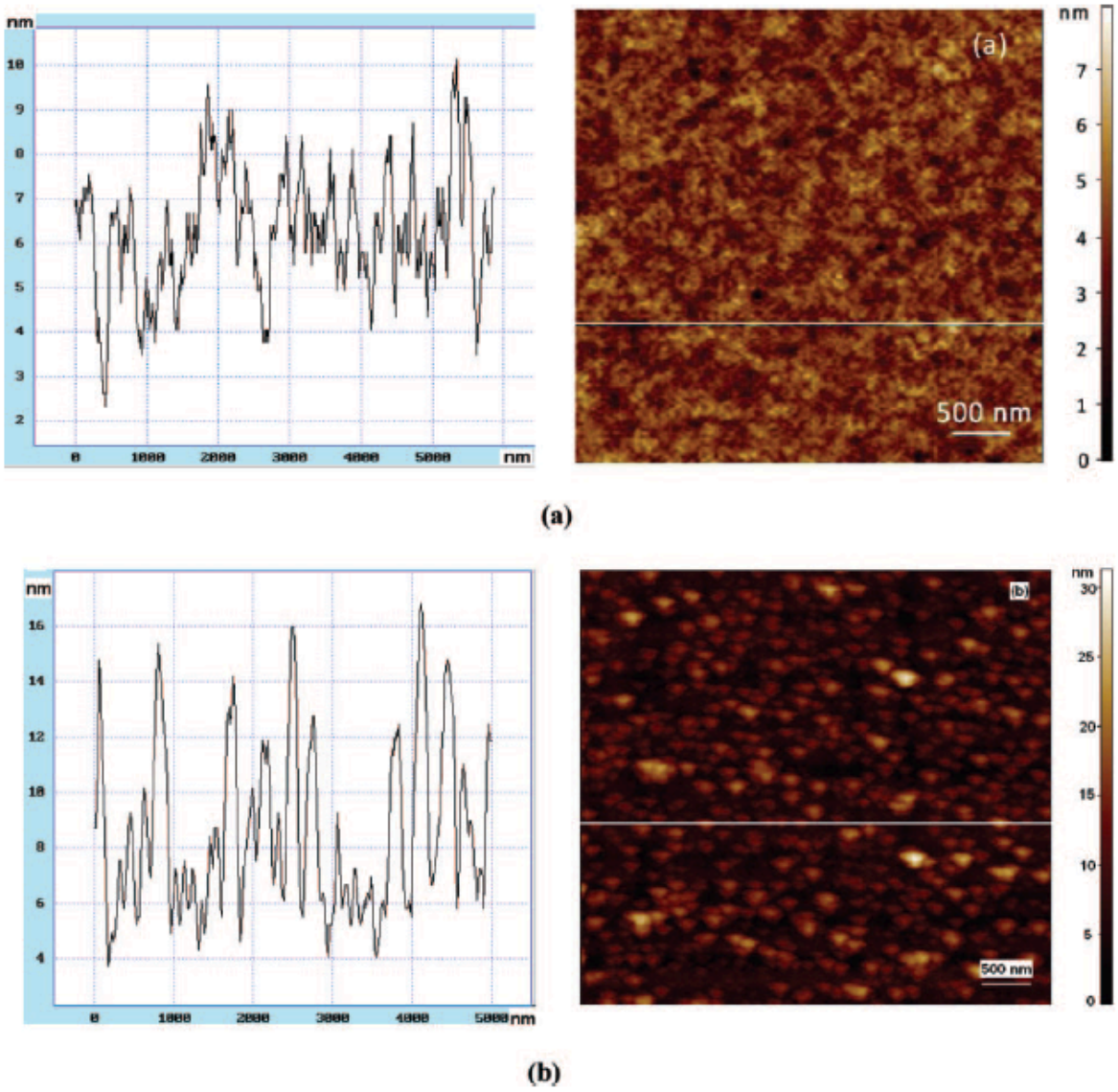


***Fig.3.19*** *AFM images of non-etched (a) and etched (b) glass surfaces and corresponding cross section surface profiles. The chemical treatment resulted in a reduction of surface roughness on the nanometer scale [99].*

These studies show that not only the microtopography but also the nanotopography plays an important role in bacterial adhesion, even if there is still disagreement over whether there are thresholds below and above which surface roughness can promote or inhibit bacterial adhesion.

As last, surface chemistry and crystallography can have an effect to be considered as added to the topographical ones.

Puckett et al. [100] studied the adhesion of Staphylococcus aureus, Staphylococcus epidermidis, and Pseudomonas aeruginosa on conventional Ti, nanorough Ti produced by electron beam evaporation, and nanotubular (with an inner diameter from 60 to 70 nm as shown in Fig.3.9 d) and nanotextured Ti produced by two different anodization processes. The nanotextured and nanotubular Titanium were found to be amorphous, while nanorough and conventional Titanium presented a crystalline structure. In particular, the conventional Ti contained rutile $TiO_2$, while the nanorough Ti contained anatase $TiO_2$.
The results showed that nanorough, nanotubular, and nanotextured Ti promoted protein adsorption; in addition nanorough Titanium decreased bacterial attachment compared to conventional, nanotextured and nanotubular Titanium. This could also be due to the antibacterial properties of the anatase $TiO_2$ , as shown by some research (Fig.3.20) [101] [102].

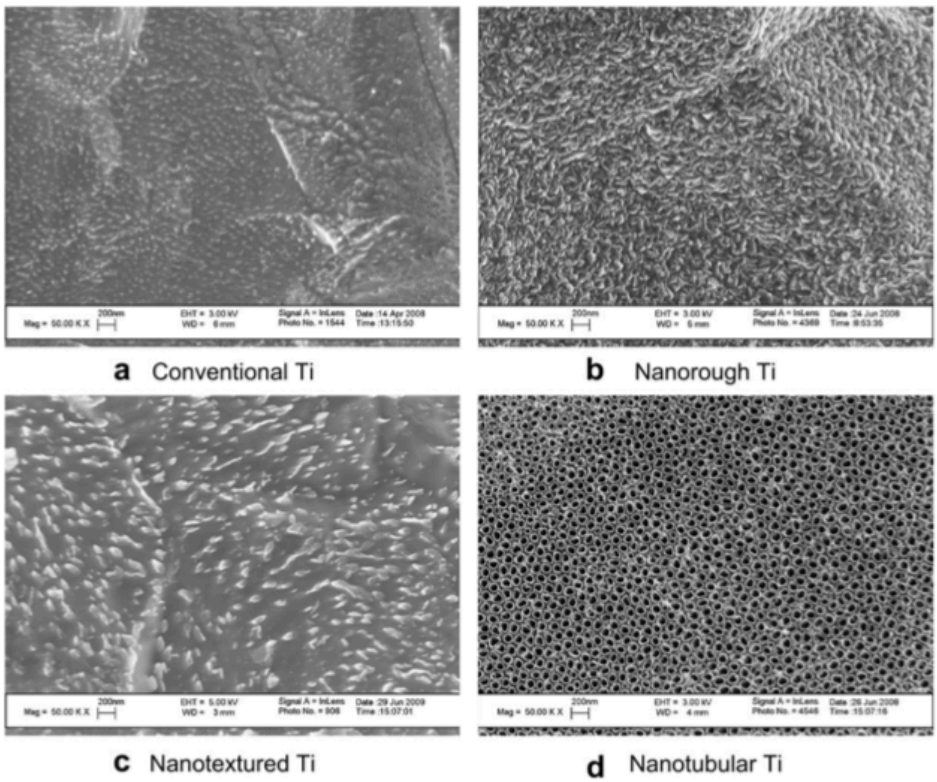


***Fig.3.20*** *SEM micrographs of Ti before and after electron beam evaporation and anodization: (a) conventional Ti as purchased from the vendor; (b) nanorough Ti after electron beam evaporation; (c) nanotextured Ti after anodization for 1 min in 0.5% HF at 20V; (d) nanotubular Ti after anodization for 10min in 1.5% HF at 20V. Scale bars= 200nm [100].*

## EFFECT OF THE MICROSTRUCTURE ON CELLS AND BACTERIA

Kurissery R. Sreekumari et al. studied the effect of Type 304 L SS weld microstructure on bacterial adhesion. The samples were machined to separate weld metal, the heat affected zone (HAZ) and base metal regions. Each zone present a different grain size: the smallest grains are in the weld metal region (10.83 μm ± 3.7) and the largest in the base metal (27.24 μm ± 3.18), while grains in the HAZ have an intermediate size (18.5 μm ± 1.15). The bacterial strain used for the attachment studies was Pseudomonas sp.

They observed that the base metal had the lowest area of adhesion, whilst the weld metal had the highest. The bacterial attachment was higher where there were the larger number of grains per unit area and vice versa (Fig.3.21). They noticed in fact that bacterial adhesion occurred on the grain boundaries [103].

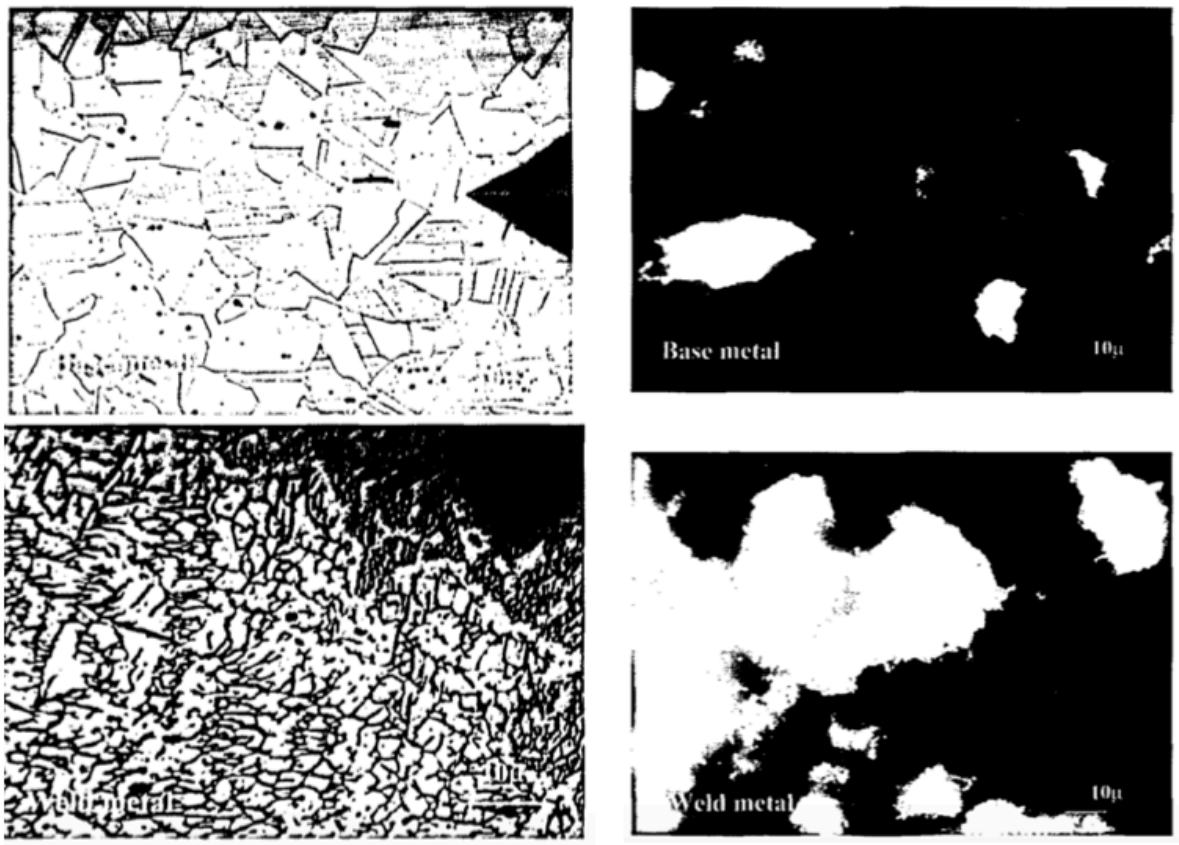


***Fig.3.21*** *On the left bright field microscopic images of base metal (upper) and weld metal (lower) coupons after electrolytic etching to show the distribution of grains (base metal) and grains and sub-grains (weld metal) on the coupon surfaces. On the right epifluorescence images of base metal (upper) and weld metal (lower) showing bacterial adhesion after 192h exposure in the experimental medium with Pseudomonas sp [103].*

Microstructure and topography are in some cases strictly interconnected. Vi K. Truong et al. worked on the effect of extreme grain refinement in the bulk, achieved by ECAP, of commercial purity titanium (CP, Grade-2) on bacterial attachment. ECAP produces a ultrafine-grain structure characterized by equi-axed grains with an average grain size of 170–200 nm. This was followed by

combined mechano-chemical polishing (Fig.3.22). In this way, the surfaces of ECAP-processed material develop a characteristic nanopattern that turned out to be suitable for *S. aureus* attachment [104].

These studies show how it is possible to control bacterial adhesion through microstructure. The proposed approaches to obtained a particular microstructure are promising for production of multifunctional orthopedic implants and should be further studied for improving efficiency in reducing complications in biomedical field.

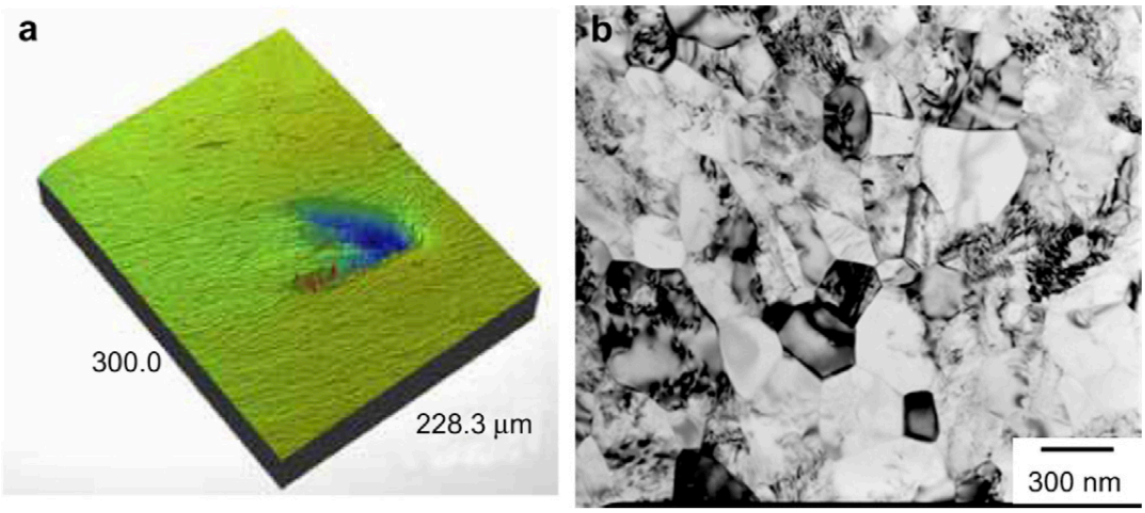


***Fig.3.22*** *Optical profiling of titanium surfaces after diamond polishing showing mechanical deformation (e.g., scratches and smearing) (a); High-resolution transmission electron micrograph of ECAP-processed titanium showing a uniform distribution of fairly equi-axed grains with an average grain size of 170–200 nm (b) [104].*

The following table 3.1 shows some of the studies that have been done to evaluate the influence of the substrate microstructure, micro and nanotopography on the behavior of cells and bacteria.

| SUBSTRATE | SURFACE MODIFICATION TECHNIQUE | MICRO STRUCTURE | MICRO TOPOGRAPHY | NANO TOPOGRAPHY | CELL TYPE | CELL RESPONSE | TYPE OF BACTERIA | BACTERIAL RESPONSE | REFERENCE |
|---|---|---|---|---|---|---|---|---|---|
| PS/PBrS | Polymer demixing | | | Nano-islands 13nm tall | Endothelial cells, fibroblasts, osteoblasts, leucocytes, platelets | increase of cell spread and proliferation | | | [62] |
| Template of cell-adhesive gold nano dots coated with cyclic RGDfK peptide | The dots were coated with RGDfK peptide by using block-copolymer micelle nanolithography | | | Dots diameter <8nm. Space between dots 28, 58, 73, and 85 nm. | Osteoblasts Melanocytes | Activation of integrins and focal complexes with a distance between the dots in the range 58–73 nm | | | [69] |
| Alpha titanium alloy: conventional Ti, nanorough Ti, nanotextured Ti | Conventional Ti, nanorough Ti produced by electron beam evaporation, nanotubular and nanotextured Ti produced by two different anodization processes. | Conventional and nanorough Ti surfaces presented crystalline $TiO_2$ . Nanotubular and nanotextured Ti surfaces were amorphous. | After electron beam evaporation, Ti substrates possessed a high degree of nanometer surface features. Nanotubular Ti surface contained structures with an inner diameter from 60 to 70 nm. | | Osteoblasts | Promoting bone tissue formation. | Staphylococcus aureus, Staphylococcus epidermidis | Certain nanometer sized Ti topographies and crystalline $TiO_2$ may be useful for reducing bacteria adhesion. | [100] |
| Polycarbonate (PC) plates | NG patterns printed on polycarbonate (PC) plates using supercritical CO2-assisted embossing | | | 200nm groove depth 870nm ridge width 670nm groove width | Human bone marrow-derived MSCs | Increased stability for focal adhesions formed and extended in the direction of the grooves | | | [58] |

| | | | | | | | | | |
|---|---|---|---|---|---|---|---|---|---|
| PS/PBrS | Polimer demixing | | | 90nm and 55nm high island | Human bone marrow cells | Cell differentiation | | | [68] |
| Silicon wafers | The silicon wafers were primed with hexamethyldisilazane and coated with UV3 photoresistpatterned lithographically. | | | 70nm grooves | Human corneal epithelial cells | Increase of cells elongation and alignment along grooves | | | [51] |
| Polidimetilsil ossano (PDMS) surface | Nanostructures were constructed on PDMS surface using a UV-assisted capillary moulding technique. | | | 400 nm pillars, 400 nm perpendicular400 nm parallel lines | Human breast epithelial cells MCF10A cancer cells MCF 7 | MCF10A cells showed higher adhesion than MCF7 cells | | | [73] |
| Polybromosty rene–polystyrene (PS/PBrS) and poly-*n*-butylmethacry late–polystyrene (PnBMA/PS) | Polymer demixing | | | Nanohills with increasing height (13–95 nm) | Endothelial cells | The 13 nm structures showed higher endothelization. | | | [72] |
| Surfaces presenting fibronectin nano patterns with a nonadhesive PEG background | The nanopatches were created using colloidal lithography | | | Fibronectin 90–400 nm nanopatches | Endothelial cells | The nanopattern influences cellular proliferation only at longer times, but influences spreading at both early and later times. | | | [75] |

| | | | | | | | | | |
|---|---|---|---|---|---|---|---|---|---|
| Gold-coated coverslip with a stamped thiol pattern. The remaining regions are blocked with a protein-resistant hydrophilic alkanethiol. | Microcontact printing method using a PDMS stamp | | 0.3-3μm$^2$ sized ECM protein dots with a centre-to-centre distance between the dots of 1-30μm | | Mouse B16F1 melanoma cells, buffalo rat liver cells, NIH 3T3 fibroblasts | The extent of cell spreading is directly correlated to the total substratum covered with ECM-proteins, but independent of the geometrical pattern. | | | [74] |
| Titanium-coated micromachined silicon wafer | Anisotropic etching produced f grooves on silicon wafers that were then evaporatively coated with titanium. | | 3 μm-deep grooves with a 30 μm pitch comprising a 15 μm -wide groove and a 15 μm -wide ridge | | Fibroblasts | Increase alignment and focal contacts formation | | | [76] |
| cp-titanium, Ti6Al4V TiTa30 | The plates were embedded in a methylmethacrylate plastic and polished with an alumina emulsion or ground with Sic papers of different grains. | | Different surface roughness of 0.04μm (polished surface),0.34μm and 1.36 μm | | Human Gingival Fibroblast | The number of orientated cells was shown to increase - independent of the material - with increasing roughness of the ground substrate. | | | [77] |
| Carbon-fiber-reinforced polyetheretherketone (CFRPEEK) | CFRPEEK surface was modified with multilevel $TiO_2$ nanostructure using titanium plasma immersion ion implantation technique. | | | Nanopores with diameters in the range of 150–200 nm | Human gingival fibroblast | The nanoscale surface influences the synthesis of ECM and regulate the expression of integrins | Streptococcus mutans, Fusobacterium nucleatum, Porphyromonas gingivalis | The nanoscale surface inhibit bacterial reproduction. | [78] |

| | | | | | | | | | |
|---|---|---|---|---|---|---|---|---|---|
| Keratin electrospun nanofibers on commercially pure titanium surface | Nanogrooves were produced by keratin electrospun nanofibers with the electrospinning technique. | | Nanogrooves 0.1-0.2μm | | Human gingival fibroblast | Increase fibroblast alignment, adhesion and proliferation. | Staphylococcus aureus | The grooved surface did not increase bacterial biofilm adhesion in comparison with mirror polished surfaces. | [79] |
| Fibronectin (FN)-coated micro grooved titanium plates | Titanium plates were polished by using waterproof abrasive paper and FN was immobilized onto the micro-grooved surfaces using silanization. | | Micro-grooved (with 35 μm width, 15 μm bridge, 10 μm depth) | | Human gingival fibroblast | HGFs alignment along the grooves, cell spread, adhesion and proliferation were promoted. | | | [80] |
| Glass surfaces as-received and chemically etched | Chemical etching with hydrofluoric acid | | Roughness glass non etched surface: 2.13<br><br>Roughness glass etched surface: 1.31 | | | | Five different marine bacteria | The number of attached bacteria increase on etched glass surfaces. | [99] |
| Type 304 L SS | AISI type 304 L SS welds were made by the Gas Metal Arc Welding (GMAW) process. | The smallest grains were in the weld metal region (10.83 (im ± 3.7), the largest in the base metal (27.24 *im* ± 3.18), grains in the HAZ showed an intermediate size (18.5 n,m ± 1.15). | | | | | Pseudomonas. | Grain dimension influences bacterial adhesion: base metal had the lowest area of adhesion, whilst the weld metal had the highest. | [103] |

| | | | | | | | | | |
|---|---|---|---|---|---|---|---|---|---|
| CP Titanium, Grade-2 | Equal channel angular pressing (ECAP) was used to form a sub-micron or nano-scale grain structure. | Average grain size of 170–200 nm. | | | | | Staphylococcus aureus, Pseudomonas aeruginosa | S. aureus had a greater propensity for attachment to ECAP-modified titanium surface, while P. aeruginosa, was less sensitive to it. | [104] |

***Tab. 3.1*** *Different studies on the influence of micro and nano topographies and microstructure on cells and bacteria.*

# MATERIALS AND METHODS

## INVESTIGATED MATERIALS

In this thesis work three different titanium alloys have been used: Ti grade 2 (α alloy), Ti-6Al-4V (α+β alloy) and Ti-15Mo (metastable β alloy) subjected to different Electron Beam structuring processes in order to obtain specific micro and nano structures on the surface. The final aim is to produce oriented grooves on the surface with micrometric spacing (5, 10, 30 μm) and nanometric width. The influence of the alloy composition and microstructure on the final topography and microstructure of the structured samples, as well as their biological response were in depth investigated.

The main features of the studied alloys are reported in the following and in table 4.1.

***α* alloy**: TiGr2 (commercial pure titanium alloy)

***α*+*β* alloy**: Ti6Al4V

**Metastable *β* alloy**: Ti15Mo

| *Physical property* | *Value* | *Unit* |
|---|---|---|
| Liquidus temperature | 1665±5 | °C |
| Density (20°) | 4.51 | g/cm³ |
| ***β***-transus temperature | 913±15 | °C |
| Young's Modulus | 105-110 | GPa |
| Specific Heat | 523 | J/kgK |
| *Mechanical property* | *Value* | *Unit* |
| Ultimate tensile strength | 345 | MPa |
| Yield Strength | 250 | MPa |
| *Physical property* | *Value* | *Unit* |
| Liquidus temperature | 1650-1660 | °C |
| Density (20°) | 4.43 | g/cm³ |
| ***β***-transus temperature | 1020±5 | °C |
| Young's Modulus | 105-116 | GPa |
| Specific Heat | 526 | J/kgK |
| *Mechanical property* | *Value* | *Unit* |
| Ultimate tensile strength | 1009-1054 | MPa |
| Yield Strength | 923-924 | MPa |
| *Physical property* | *Value* | *Unit* |
| Liquidus temperature | 1704-1760 | °C |
| Density (20°) | 5.4 | g/cm³ |
| ***β***-transus temperature | 774±14 | °C |
| Young's Modulus | 78 (***β*** annealed condition)<br>106 (***α*+*β*** annealed condition) | GPa |
| Specific Heat | 500 | J/kgK |
| *Mechanical property* | *Value* | *Unit* |
| Ultimate tensile strength | 775-785 | MPa |
| Yield Strength | 715-730 | MPa |

***Tab.4.1*** *Physical and Mechanical properties of the investigated materials [8].*

## SAMPLE PREPARATION

This thesis work has been carried out on specimens of Ti-6Al-4V, with dimensions of 15 mm x 15 mm, Ti grade 2, with dimensions of 15 mm x 15 mm and Ti-15Mo with dimensions of 10 mm x 15 mm. All of the samples have about 2 mm of thickness. These were grinded and polished with a *Struers Tegramin-30* machine (Fig. 4.1), in order to remove surface imperfections and obtain mirror polished surfaces.


***Fig. 4.1*** *Struers Tegramin-30 machine.*

The specimens were fixed to a metal disc using adhesive tape and glue (Fig 4.2). In this way has been possible to polish one of the surfaces.

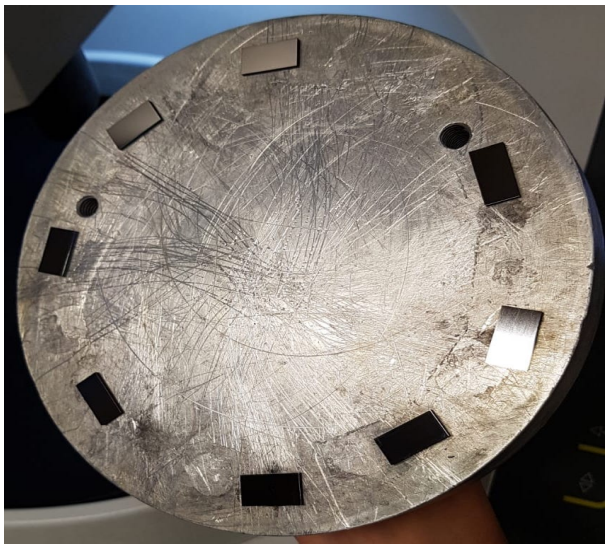

***Fig 4.2*** *Specimens fixed on the metal disc after the polishing process.*

Samples were grinded using silicon carbide abrasive papers with different grit sizes: P320, P800, P1200, P4000, for about 3 minutes per paper. After every paper change, samples were washed with water and ethanol and well dried.
The process parameters used were the following:

- 150 rpm speed
- a force of 30 N (single specimen mode)
- Co-rotation of the plate and the metal disk.

The process was performed under water lubrication.
Then specimens were finally polished using a MD-chem cloth with a solution of OPS *Nondry* (non-drying colloidal silica suspension for final polishing) and distilled water, for about 5 minutes using the same machine parameters.

To remove OPS, the specimens were subsequently washed with water and ethanol and well dried, and then detached from the metal disk.

## ELECTRON BEAM STRUCTURING

Electron beam structuring technique was used to modify the specimen's surface and to produce surface microstructures. The EBW machine used in the experiments is the *pro-beam Kammeranlage K14* (Fig. 4.3).

***Fig. 4.3*** *pro-beam Kammeranlage K14*

The specimens were placed in the vacuum chamber, using a samples holder, as shown in the following figures (Figure 4.4 and 4.5).

***Fig. 4.4*** *Specimens placed in the samples holder.*

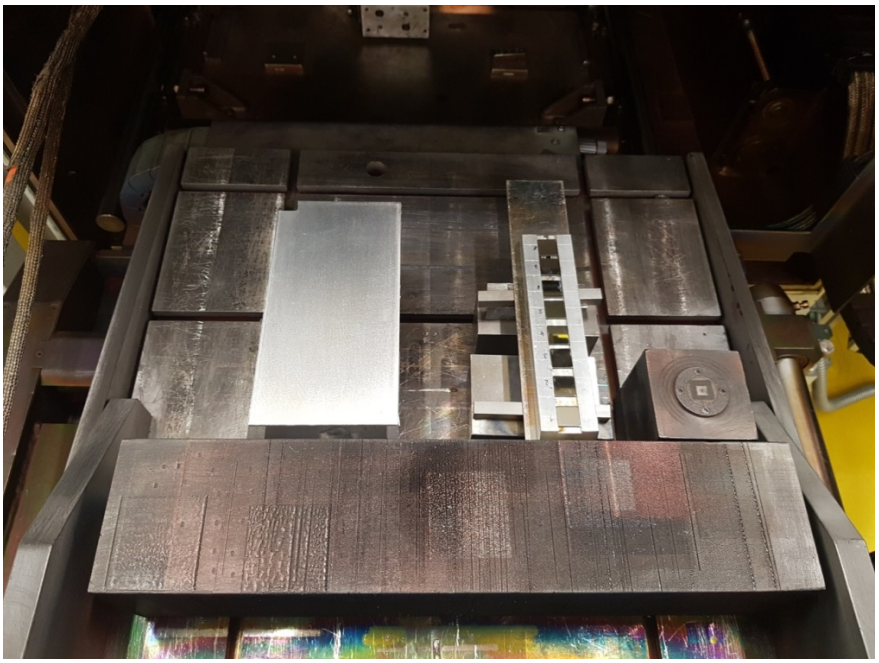

***Fig. 4.5*** *Samples holder placed in the vacuum chamber.*

The technique offers a highly beam power and a fast scan speed/beam deflection due to the guiding of electrons by the magnetic field. The free electrons in vacuum can be accelerated by an electric field, and their orbit can be controlled with a magnetic field in order to form a fine beam. The kinetic energy of electrons shooting on the workpiece produces the heating source for the technique. This concentration of energy in a small volume of workpiece allows to structure its surface. The free electrons are produced by a tungsten cathode that is heated to a certain temperature, and the high voltage between the cathode and the anode forces their emission towards the anode [105].

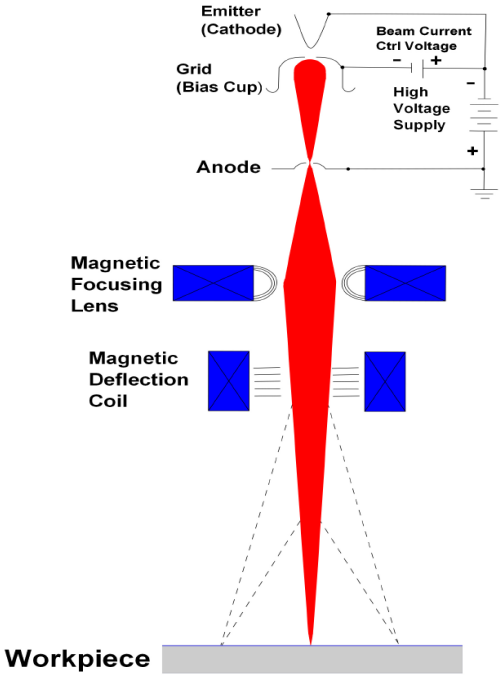


***Fig. 4.6*** *Electron beam welding technique.*

The high voltage (HV) value is proportional to the electron's achieved velocity. A higher voltage results in a higher velocity.

The electrons respond to magnetic field according to the Lorentz force $\overrightarrow{F_L}$. The force $\overrightarrow{F_L}$ acting on a particle of electric charge $q$ with instantaneous velocity $\vec{v}$, due to an external electric field $\vec{E}$ and magnetic field $\vec{B}$, is given by

$$\overrightarrow{F_L} = q \cdot (\vec{E} + \vec{v} \times \vec{B}) \tag{4.1}$$

Faster electrons are more influenced by magnetic fields, and thus the electron beam can be focused better by the beam gun's focusing magnetic fields.

The impact of high-speed focused electron beam onto the material causes heating, melting, local evaporation and formation of the so called “keyhole”. By moving the electron beam over the surface of the workpiece, a material transport occurs in the opposite direction of welding direction: the molten material is moved behind the beam and solidifies at the backside, resulting in a protrusion at the beginning and an intrusion at the end of the weldment (Fig. 4.7) [106].

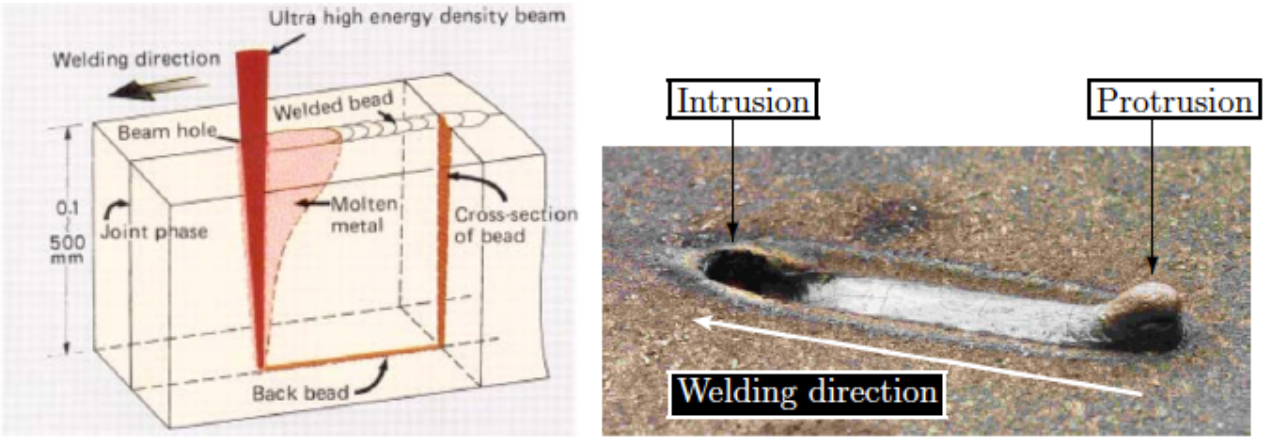


***Fig. 4.7**: Electron beam welding technique: (a) Keyhole formation [107] and (b) the resulting protrusion-intrusion effect from a single beam swipe [108].*

The surface structuring is based on the effect of creating protrusion patterns by repeating the beam movement on the same path. Depending on the repetition numbers, the protrusion height and intrusion depth can be raised as shown in Fig. 4.8.

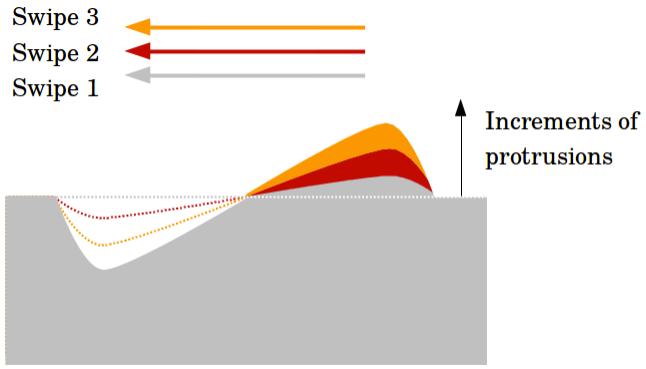


***Fig. 4.8** Effect of repeated beam swipes on the surface.*

The beam itself has virtually no inertia so it can be deflected instantaneously and very precisely, allowing a very selective and precise weldments with very little distortion. The deflection of the EB can be programmed in a specific way to generate corresponding figure arrays on metallic materials.

In this thesis work the figure created on the specimen's surface consists in parallel lines spaced 30,10 or 5µm which form a 7x7mm structured area on the samples surface. In this way it was possible to obtain two structured areas per sample.

The aim of the process was to create different size grooves on the surface in order to compare the effect of their dimension on cells and bacteria adhesion and alignment.

The file for the EBW machine was build using Matlab.

The main MATLAB and machine parameters used are reported in Table 4.1:

| | MATLAB Parameters | Machine Parameters | | | | | |
|---|---|---|---|---|---|---|---|
| | Distance Between Lines [µm] | HV (voltage) [KV] | I (current) [mA] | Velocity [mm/s] | PVZL | Total Time [s] | Vacuum Value [mbar] |
| **Ti6Al4V** | 30 | 150 | 0,8 | 853 | 4687 | 3,871 | 2.0E-4 |
| | 10 | | | 3333 | 1200 | 4,4325 | |
| | 5 | | | 5333 | 750 | 4,4294 | |
| | **MATLAB Parameters** | **Machine Parameters** | | | | | |
| **Ti15Mo** | 10 | 150 | 0,8 | 3333 | 1200 | 4,4325 | 2.0E-4 |
| | 5 | | | 5333 | 750 | 4,4294 | |
| **Tigrade2** | **MATLAB Parameters** | **Machine Parameters** | | | | | |
| | 30 | 150 | 0,8 | 853mm/s | 4687 | 3,871 | 2.0E-4 |
| | 10 | | | 3333mm/s | 1200 | 4,4325 | |

***Tab. 4.1*** *MATLAB and EBW machine parameters.*

At the end of the process it is possible to observe the microstructure on the surface of the samples (Fig. 4.9).

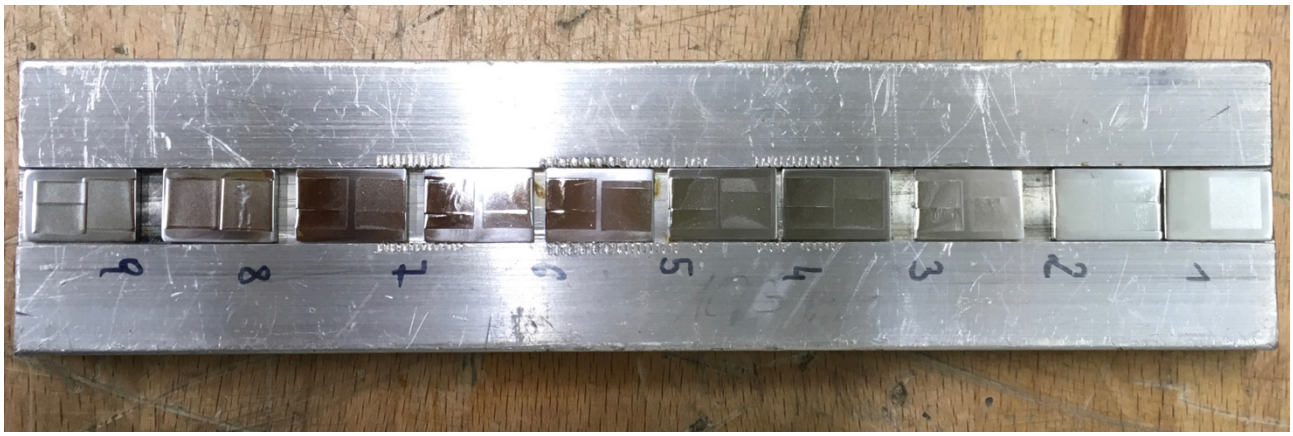

***Fig. 4.9*** *Microstructure on Ti-15Mo samples surface.*

## CUTTING SAMPLES

To get enough material on which to perform the numerous heat treatment experiments, the structured samples were cut by the *Struers Accutom-2* machine in order to obtain from each sample four pieces of approximately 3mm x 10mm (Ti-15Mo) and 3mm x 15mm (Ti-6Al-4V and Tigr2) in size (Fig.4.10).

The cutting plate used was a silicon carbide cut-off wheel 10S15 (HV 70-400) for soft non-ferrous metals.


***Fig. 4.10*** *Struers Accutom-2 machine.*

The part of the sample used to fix it to the machine (Fig. 4.11) has been discarded because of the damaged structured surface.

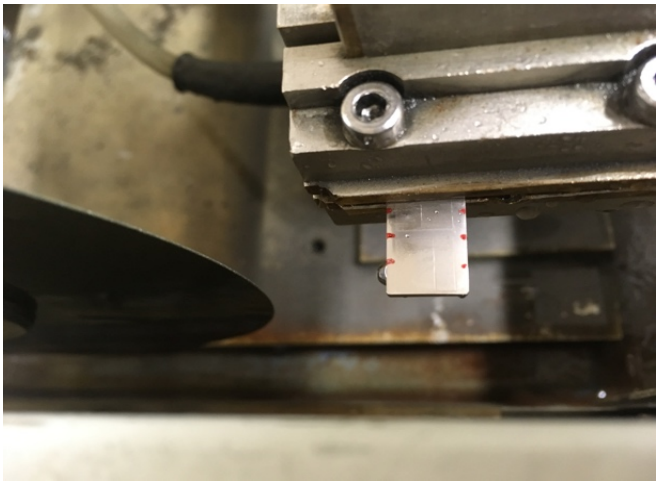

***Fig. 4.11*** *Sample fixed to the machine.*

After cutting, the samples have been cleaned with water and ethanol and then well dried (Fig. 4.12).

***Fig. 4.12*** *Cut samples.*

## THERMAL TREATMENTS

After EBW, the samples were subjected to heat treatment (HT) in order to investigate phase transformation and changes in microstructure. The aim of the process is to nanostructure the samples by the nucleation and formation of the alpha phase on the surface in different morphologies. In this way the samples will show a micro structure created by the EBW technique and a nano structure created by the HT.

The experiments were carried out using a dilatometer (Fig. 4.13), an instrument that measures volume changes caused by thermal process in this case.

***Fig. 4.13*** *Dilatometer.*

A thermocouple is welded on the surface of the sample at the microstructure. Subsequently the sample is placed inside a coil that generates heat, using an alternating electromagnetic field that generates a current flowing inside the sample.
The experiments were carried out in an inert atmosphere (vacuum at $5 \cdot 10^{-4}$mbar), after cleaning of chamber by flooding Argon, to avoid oxidation of the sample surface.

### HEAT TREATMENTS ON Ti6Al4V

- Heating rate: 300K/min
- Temperature: 1030°C (5min)
- Cooling rate: 100K/min or 200K/min

The HT temperature is higher than β-transus temperature (as reported in Tab.4.1), so after heating, the sample is characterized by β phase. The purpose of this treatment is to form stable α lamellar on the sample surface by moderate cooling. As reported in literature, a higher cooling rate will generate a finer lamellar structure.

- Heating rate: 300K/min
- Temperature: 720°C (2hs)
- Cooling rate: 200K/min

In this case, the HT temperature is lower than β-transus temperature (Tab.4.1); the HT is performed in the α+β field. The purpose is to stabilize the martensite microstructure by 720°C for 2 hours.

- Heating rate: 300K/min
- Temperature: 900°C (4hs)
- Cooling rate: 10K/min and 100K/min

The HT temperature in lower than β-transus temperature (Tab 1.4). The purpose is to evaluate the effect of the recrystallization on the martensite by the heat treatment.

A graph of the treatments on Ti6Al4V is shown below.

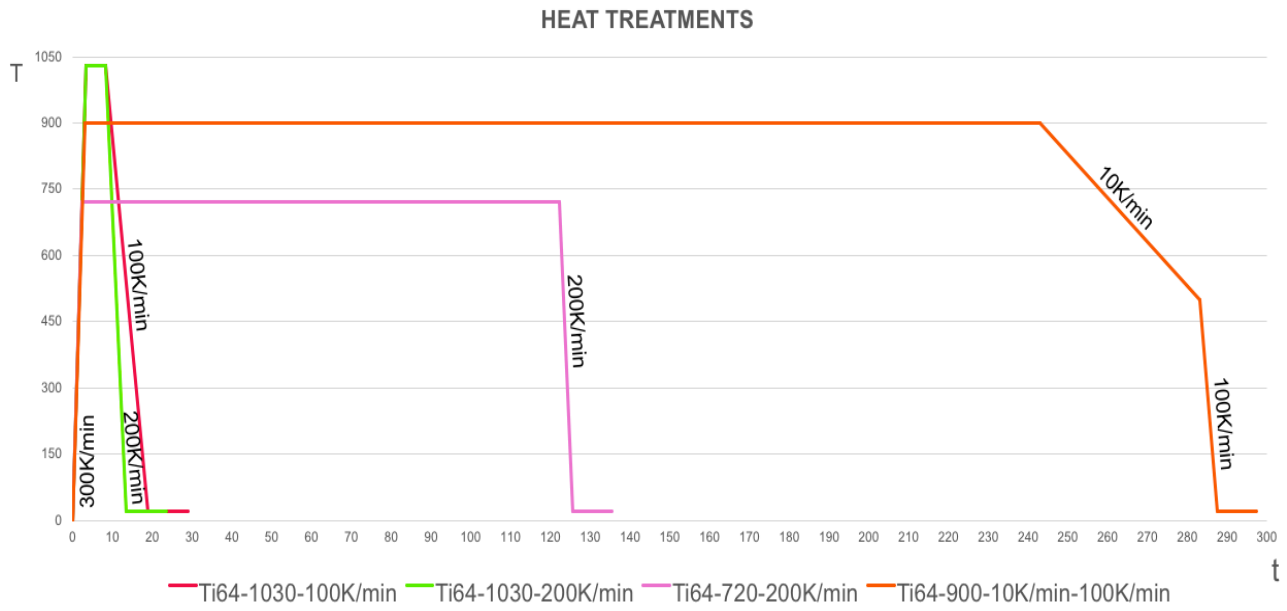


***Fig. 4.14*** *Heat Treatments on Ti6Al4V.*

## HEAT TREATMENTS ON Ti15Mo

- Heating rate: 5K/min or 300K/min
- Temperature: 550°C (4hs)
- Cooling rate: 200K/min

- Heating rate: 5K/min or 300K/min
- Temperature: 650°C (4hs)
- Cooling rate: 200K/min

Ti-15Mo is a metastable β alloy. The HT are performed to evaluate the influence of the heating rate and temperature on the precipitation of α in the β matrix.

## HEAT TREATMENTS ON Tigr2

- Heating rate: 300K/min
- Temperature: 950°C (5min)
- Cooling rate: 200K/min

The heat treatment takes place in the β field with a moderate cooling rate. The aim of the experiment is to determine if it is possible to dissolve the martensite present in the sample surface.

- Heating rate: 300K/min
- Temperature: 650K/min or 550K/min (2hs)
- Cooling rate: 200K/min

The HT temperature is lower than β-transus temperature, the purpose of the treatment is to stabilize the formed martensite on the sample surface.

## METALLOGRAPHY

To analyze the cross section of the material, the specimens were hot mounted using polyfast powder, a thermosetting resin, in *Struers citopress mounting press* (Fig. 4.15).

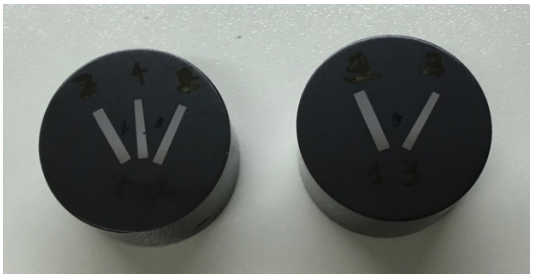

***Fig.4.15*** *Specimens mounted with polyfast powder.*

The samples were then fixed by sample holders (Fig.4.16) for *Struers Tegramin-30* machine, grinded and polished to make the sample's surface clearly visible.

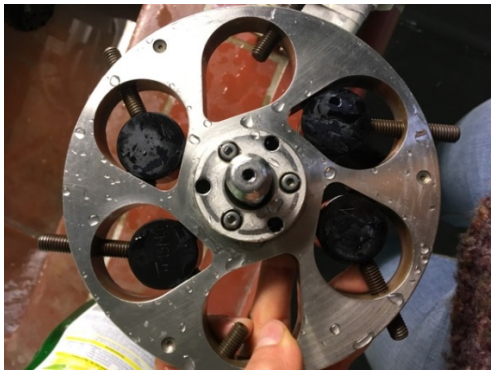

***Fig.4.16*** *Samples fixed by sample holder.*

Samples were grinded using silicon carbide abrasive papers with different grit sizes: P320, P800, P1200, P4000, increasing the process time from about 2 to 5 minutes. The force was set to 10N/sample and the speed to 150rpm.

The polishing step was carried out using firstly a Diamond 1µm cloth with a solution of Nap DiaDuo-2 for 5 minutes, and then a MD-chem cloth with a solution of OPS *Nondry* (non-drying colloidal silica suspension for final polishing) and distilled water, for about 10 minutes, using the same force and speed values as before.

At the end of the process, samples were cleaned with water and alcohol and well dried.

## ETCHING

The chemical etching has been used to enhance the effect of the nanostructure on Ti6Al4V samples. Etching selectively alters the microstructural features based on composition, stress, or crystal structure. The most common technique for etching is selective chemical etching. Hydrofluoric acid (HF) is the primary chemical needed to etch titanium.
The etching reaction is shown as:

$$Ti + 3HF \rightarrow TiF_3 + \frac{3}{2}H_2$$

The etching of titanium, with HF, produces titanium trifluoride and hydrogen gas. HF is usually combined with nitric acid. [109]

In this thesis, only hydrofluoric acid (HF) has been used as an etching agent, due to the preferential dissolution of the alpha phase of the biphasic alloy.
Various etching times and HF concentrations in distilled water were tested until optimal surface treatment was achieved.

The best result has been obtained using 1% HF in distilled water, and immersing the sample for 4 minutes in the solution in which another titanium sample was previously immersed for 4 minutes.

## FINAL POLISH

A final polishing process was made in order to remove the grooves made by Ebeam structuring, leaving the Heat Affected Zone microstructure visible. The goal of this final treatment is to evaluate the influence of the HAZ on cell and bacterial behavior. The polishing step was carried out using firstly a Diamond 1µm cloth with a solution of Nap DiaDuo-2 (a water-based diamond suspension without solvents) for 5 minutes, and then a MD-chem cloth with a solution of OPS *Nondry* (non-drying colloidal silica suspension) and distilled water, for about 10 minutes, using the following parameters:

- 150 rpm speed
- a force of 30 N (single specimen mode)
- Co-rotation of the plate and the metal disk.

. At the end of the process, samples were cleaned with water and alcohol and well dried.

## SAMPLE PREPARATION FOR BIOLOGICAL TEST

To carry out biological tests and surface characterizations, 37 Ti6Al4V samples were brought to Politecnico of Torino:

- 8 mirror polished samples

- 8 Ti6Al4V EB10µm
- 8 Ti6Al4V EB30µm
- 8 Ti6Al4V EB10µm HT (1030°C) called EB10HT or HT10 for reason of simplification
- 8 Ti6Al4V EB10µm HT (1030°C) + Etching called EB10HTEtch or HT10Etch for reason of simplification
- 7 P10µm (polished after EB structuring).

In order to eliminate contamination on the samples as a result of previous operations and transport, the samples were washed as follows.

The samples were immersed in acetone, taking care to position the structured part upwards and the unstructured part in contact with the beaker bottom. This operation was carried out under the fume hood and then the containers, covered with aluminum foil, were inserted into the ultrasonic bath for a period of 5 minutes. At the end of 5 minutes, the samples were transferred under the hood and immersed in a baker with ultrapure water. Bakers were then placed in the ultrasonic bath for 10 minutes. This last wash was repeated a second time with new ultrapure water.

The samples were then dried and placed in Petri dishes and sterilized in the furnace for 2 hours at 180 °C. At the end of the operation the samples were packed in sealed bags.

# CHARACTERIZATION METHODS

## SEM (Scanning Electron Microscope)

A scanning electron microscope is a type of microscope that scans a focused electron beam over a surface to produce an image. The image is the result of the interaction between the primary electrons in the beam and the sample, and it gives information about the surface topography and, when equipped with Energy Dispersive Spectroscopy (EDS), about semi-quantitative chemical composition (Fig.5.1).

The beam is generated by an electronic source, accelerated by an anode, concentrated by a series of electromagnetic lenses and deflected by an objective lens. The position of the beam on the sample is controlled by scan coils situated above the objective lens. These coils allow the beam to be scanned over the surface of the sample. The sample is mounted on a stage in the chamber area that is evacuated by a combination of pumps to work in high vacuum.

The electron beam penetrates the sample to a depth of a few microns, depending on the accelerating voltage and the density of the sample that responds by emitting a series of signals collected by one or more detectors to form images which are then displayed on the computer screen.

The most common SEM mode is the detection of secondary electrons emitted by atoms excited by the electron beam. The number of secondary electrons that can be detected depends, among other things, on specimen topography [110].

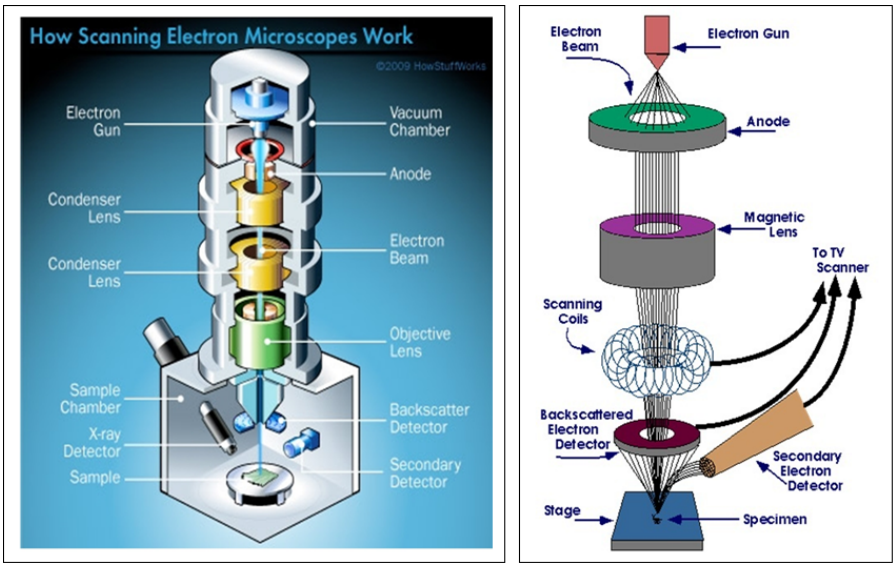


*Fig. 5.1 Scanning Electron Microscope [111].*

The electron microscope can achieve resolution better than 1 nanometer and was developed to overcome the limiting wavelength in light microscopes.

## FESEM (Field Emission Scanning Electron Microscope)

A FESEM is a microscope that works just like the SEM, but with higher resolution and a much greater energy range.

The primary electrons are emitted by an emission source, accelerated in a high electrical field gradient, focused and deflected by electronic lenses to produce a scan beam that bombards the sample. As a result secondary electrons are emitted with an angle and a velocity related to the surface structure of the sample. A detector catches the secondary electrons and produces an electronic signal that is amplified and transformed to an image.

A FESEM is used to visualize very small topographic details on the surface, and it may be employed for example to study organelles and DNA material in cell [112].

## LOM (Light Optical Microscope)

The optical microscope uses visible light and a system of lenses to magnify images of small subjects.

The eyepiece, or ocular lens, is a cylinder containing two or more lenses which function is to bring the image into focus for the eye.

The lens above the object, called the objective lens, collect light from the sample. By changing them it is possible to change the magnification. Most microscopes can magnify by 10, 20, 40, or 100 times, though professional ones magnifications up to 1000 times or more can be reached.

The specimen is supported by the stage, a platform below the objective, and it is illuminated by light that passes through a hole in the center of the stage.

Light microscope has a light source and a condenser, a lens designed to focus light from the illumination source onto the sample, in the same area that the objective lens examines (Fig.5.2) [113].

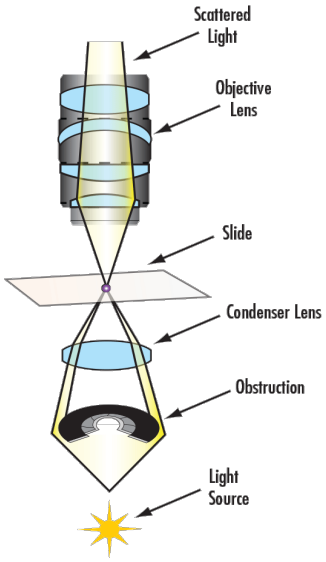


***Fig.5.2*** *Light Optical Microscope Scheme [114].*

## SURFACE ROUGHNESS

Roughness measurements are taken to describe the topography of a surface. Surface roughness has a significant influence on surface's wettability, so it can be important in determining the behaviour of cells and bacteria when they come into contact with the surface.

Ra is by far the most common roughness parameter used. It is defined as the arithmetic average of the absolute distances of the roughness profile to the mean line. The unit of Ra is micrometres.

$$\boldsymbol{Ra = \frac{1}{L}\int_0^L |y(x)|\ dx}$$

However, surface's profiles with the same Ra can present different trends, so the Ra value is not sufficient to completely define the morphological characteristics of the surface; for this reason, other parameters have been introduced, such as Rt (maximum height of the profile), Rz (average distance between 5 highest peak and 5 lowest valley) and Rq (the square mean of the deviation of the profile points from the midline). In Fig.5.3 are shown Ra and Rq. This parameter, being a quadratic average, is more sensitive to sharp deviation of the profile from a regular pattern and is generally higher than the Ra value [115].

$$\boldsymbol{Rq = \frac{1}{L}\int_0^L |y^2(x)|\ dx}$$

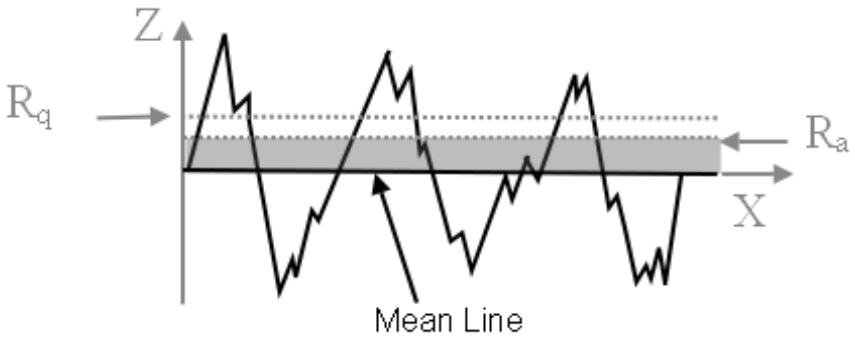


*Fig.5.3 Roughness parameters [116].*

Roughness measurements were carried out using the contact profilometer Talysurf Series-Taylor Hobson at the CNR in Turin.

The measurement were performed on the following sample:

- 2 Ti6Al4V MP (Mirror Polished)
- 2 Ti6Al4V EB 10
- 2 Ti6Al4V EB 30
- 2 Ti6Al4V HT10_1030°C_100K/min (structured + heat treated) called EB10HT or HT10 for reason of simplification
- 2 Ti6Al4V ETCH (structured + heat treated + etched) called EB10HTEtch or HT10Etch for reason of simplification
- 1 Ti6Al4V P10 (structured + polished)

The the 2D and 3D reconstruction of the sample's surfaces were obtained using the optical profilometer *Talysurf CCI 3000* at CNR in Turin.

The surface reconstructions were realized on the following samples:

- Ti6Al4V EB 10
- Ti6Al4V EB 30
- Ti6Al4V HT10_1030°C_100K/min (structured + heat treated) called EB10HT or HT10 for reason of simplification
- Ti6Al4V ETCH (structured + heat treated + etched) called EB10HTEtch or HT10Etch for reason of simplification
- Ti6Al4V P10 (structured + polished)

## CONTACT ANGLE

The Contact angle is the angle formed by a liquid where a liquid, gas and solid intersect. It is widely used to measure the wettability of a surface. The balance at the three phase contact is described by Young equation:

$$\gamma_{SV} = \gamma_{SL} + \gamma_{LV} cos\theta_Y$$

where $\gamma_{SV}, \gamma_{SL}$ and $\gamma_{LV}$ are the interfacial tensions between the three phases liquid, gas and solid, and $\theta_Y$ is the contact angle.

If the contact angle is less than 90° the liquid spreads on the surface; zero contact angle representing complete wetting (hydrophilic surface). If contact angle is greater than 90°, the surface is non-wetting with that liquid (hydrophobic surface) as shown in Fig.5.4 [117].

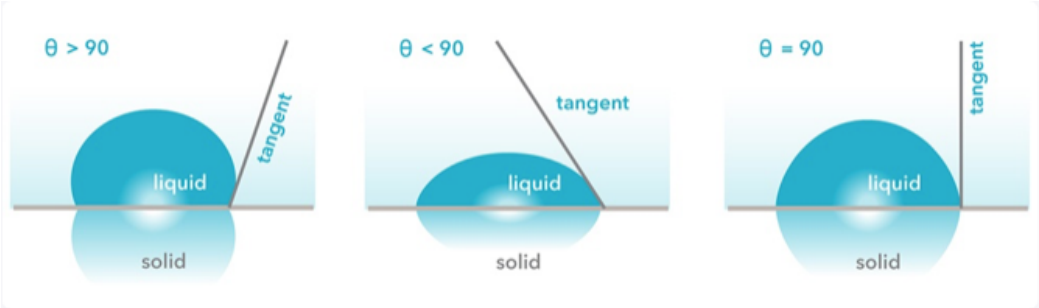


***Fig.5.4*** *Contact angle values [118].*

Wettability measurements were carried out using the optical microscope Kruss DSA 100. The equipment used consists of a support plate for the sample, on which a liquid drop is placed through a micrometric pipette, a light source and a telescope connected to the software. The two-dimensional image and contact angle measurement are reconstructed by software. The liquid used for this test was distilled water. A constant drop of volume was created (5µL), placed on the sample surface and a static contact angle was measured. On each sample type, different measurements were carried out by placing several drops on the surface of the samples.

The measures were performed on the following samples:

- 2 Ti6Al4V MP
- 2 Ti6Al4V EB 10
- 2 Ti6Al4V EB 30
- 2 Ti6Al4V HT10_1030°C_100K/min (structured + heat treated) called EB10HT or HT10 for reason of simplification

- 2 Ti6Al4V ETCH (structured + heat treated + etched) called EB10HTEtch or HT10Etch for reason of simplification
- 2 Ti6Al4V P10 (structured + polished)

## XRD

X-ray diffraction is a non-destructive techniques used to identify and characterize the materials based on their diffraction pattern, and to obtain information about their crystal structure, chemical composition, and physical properties of materials.

X-ray diffraction is based on constructive interference of monochromatic X-rays and a crystalline sample. The X-rays are generated by a cathode ray tube by heating a filament to produce electrons, accelerated toward a target by applying a voltage, filtered to produce monochromatic radiation, collimated to concentrate, and directed toward the sample. When electrons have sufficient energy to dislodge inner shell electrons of the target material, characteristic X-ray spectra are produced.

The interaction of the incident rays with the sample produces constructive interference (and a diffracted ray) when conditions satisfy Bragg's Law (Fig.5.5)

$$n\lambda=2d\sin\theta$$

- $\theta$ is the angle which the outgoing beam forms with the crystalline plane;
- $\lambda$ is the wavelength of the radiation;
- $d$ (d-spacing) is the distance between two adjacent planes;
- $n$ indicates the order of diffraction.

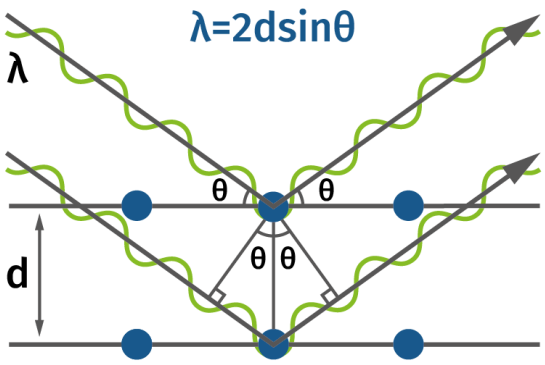


*Fig.5.5 X-ray diffraction from crystal lattice planes (Bragg´s law) [119].*

This law relates the wavelength of electromagnetic radiation to the diffraction angle and the lattice spacing in a crystalline sample. The intensities of the diffracted waves depend on the kind and arrangement of atoms in the crystal structure.

These diffracted X-rays are then detected, processed and counted.

By scanning the sample through a range of 2θangles, all possible diffraction directions of the lattice should be achieved due to the random orientation of the material.

Conversion of the diffraction peaks to d-spacings allows identification of the mineral because each mineral has a set of unique d-spacings. Typically, this is achieved by comparison of d-spacings with standard reference patterns.

The instrument works as follows: a beam of parallel and monochromatic X-rays (with defined λ) affects the sample, the radiations diffracted by the sample are collected by a detector that transforms them into electrical pulses, which are then amplified and sent to a computer that allows processing (Fig.5.6) [119].

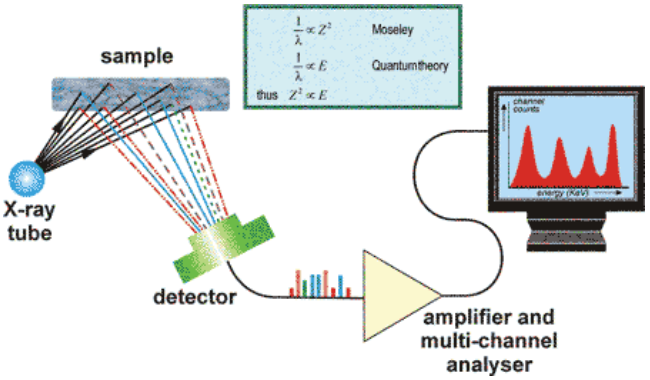


*Fig.5.6 XRD operating scheme.*

# BIOLOGICAL CHARACTERIZATION

## CYTOCOMPATIBILITY

### CELLS

Specimens' cytotoxicity was evaluated on pooled primary human gingival fibroblasts (HGFs). HGFs were isolated from discarded normal human gingiva, surgically resected from healthy patients. All subjects gave informed consent to participate to the study, which was conducted according to the Declaration of Helsinki. Briefly, thin sheets of mucosa were removed using a dermatome, and the epithelial layer was enzymatically detached through simple digestion with 0.5% dispase at 4 °C O/N. The dermal layer was then minced with surgical blades and digested for 30 min at 37 °C with a collagenase/dispase/trypsin solution (1 mg mL−1 collagenase, 0.3 mg mL−1 dispase, 0.25% trypsin in PBS, all from Sigma-Aldrich). Cells were then cultivated in α-MEM (Sigma-Aldrich) supplemented with 10% heat-inactivated fetal bovine serum FBS (Sigma-Aldrich) and 1% antibiotics-antimycotics (Anti-Anti, Sigma-Aldrich) at 37 °C in a humidified 10% CO2 atmosphere. Before confluence, both cell types were trypsinized, re-suspended, plated for the experiments, and used within fifteen population doublings.

### DIRECT METABOLIC EVALUATION

Specimens aimed for biological assays were previously sterilized by means of heating treatment for 2 hours at 180°C in the oven. Sterile specimens were gently located into a 12 multiwell (Nunc Delta Surface, Thermo Fisher, MA, USA) plate by sterile tweezers avoiding any surface damages. Then, $2x10^4$ cells/specimens were dropwise (50 µl) seeded directly onto specimens' surface and allowed to adhere for 2 hours; afterwards, 1,5 ml of fresh medium was gently spotted into each well to fill specimens. Cells were cultivated for 2 days onto specimens' surface and viability evaluated at each time point by the Alamar blue assay (alamar Blue®, Thermo Fisher, MA, USA) following Manufacturer's instructions. Briefly, at each time-point, supernatants were removed from each well containing cells and replaced with alamar blue solution (10% v/v in fresh medium). Plates were incubated in the dark for 4 h and then 100 µL were removed, spotted into a new 96-well plate and fluorescence signals were evaluated with a spectrophotometer (Victor, Perkin Elmer, Waltham, MA, USA) at 590 nm. Experiments were performed in triplicate.

### MORPHOLOGICAL EVALUATION

After 48 h of direct cultivation, morphology of the cells grown onto the grooved specimens was investigated by field emission scanning electron microscopy (FESEM, Supratum40, Zeiss) and immunofluorescence (IF) staining. Briefly, the cells were fixed with 3% paraformaldehyde (Sigma-Aldrich), in PBS, for 2 hs, then washed in 1 mol l−1 sodium cacodylate buffer, dehydrated with 70%, 80%, 90%, and 100% ethanol (10 min each). The specimens were positioned on aluminium stubs using conductive carbon tape, then covered with a chromium layer and observed by FESEM (SUPRATM 40, Zeiss) at various magnifications.

To assay IF staining, the cells were fixed with 3% paraformaldehyde for 20 minutes at room temperature, washed gently with PBS and stained with an anti-vinculin (AbCam, 1:200 in PBS, 5% goat serum, 1% BSA) and anti-collagen type III (AbCam, 1:200 in PBS, 5% goat serum, 1% BSA) for 2h at room temperature. Then, the cells were stained with an appropriate secondary anti body (45 min room temperature) and finally co-stained with phalloidin (AbCam, 1:500 in PBS) and 4,6-diamidino-2-phenylindole (DAPI, Sigma) to visualize cytoskeleton f-actins and nuclei. The specimens were analysed by using a fluorescent microscope (Leica 6500, Leica Microsystems, Basel, Switzerland).

## ANTIBACTERIAL ACTIVITY

### STRAIN

The orthopedic-infections related strong biofilm former strain *Staphylococcus aureus* (SA, commercial, multi-drug resistant, ATCC 43300), was used to assay specimens' antibacterial efficacy. SA was cultivated into selective blood agar medium (from Sigma Aldrich); bacteria were cultivated at 37°C until single round colonies were formed onto the agar surface. Plate were maintained at 4°C prior to experiments; fresh broth-cultures were prepared prior to each experiment by dissolving 2–3 colonies in 30 ml of each specific medium. Bacteria concentration was adjusted until $1x10^5$ cells/ml by diluting in fresh media until optical density of 0.001 at 600 nm was reached as determined by spectrophotometer (Victor, Packard Bell, LA, USA).

### BIOFILM FORMATION

Sterile specimens were gently located into a 12 multiwell plate by sterile tweezers avoiding any surface damages. Each specimen was submerged with 1 ml of the broth bacteria culture prepared as prior described; plate was incubated for 90 minutes in agitation (120 rpm) at 37°C to allows the separation between adherent biofilm cells and not-adherent floating planktonic cells (separation phase). Afterwards, supernatants containing planktonic cells were removed and replaced with 1 ml

of fresh media to cultivated surface-adhered biofilm cells (growth phase). Biofilm were grown at 37°C for 1-2-3 days prior to evaluations.

### BIOFILM METABOLIC EVALUATION

At each time points, biofilm metabolic activity was evaluated by the alamar blue assay as prior described in the cytocompatibility paragraph. Briefly, specimens were gently washed with sterile PBS (1ml each) 3 times to remove non-adherent cells; then, specimens were moved to a new 12 multiwell plate and the alamar blue solution (prepared in LB medium) was added to each well for 4 hours in the dark. Optical density was evaluated by spectrophotometer (Victor, Perkin Elmer, Waltham, MA, USA) at 590 nm. Experiments were performed in triplicate.

After 72h of direct contact, colony forming unit (CFU) were counted. Briefly, bacteria were detached from the specimen surface by vortex and sonicator (3 times, 30 seconds each) and then 100 µl of supernatant were collected from each well and used to perform six-serial ten-fold dilutions, mixing 20 µl of bacterial suspension with 180 µl of sterile saline (0.9% NaCl). Twenty µl were then collected from each dilution, spotted onto plates containing LB agar medium, and incubated for 24h at 37°C. CFU m were counted as follows:

$$CFU = [(number\ of\ colonies \times diluon\ factor)^{(serial\ dilution)}]$$

### BIOFILM MORPHOLOGY EVALUATION

After 3 days culturing the morphology of adhered biofilm was visually checked by FESEM as prior described in the cytocompatibility section. Briefly, specimens were gently washed with sterile PBS (1ml each) 3 times to remove non-adherent cells; then, cells were fixed with 3% paraformaldehyde (Sigma-Aldrich), in PBS, for 2 hs, then washed in 1 mol l−1 sodium cacodylate buffer, dehydrated with 70%, 80%, 90%, and 100% ethanol (10 min each). The specimens were positioned on aluminium stubs using conductive carbon tape, then covered with a chromium layer and observed by FESEM (SUPRATM 40, Zeiss) at various magnifications.

## STATISTIC ANALYSIS

A statistic analysis was performed using One-way ANOVA with post-hoc Tukey HSD Test Calculator to compare the different treatments carried out on the samples.

# RESULT AND DISCUSSION

## ELECTRON BEAM STRUCTURING RESULTS

After structuring with electron beam technique, FESEM and LOM (Light Optical Microscope) were used to observe the morphological modifications obtained by structuring on the specimens' surfaces.

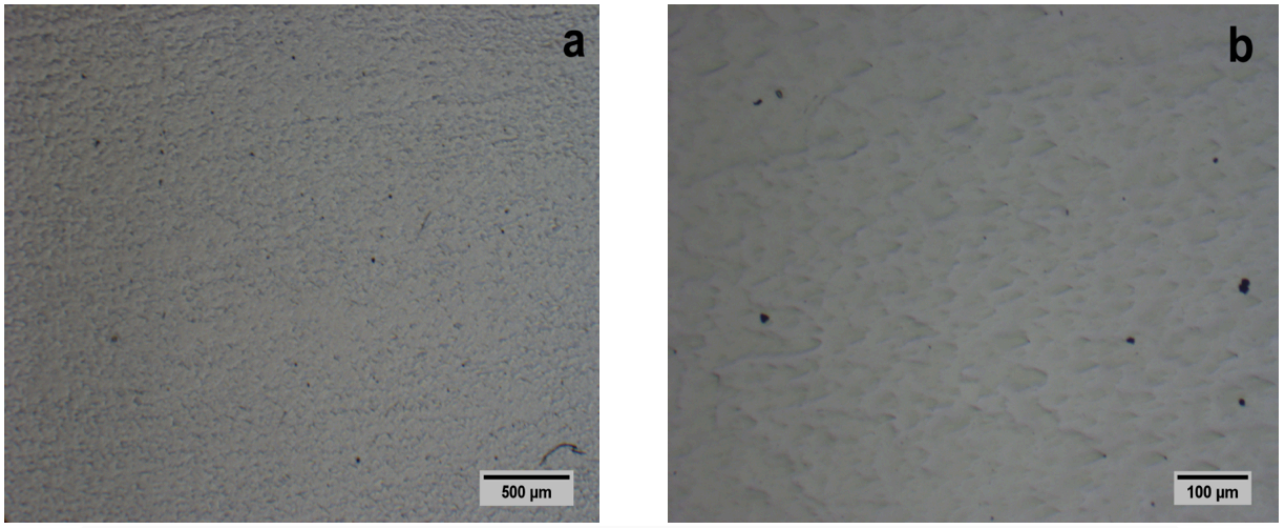


***Fig.6.1*** *Ti6Al4V MP surface microstructure and micro topography (LOM): 50x mag. (a); 200x mag. (b).*

The mirror-polished MP sample (Fig.6.1) has a homogeneous surface, which shows the marks left by the polishing process.

Regarding Ti6Al4V, 5,10 and 30 µm parallel grooves were produced.

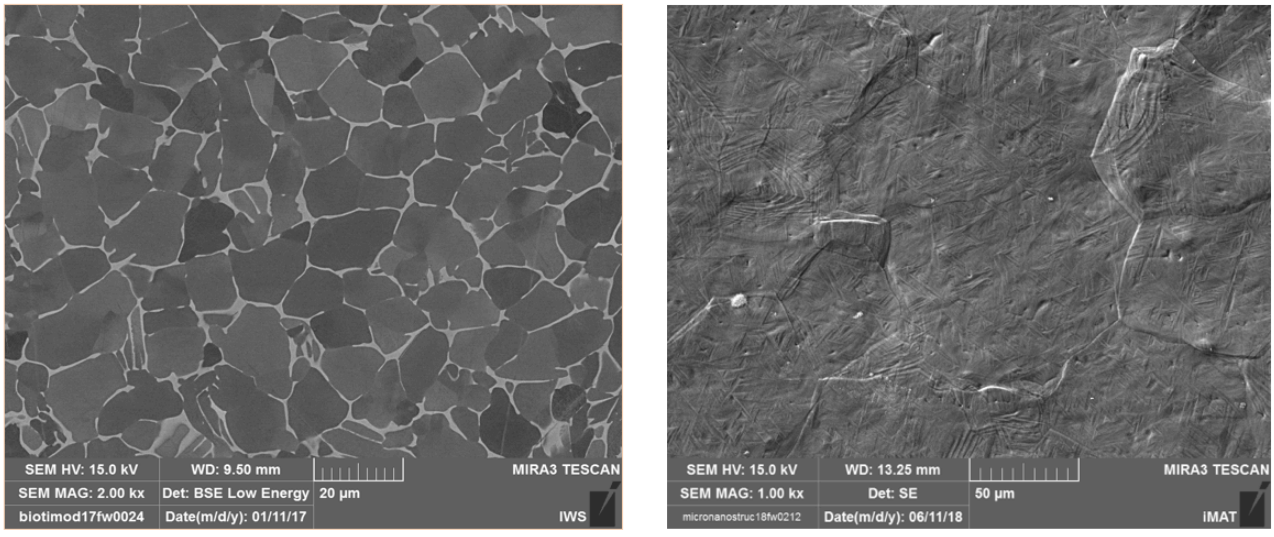


***Fig.6.2*** *Ti6Al4V as received microstructure (on the left); Ti6Al4V 5µm grooves tilt 20° (mag.1000x)(on the right).*

From FESEM image (Fig.6.2 right) it is possible to see the grain's boundaries corresponding to the β grains which were formed at high temperature and martensitic microstructure, nevertheless the

5µm sized grooves created with E-beam Structuring are not visible using FESEM technique even by tilting the specimen (20° in this case).

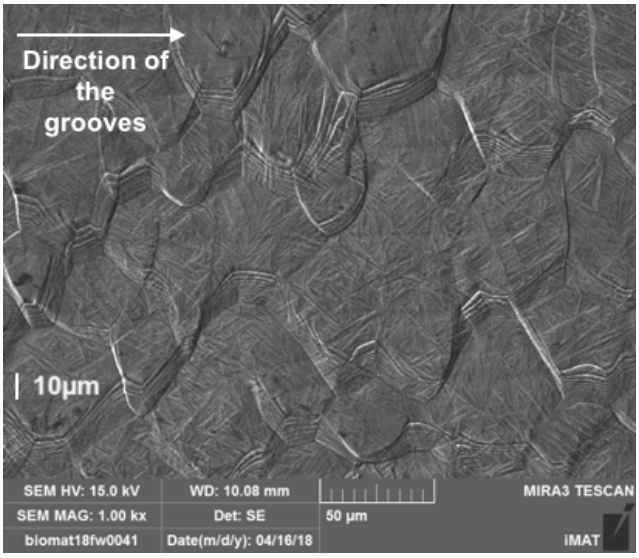


***Fig.6.3*** *Ti6Al4V 10µm grooves tilt 0° (mag.1000x).*

As the previous one, Ti6Al4V sample with 10µm grooves is characterized by prior β grains with very fine needle-like martensitic inside (Fig.6.3). To better observe the grooves it has been necessary to tilt the sample by 60° (Fig.6.4).

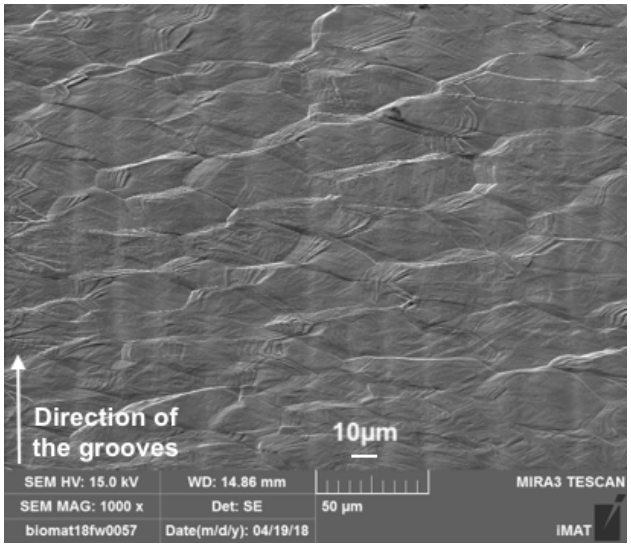


***Fig.6.4*** *Ti6Al4V 10µm grooves tilt 60° (mag.1000x).*

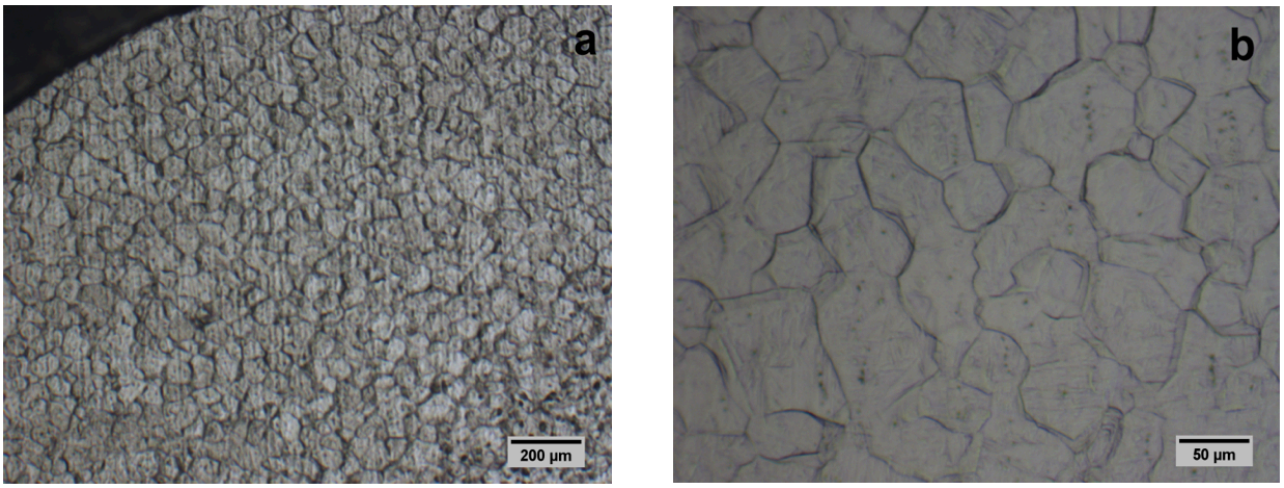


*Fig.6.5 EB10 microstructure and micro topography (LOM): 50x mag. (a); 200x mag. (b).*

On the surface of the sample structured with e-beam (Fig 6.5), it is also possible to well identify the grooves by optical microscopy. The microstructure presents prior β grains with martensitic structure, as already observed at FESEM.

The same microstructure is also present in Ti6Al4V with 30µm grooves, observed through tilting by 60° (Fig.6.6).

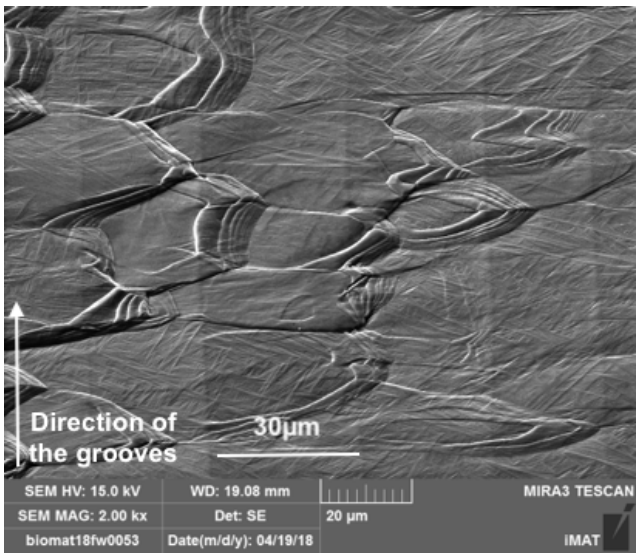


*Fig.6.6 Ti6Al4V 30µm grooves tilt 60° (mag.2000x).*

Setting 30µm as grooves dimension, resulting in a more visible topography than 10µm one, even without tilting the sample (Fig.6.7).

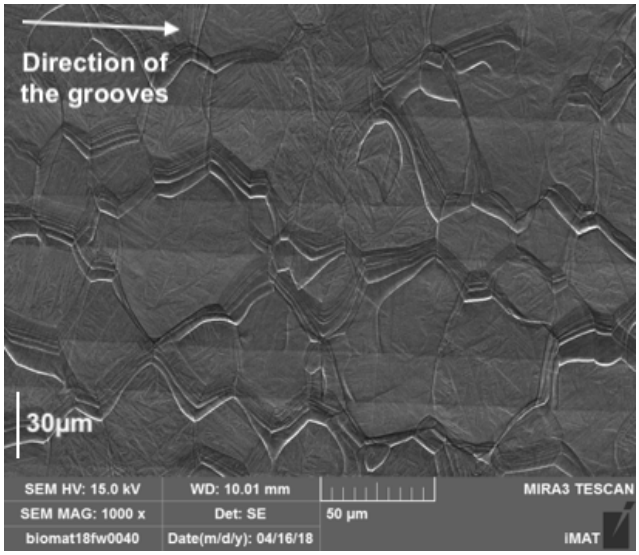


***Fig.6.7*** *Ti6Al4V 30µm grooves tilt 0° (mag.1000x).*

In the figure 6.7, it can be clearly observed that the grooves do not have a costant size; the cause of this effect is unclear.

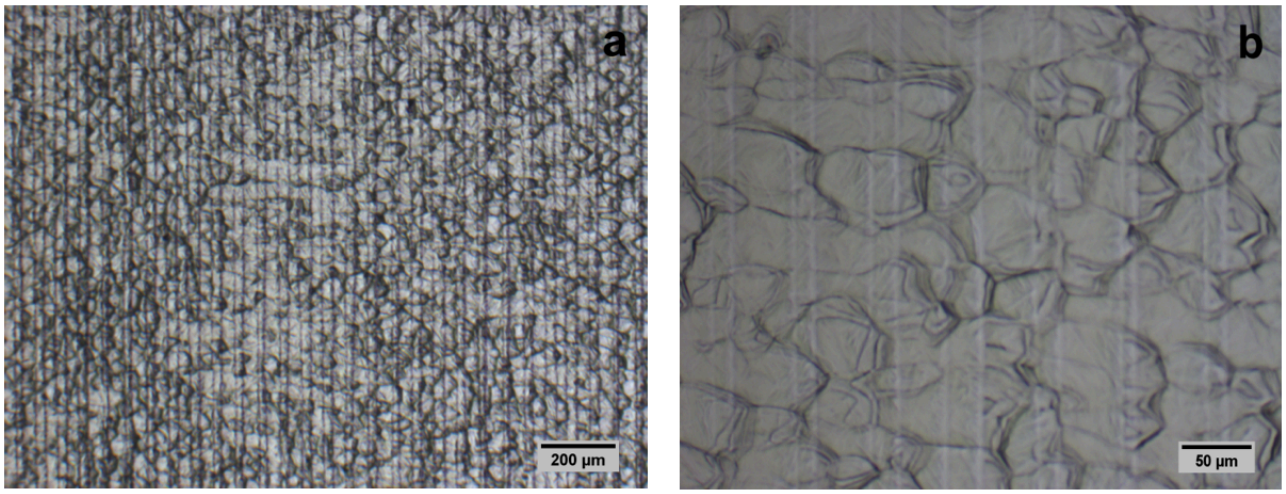


***Fig.6.8*** *EB30 microstructure and micro topography (LOM): 50x mag. (a); 200x mag. (b).*

The sample EB30, structured with E-beam, (Fig.6.8) shows at LOM observation the same microstructural and surface topographic features of EB10 sample, but changes for grooves that are spaced 30micron.

For Ti15Mo and Ti grade 2 substrates, the electron beam structuring effect has already been previously studied, in particular to see the microtopographic changes on the sample's surfaces with grooves spaced 10 and 30µm.

In this work, the electron beam technique was used on Ti15Mo surface to verify the actual success of the structuring with 5µm sized grooves. The grooves are slightly visible on some areas (Fig.6.9), but they are not homogeneously distributed.

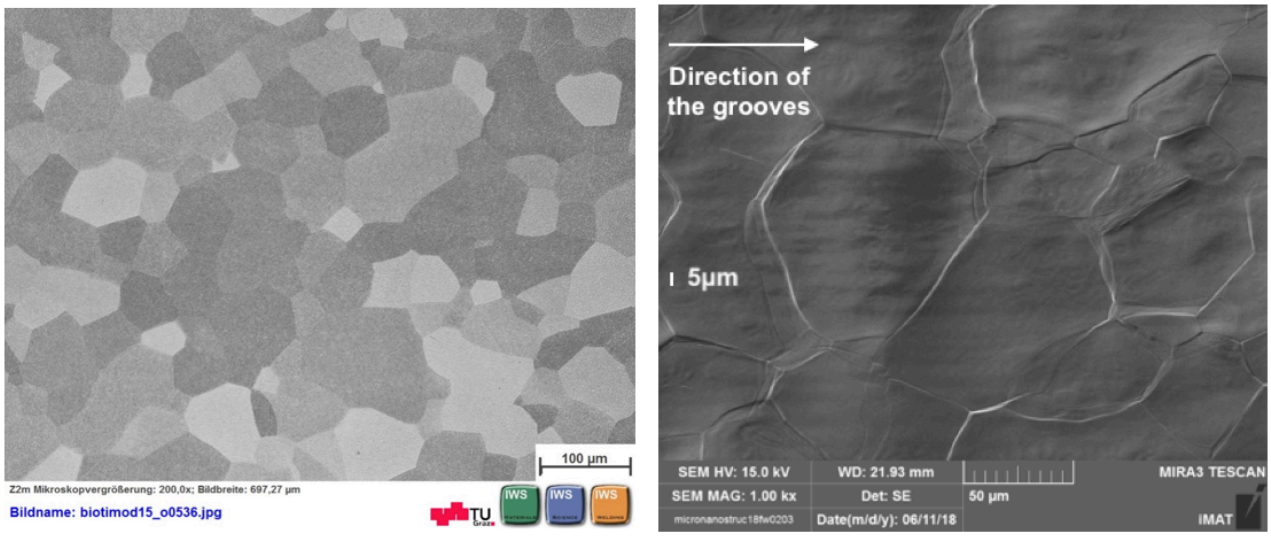


***Fig.6.9*** *Ti15Mo base material (on the left); Ti15Mo EB 5µm tilt 40° (on the right).*

The FESEM image (Fig.6.9) shows the presence of the β grains and relative grain boundaries.
By increasing the magnification it is possible to observe the formation of a particular nanotopography (Fig.6.10).

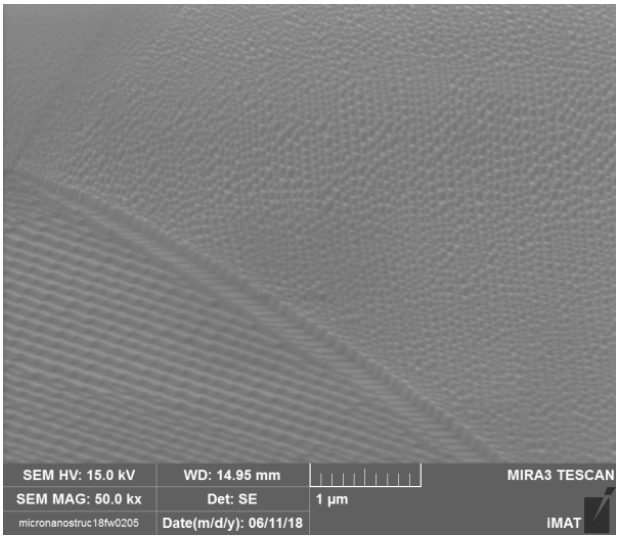


***Fig.6.10*** *Ti15Mo EB 5µm tilt 60° (mag.50000x).*

## HEAT TREATMENTS RESULTS

The various heat treatments were carried out after structuring, in order to obtain different micro and nano structures, as can be seen in the following FESEM images.

### Ti6Al4V

- Heating rate: 300K/min
- Temperature: 1030°C (5min)

- Cooling rate: 100K/min

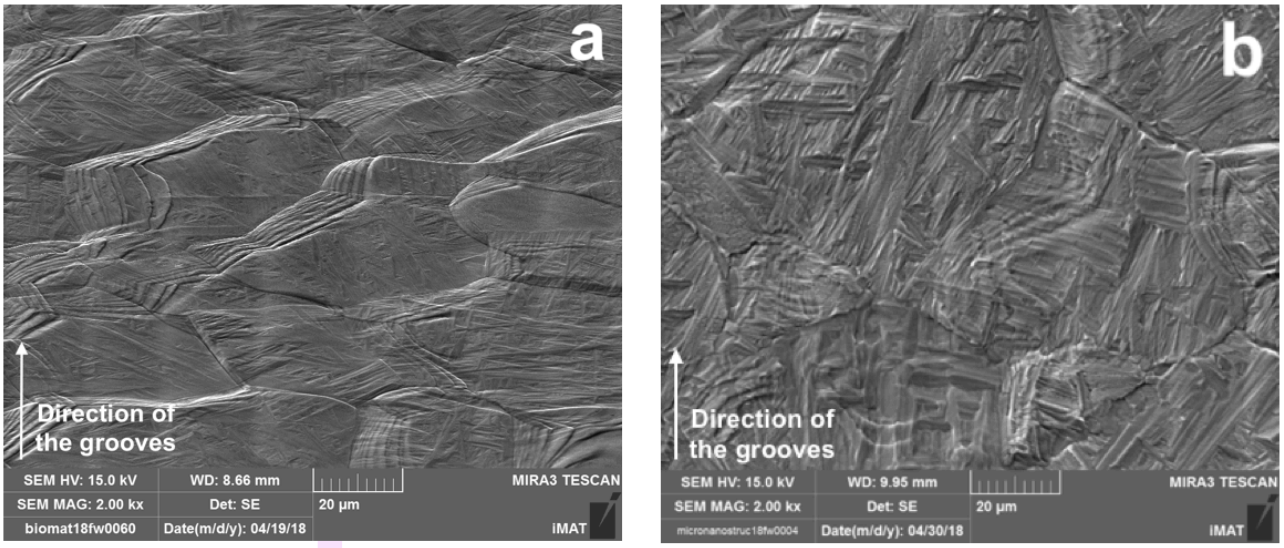


***Fig.6.11*** *Ti6Al4V EB10µm (a) Ti64_1030°C (5min)_100K/min EB10µm Tilt 20° (b).*

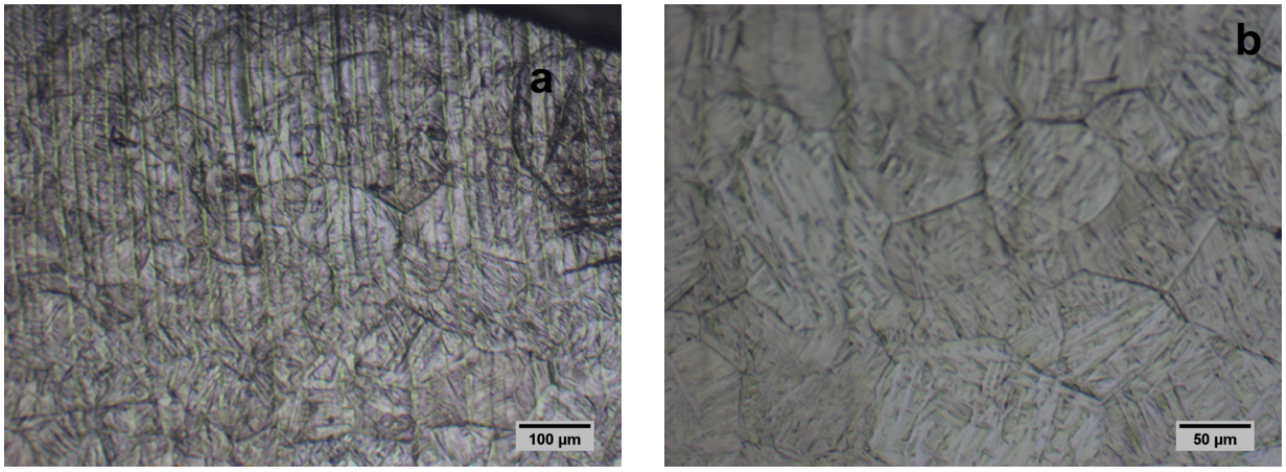


***Fig.6.12*** *Ti64 EB10_1030°C (5min)_100K/min microstructure and micro topography (LOM): 100x mag. (a); 200x mag. (b).*

As reported in literature, after cooling from the β field, α lamellae colonies formed into β prior grain (Fig.6.11 and Fig.6.12), starting to nucleate from grain boundaries to the center of the grain. The 10µm spaced grooves are clearly visible.

- Heating rate: 300K/min
- Temperature: 1030°C (5min)
- Cooling rate: 200K/min

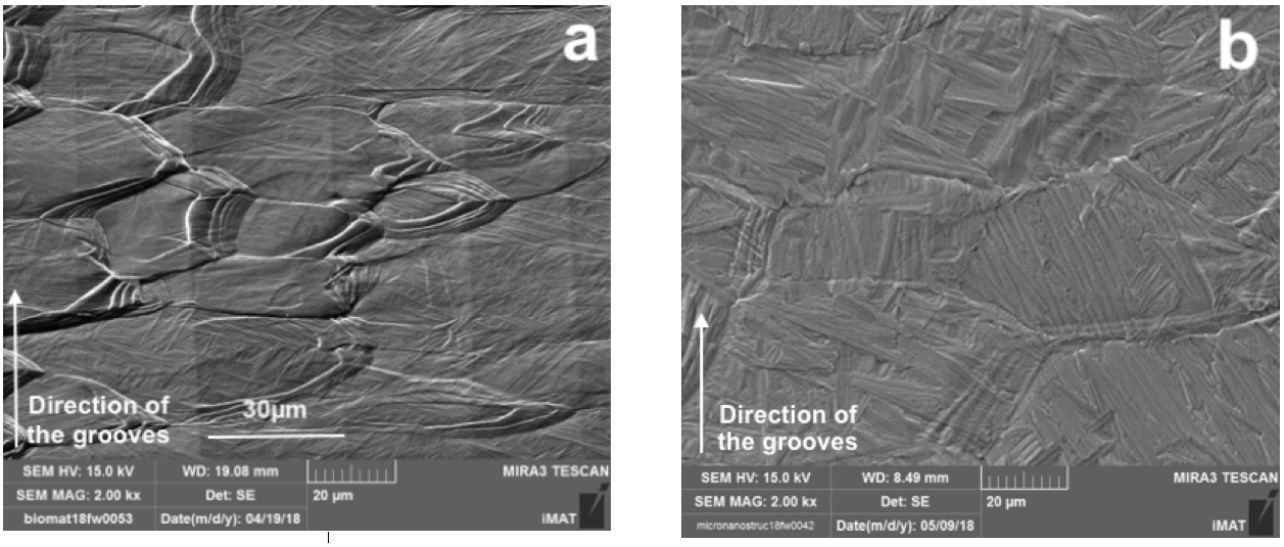


***Fig.6.13*** *Ti6Al4V EB30µm (a) Ti64_1030°C (5min)_200K/min EB30µm Tilt 20° (b).*

A similar structure was obtained using 200K/min as cooling rate. The difference is that α lamellae and α lamellar colonies became coarser by decreasing the cooling rate from 200K/min to 100K/min (Fig.6.13 and Fig.6.11). The lamellar structure obtained (Fig.6.11 and Fig.6.13) cannot be defined as a Widmanstätten structure because the cooling rate is too high.

- Heating rate: 300K/min
- Temperature: 720°C (2hs)
- Cooling rate: 200K/min

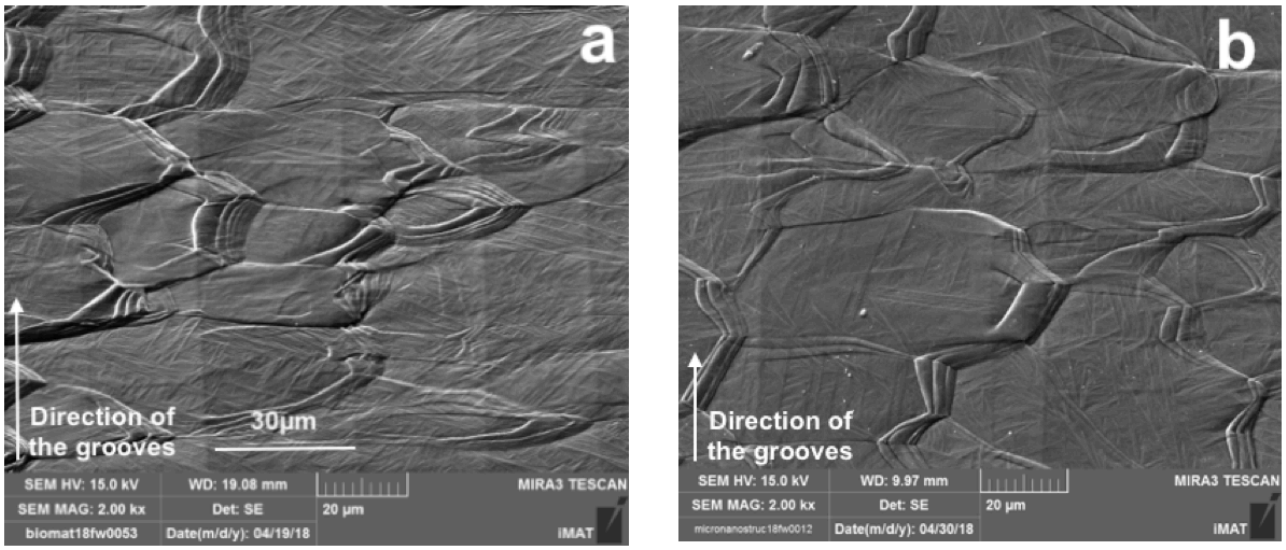


***Fig.6.14*** *Ti6Al4V EB30µm (a) Ti64_720°C (2hs)_200K/min EB30µm Tilt 40° (b).*

Cooling from below β-transus temperature results in a microstructure characterized by prior β grains and very fine martensite (Fig.6.14). This is a heat treatment to relieve the stresses produced by the martensitic transformation through rapid cooling. This HT was carried out to produce a

diffusion process to stabilize alpha and beta phase keeping the morphology of martensite. Hardness should decreases but the toughness should increase. In addition, a fast cooling rate, in vacuum, permit to avoid gases for quenching and thus contamination of the surface.

- Heating rate: 300K/min
- Temperature: 900°C (4hs)
- Cooling rate: 10K/min and 100K/min

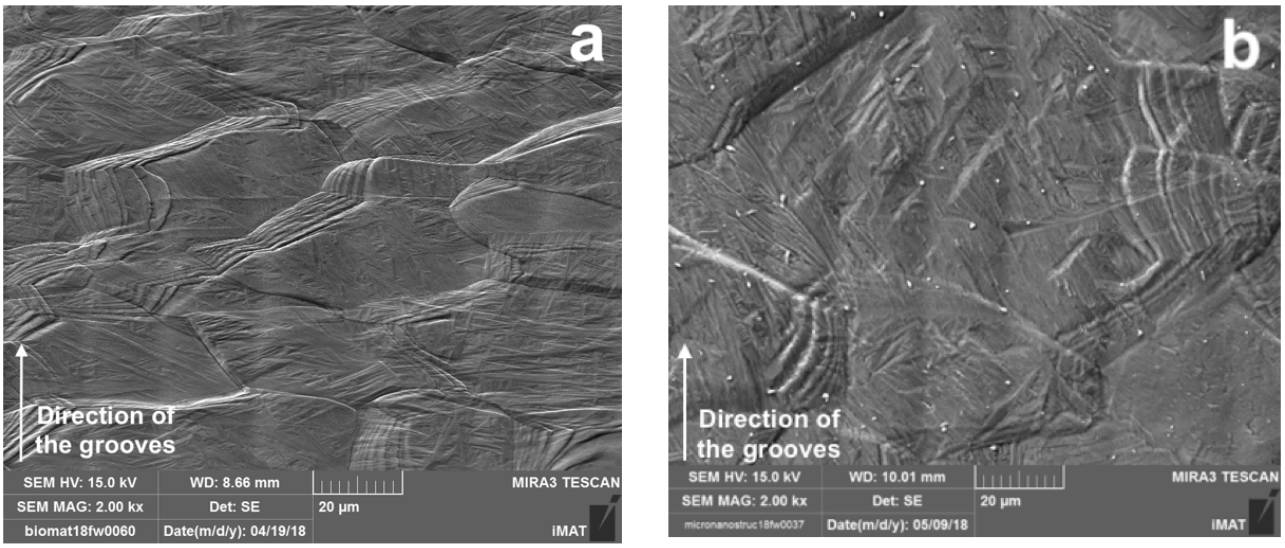


***Fig.6.15*** *Ti6Al4V EB10µm (a) Ti64_900°C (4hs)_10K/min_100K/min EB10µm Tilt 20 °.*

The microstructure presents prior β grains and martensite (Fig.6.15). The small white dots are dirt residues probably due to residues of OPS *Nondry* used for polishing. The size of the grains after this heat treatment does not change substantially. It changes from from about 40-60µm in EB10 to about 80-100µm

The effect of this heat treatment is reflected on the sample structure that show an interesting nanotopography due to the recrystallization effect (Fig.6.16).

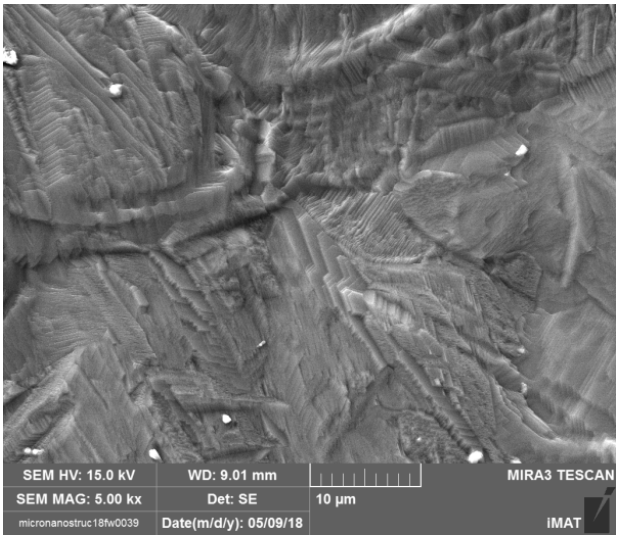


***Fig.6.16*** *Ti64_900°C (4hs)_ 10K/min_100K/min EB10µm Tilt 20 °,detail.*

## Ti15Mo

- Heating rate: 5K/min or 300K/min
- Temperature: 650°C (4hs)
- Cooling rate: 200K/min

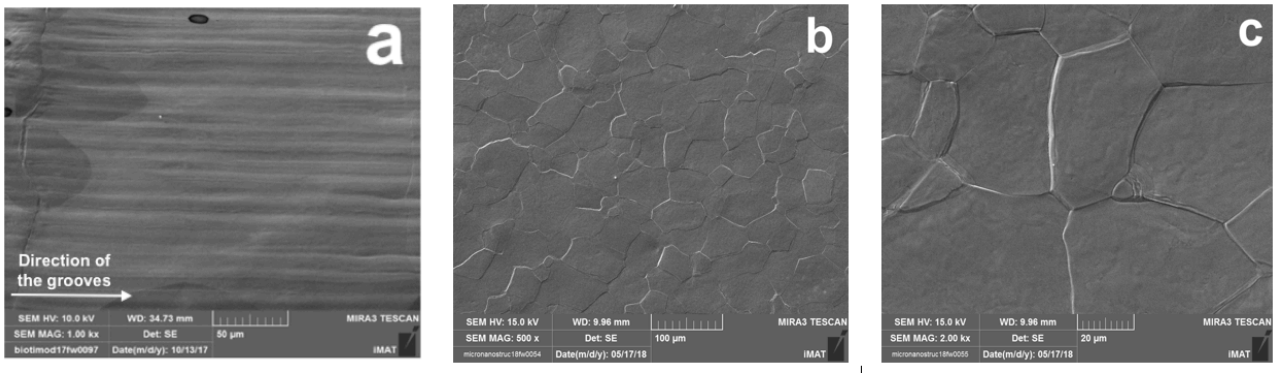


***Fig.6.17*** *Ti15Mo EB10µm (a) Ti15Mo EB10µm 300K/min 650°C 4hs Tilt 20° a different magnification (b and c).*

From FESEM images (Fig.6.17) it is possible to see very well the β grains but not the α phase, which according to literature should nucleate after the heat treatment.

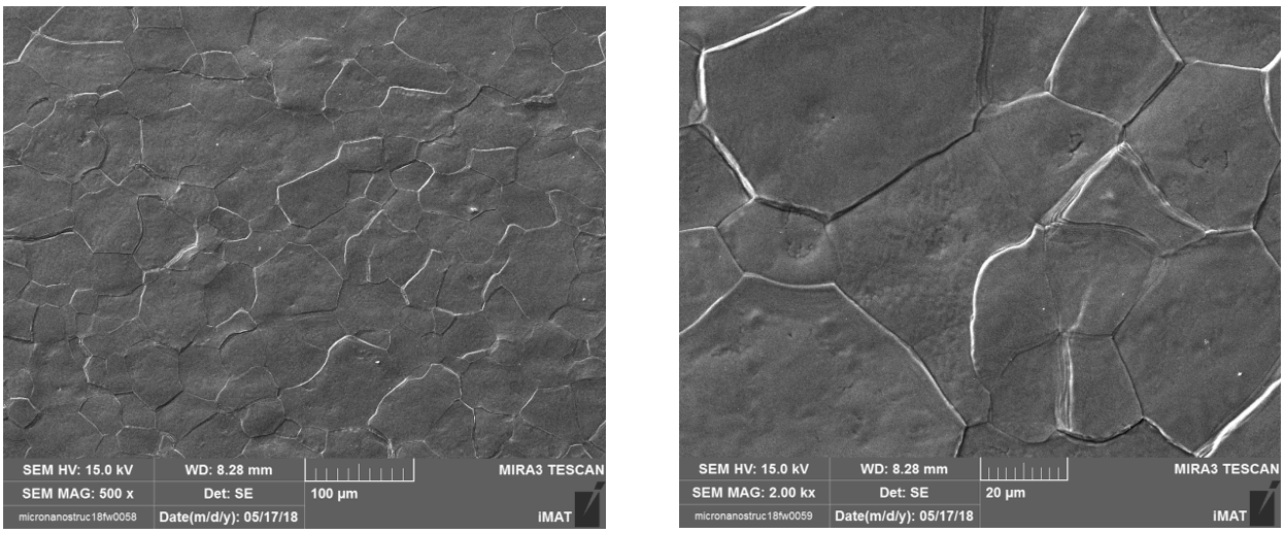


***Fig.6.18*** *Ti15Mo EB10µm 5K/min 650°C 4hs Tilt 20° a different magnification.*

An analogous result was obtained by decreasing the heating rate from 300K/min to 5K/min (Fig.6.18).

## Ti grade2

- Heating rate: 300K/min
- Temperature: 950°C (5min)
- Cooling rate: 200K/min

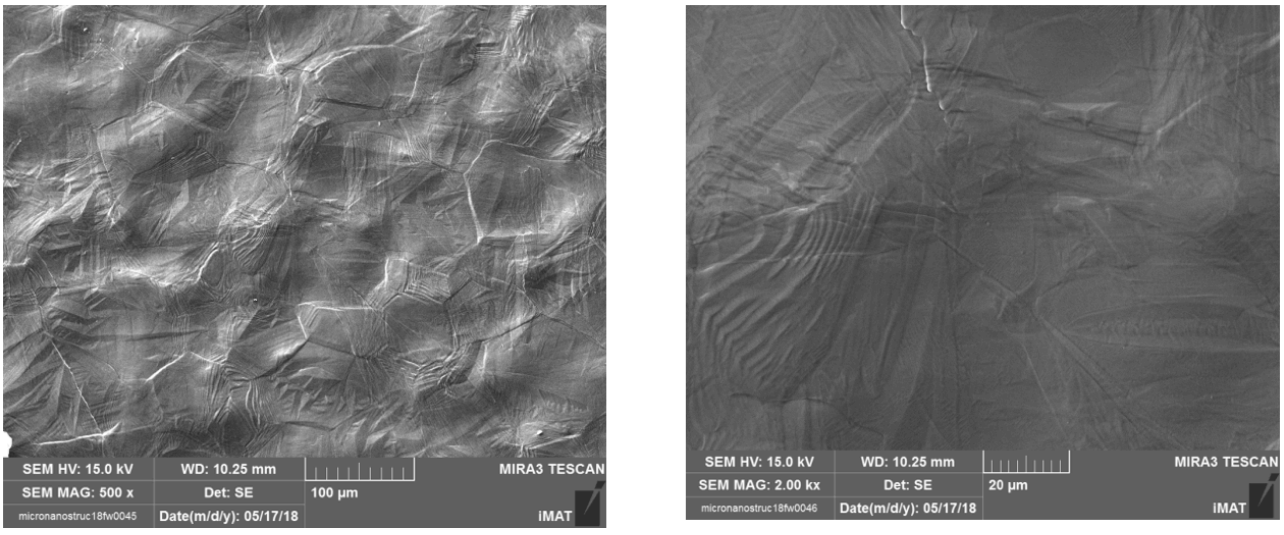


***Fig.6.19*** *Tigr2 EB10µm 950°C 5min 200K/min Tilt 20°.*

The heat treatment was carried out to understand if it was possible to remove the martensite from the surface of the sample. As shown by the FESEM images the result was unsatisfactory, as martensite is still present on the surface (Fig.6.19).

- Heating rate: 300K/min
- Temperature: 650K/min or 550K/min (2hs)

- Cooling rate: 200K/min

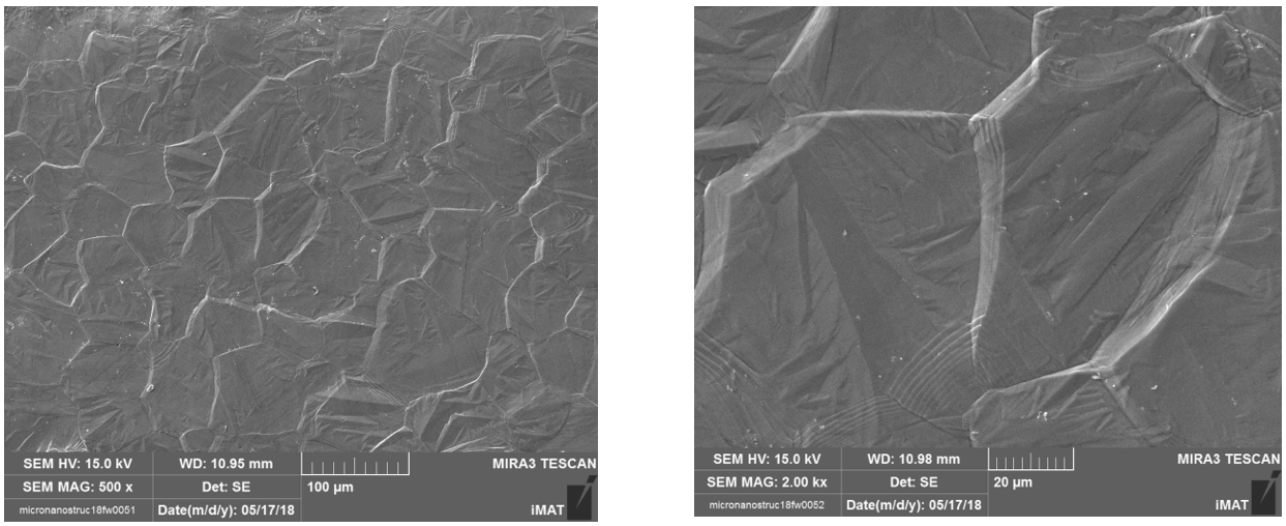


***Fig.6.20*** *Tigr2 EB10µm 650°C 2hs 200K/min Tilt 20°.*

The surface presents α grains with martensitic microstructure (Fig.6.20). The heat treatment was carried out to stabilize the formed martensite.

In all the FESEM images of Ti15Mo and Tigrade2 after heat treatments, is not possible to see the 10µm sized grooves (Figs.6.17-6.20).

## ETCHING TREATMENTS RESULTS

The etching treatment was performed on the following samples:

- EB structured Ti6Al4V samples
- Ti6Al4V EB+HT 1030°C_100K/min
- Ti6Al4V EB+HT 1030°C_200K/min
- Ti6Al4V EB+HT 720°C_200K/min

The etching was tested by varying the concentration of HF and the time of immersion of the sample in acid solution.

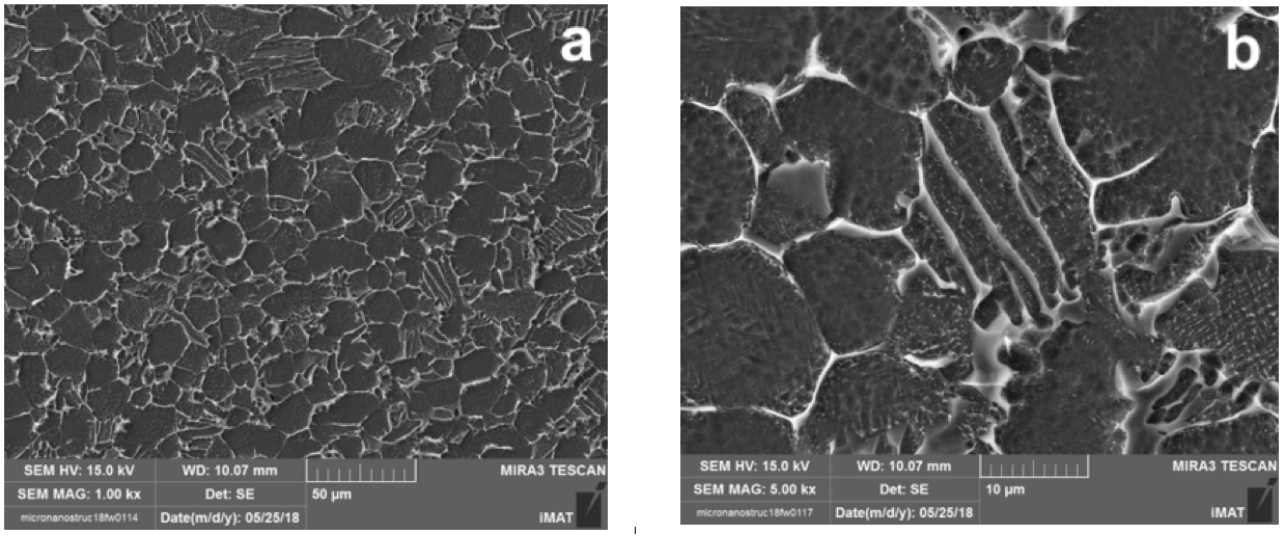


***Fig.6.21*** *Ti64 EB10µm etched HF 1% 4minutes - base material (a mag.1000x; b mag.5000x).*

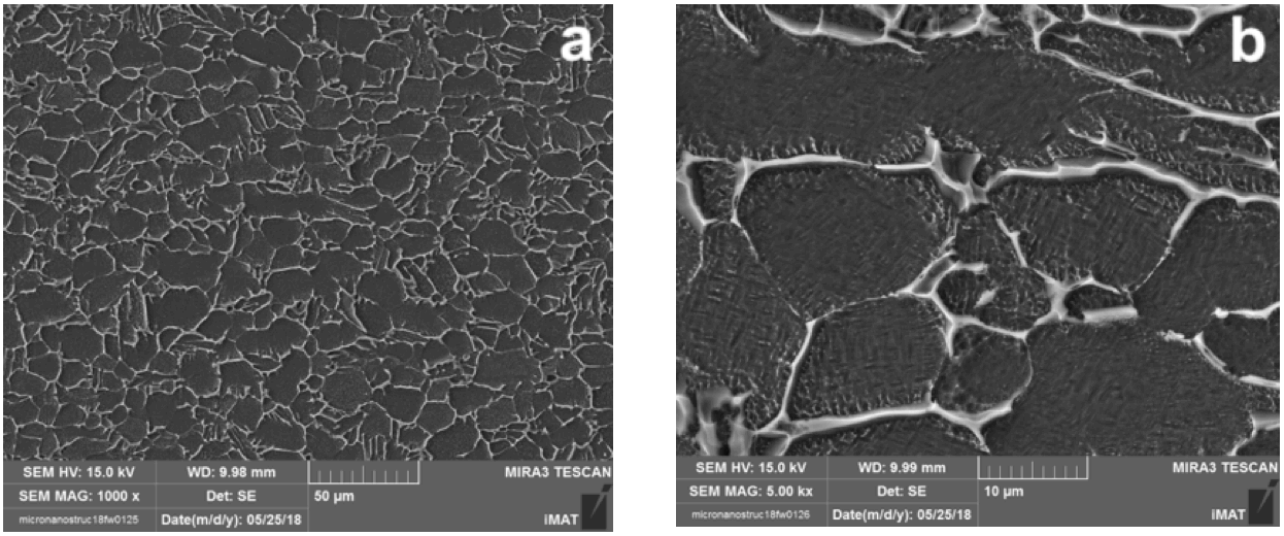


***Fig.6.22*** *Ti64 EB10µm etched HF 1% 2minutes - base material (a mag.1000x; b mag.5000x).*

Fig.6.21 and 6.22 show the effect of the treatment on the surface of the untreated material (base material), using 1% of HF for 4 and 2 minutes respectively. The microstructure is well defined and it is possible to observe the prior beta grains and alfa lamellae.

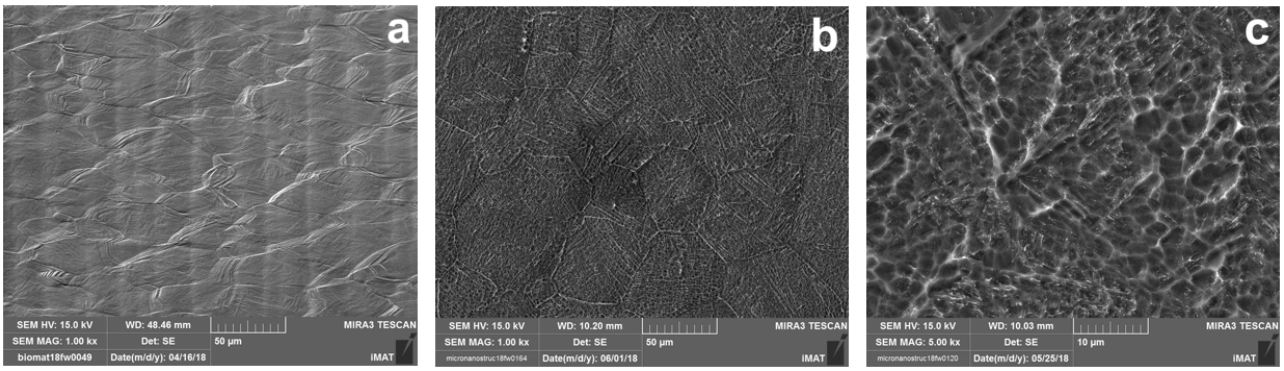


***Fig.6.23*** *Ti64 EB10µm without etching (a); Ti64 EB10µm etched HF 1% 4minutes – structured area (b mag.1000x; c mag.5000x).*

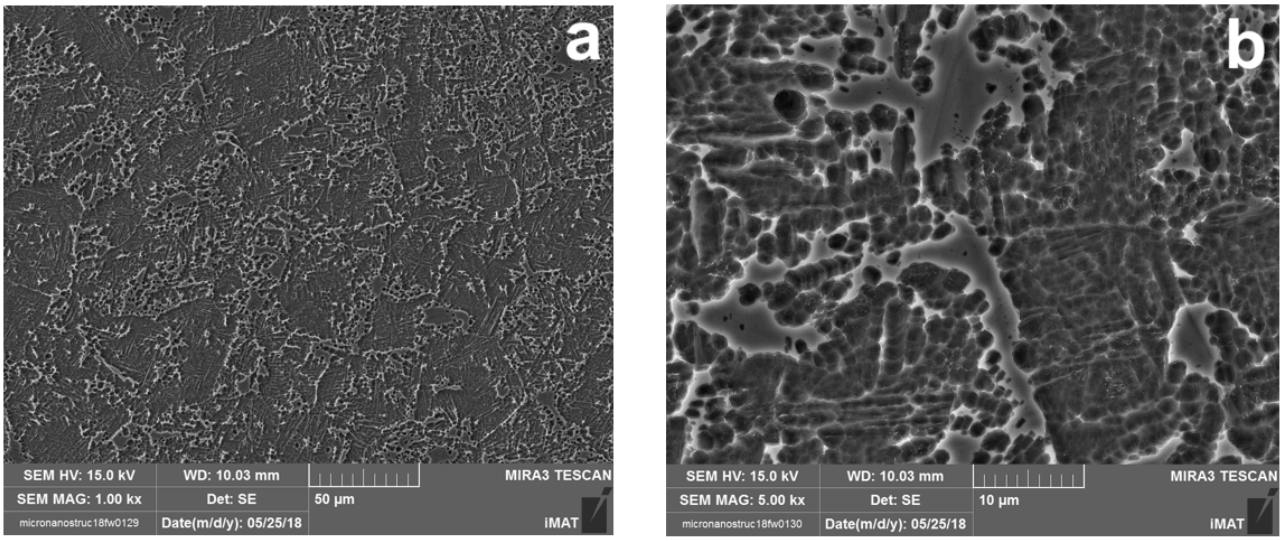


***Fig.6.24*** *Ti64 EB10µm etched HF 1% 2minutes – structured area (a mag.1000x; b mag.5000x).*

Fig.6.23 and 6.24 show the effect of etching on the structured area (the area structured by e-beam) of the same samples of Fig.6.21 and Fig.6.22, using 1% of HF for 4 and 2 minutes, respectively. The treatment in the first case is too aggressive, the surface is too excavated and it is not possible to observe the real microstructure, while in the second case the surface microstructure was not completely removed. The etching treatment is more reactive in the structured area compared to the untreated area of the surface and this may be due to the presence of residual stresses in the structured area after the e-beam treatment.

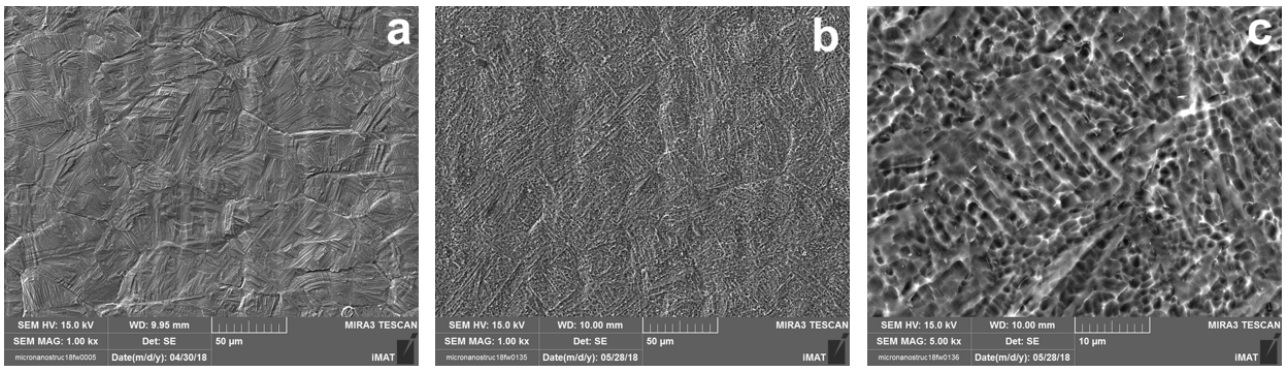


***Fig.6.25*** *Ti64 EB10µm HT1030°C_100K/min* ***without etching (a);*** *Ti64 EB10µm HT1030°C_100K/min first etch HF 1% 4minutes – structured area (b mag.1000x; c mag.5000x).*

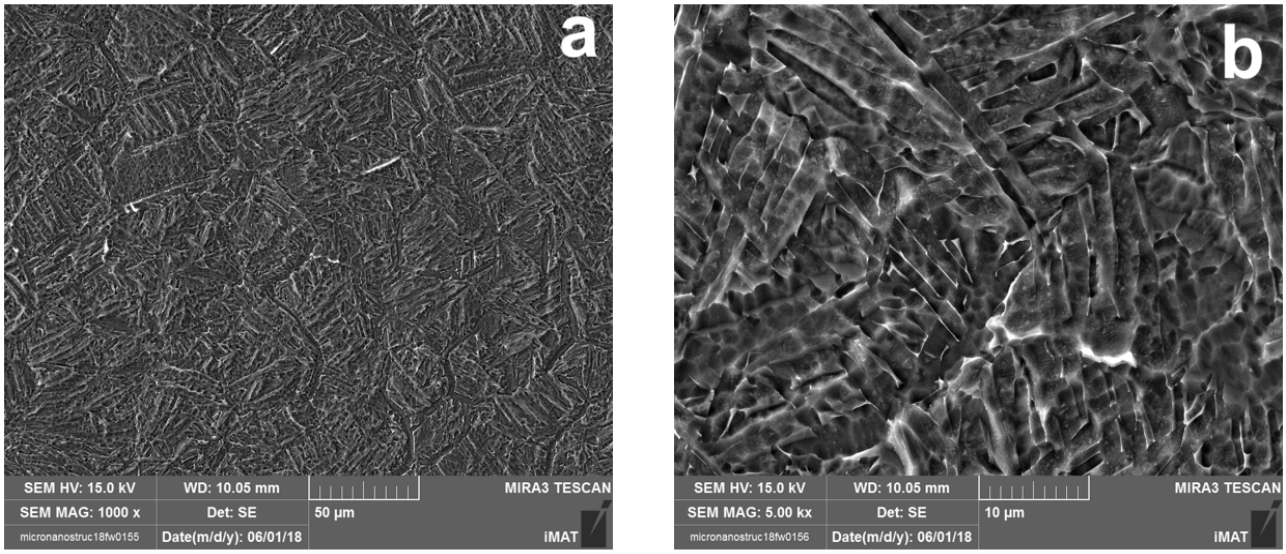


***Fig.6.26*** *Ti64 EB30µm HT1030°C_100K/min second etch HF 1% 4minutes – structured area (a mag.1000x; b mag.5000x).*

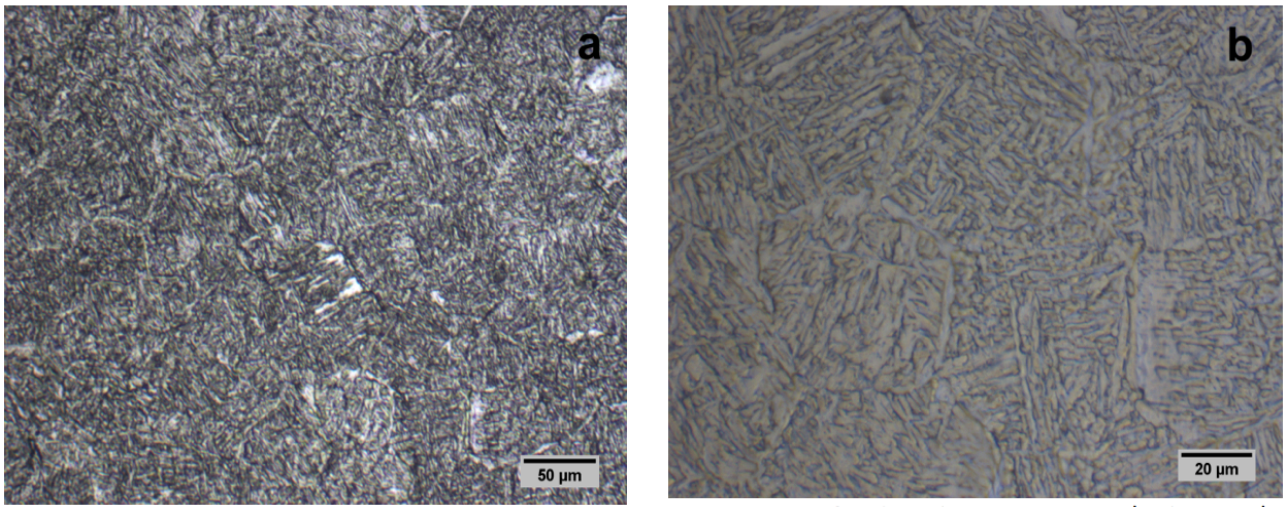


***Fig.6.27*** *Ti64 EB10µm HT1030°C_100K/min second etch HF 1% 4minutes – structured area: microstructure and micro topography (LOM): 200x mag. (a); 500x mag. (b).*

The sample (Fig.6.27) has a dug surface produced by the action of HF acid during etching. The surface was dug where previously α lamellae were present.

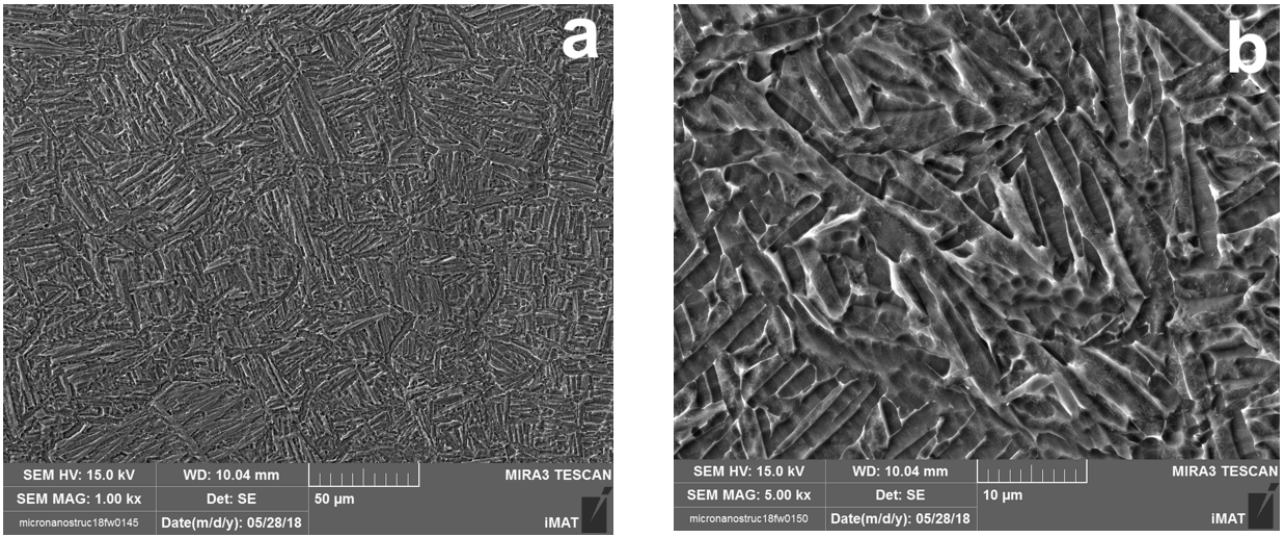


***Fig.6.28*** *Ti64 EB30µm HT1030°C_200K/min second etch HF 1% 4minutes – structured area (a mag.1000x; b mag.5000x).*

The same etching parameters (HF 1%; 4minutes) were also used for the heat treated sample (HT1030°C_100K/min) (Fig.6.25, 6.26, 6.27). "First etch" means that the sample was immersed in the newly formed HF solution while "second etch" means that the sample was immersed in the solution after a first test sample was immersed for 4 minutes. The second one show a less damaged surface in which the alfa lamellae packets can be observed.

Same result can be observed for the heat treated sample HT1030°C_200K/min (Fig.6.28).

The parameters for obtaining an effective etching are found to be therefore:

- 1%HF
- 4 minutes (second etch).

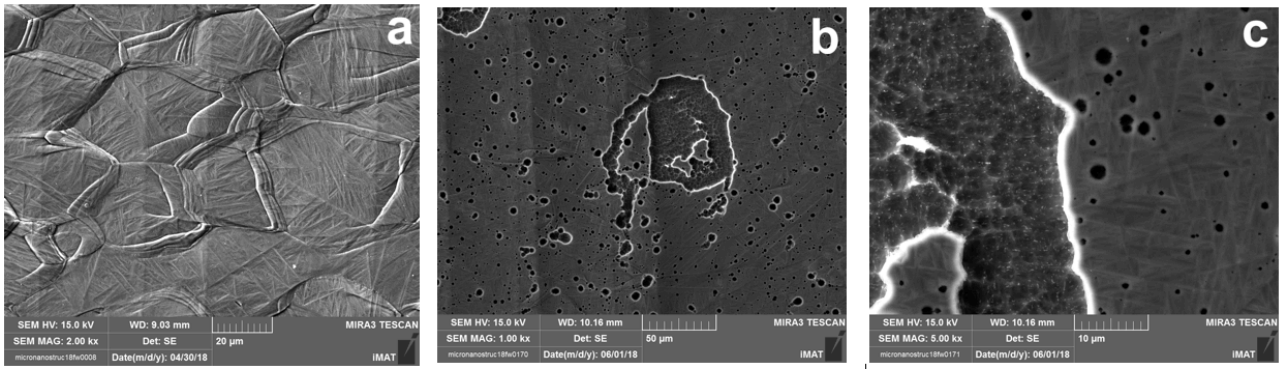


***Fig.6.29*** *Ti64 EB30µm HT 720°C_200K/min without etching (a); Ti64 EB30µm HT 720°C_200K/min second etch HF 1% 4minutes – structured area (b mag.1000x; mag.5000x).*

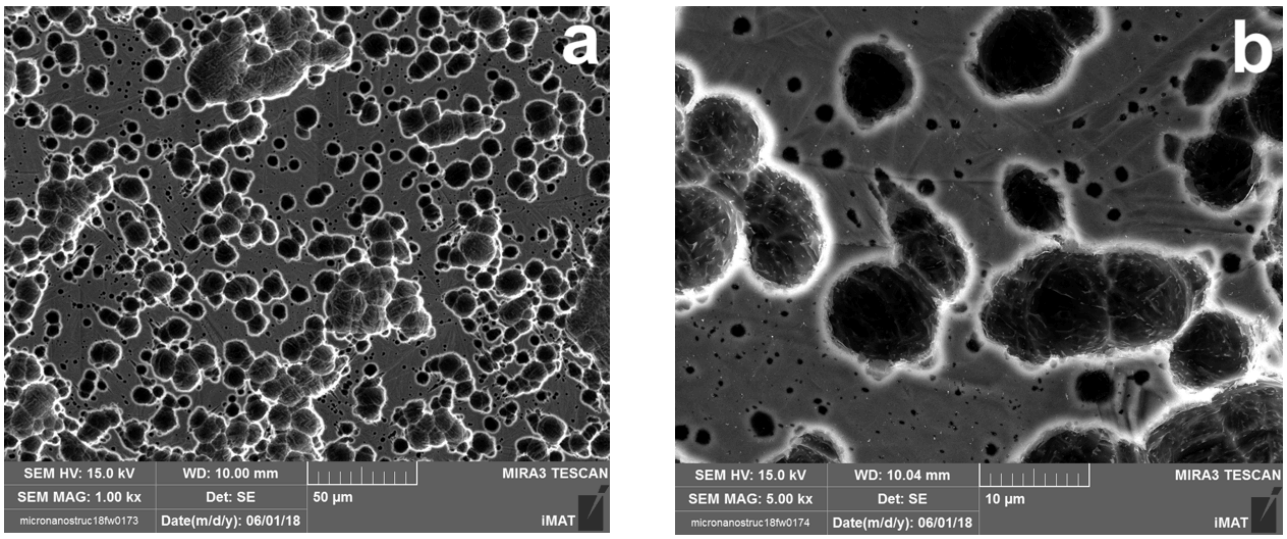


***Fig.6.30*** *Ti64 EB30µm HT 720°C_200K/min second etch HF 1% 8minutes – structured area (a mag.1000x; b mag.5000x).*

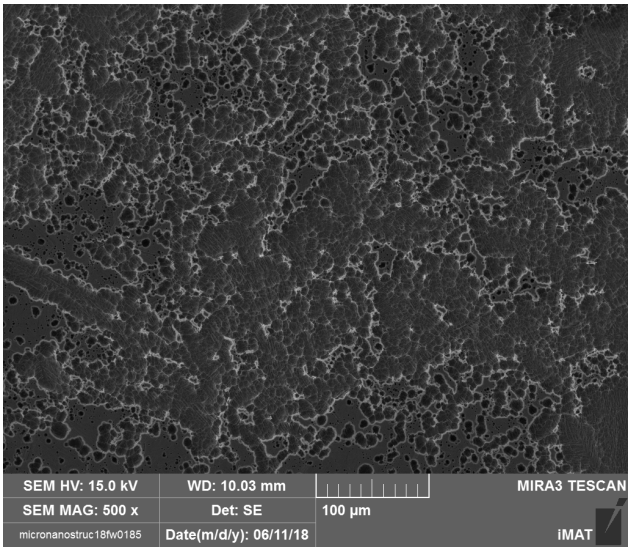


***Fig.6.31*** *Ti64 EB30µm HT 720°C_200K/min first etch HF 3% 3minutes – structured area (a mag.1000x; b mag.5000x).*

However these parameters did not have the same effectiveness in the heat treated sample HT 720°C_200K/min (Fig.6.29). Both the concentration and the etching time has been varied without obtaining a good result (Fig.6.30, Fig.6.31), the surface layer results not completely removed.

## FINAL POLISH

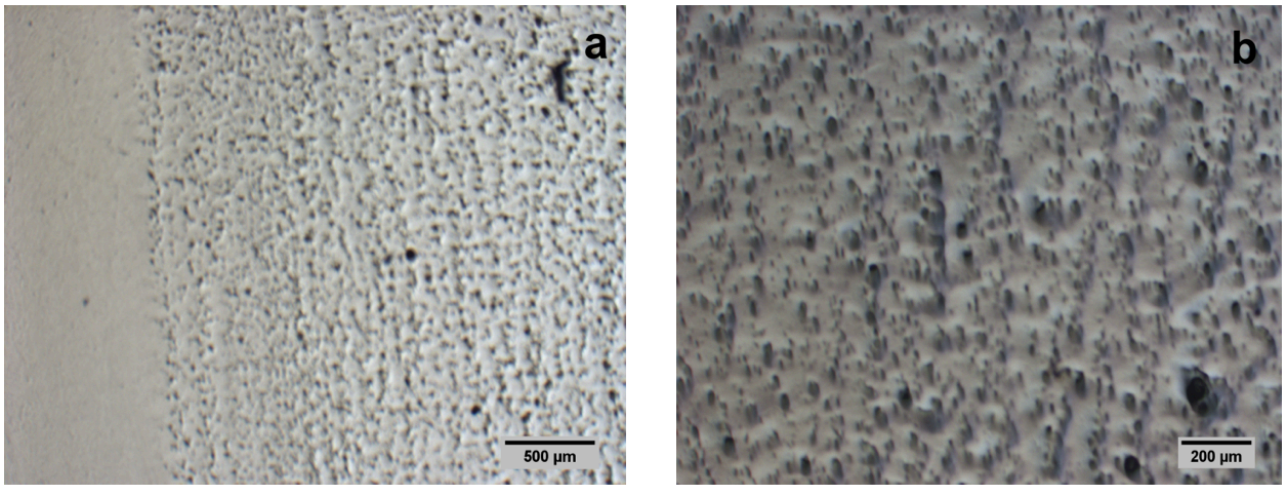


***Fig.6.32*** *P10 microstructure and micro topography (LOM): 20x mag. (a); 50x mag. (b).*

Sample P10 (final polishing on e-beam 10µm structured sample) (Fig.6.32) is characterized by the porous appearance surface due to the final polishing process. In this case it is not possible to identify the microtopography that has been removed to make visible the HAZ surface.
The topography obtained on the P10 sample by final polishing, may be due to two different effects:

- Chemical effect: the suspensions used in the final polishing could corrode the structured area of the surface, that is reactive towards acids (see etching effect in "ETCHING TREATMENTS RESULTS").
- Mechanical effect: from experience, e-beam treatment increase titanium hardness [23]. But in this case, observing the topographic structure, it seems that the opposite effect has been obtained.

## METALLOGRAPHY

Through metallography it is possible to observe the effect of the electron beam technique and the heat treatments on the cross section of the material. The cross section was observed using both FESEM and LOM. To observe the microstructure, the FESEM was used mainly in BSE mode (Back Scattered Electron detector).

From these FESEM and LOM images it is possible to distinguish between a structured (SZ) zone, a heat affected zone (HAZ) and a base material (BM). These zones show different microstructures that depend on the process performed.

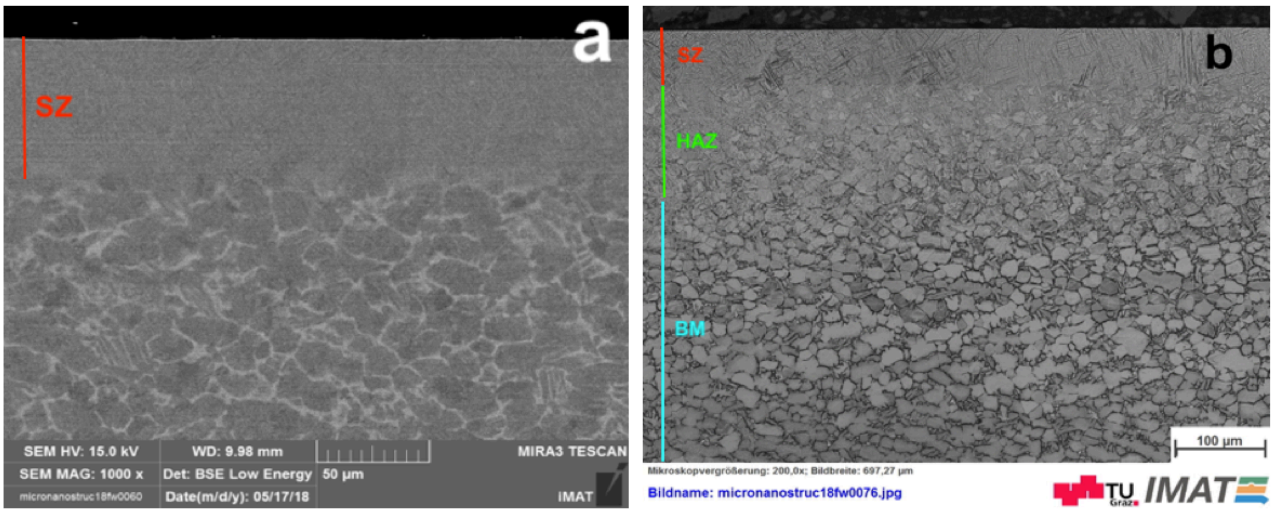


***Fig.6.33*** *Ti64 EB30µm SZ+HAZ+BM (a FESEM image; b LOM image).*

Fig.6.33 shows the cross section of Ti6Al4V after the structuring with 30µm sized grooves. The base material is characterized by primary α grains, and acicular α in β matrix. The heat affected zone presents α primary grains in β matrix, with martensite starting nucleate in grains boundaries. The structuring zone is completed affected by martensite.

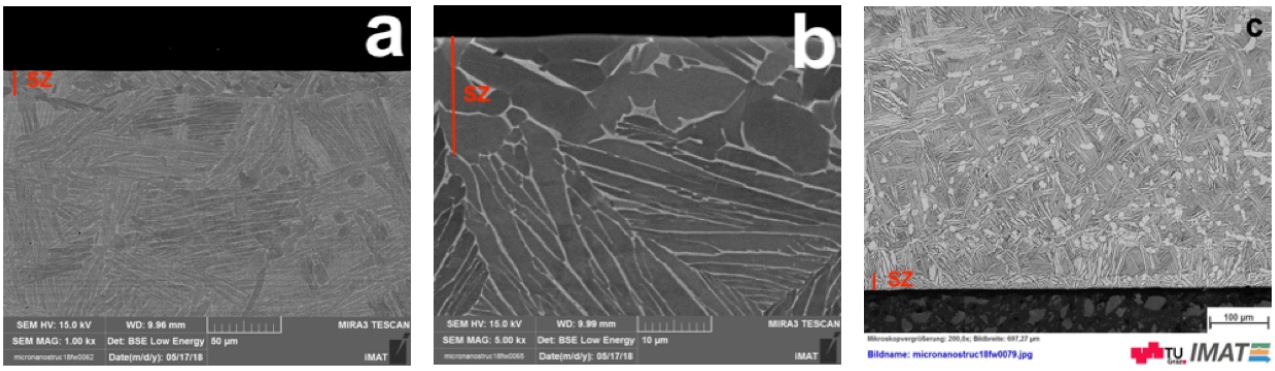


***Fig.6.34*** *Ti64_1030°C (5min)_100K/min EB30µm SZ+HAZ+BM (a FESEM image, c LOM image), SZ+HAZ (b FESEM image).*

In this case the sample underwent a HT with 1030°C heating temperature and 100K/min cooling rate. In Fig.6.34 the base material presents mainly α lamellar microstructure while the SZ has

globular α grains. The presence of some globular α grains in the base material is related to the fact that the exposure time at 1030°C was not long enough to dissolve all the α phase. The structuring zone shows the same microstructure, but with different directions of the lamellar packets and coarser α grains.

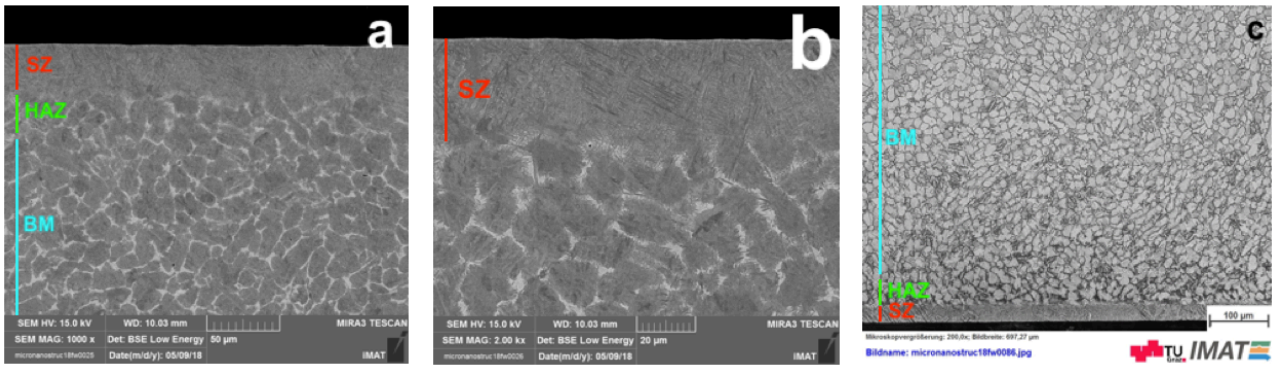


***Fig.6.35*** *Ti64_720°C (2hs)_200K/min EB10µm SZ+HAZ+BM (a FESEM, c LOM image), SZ+HAZ (b FESEM image).*

Fig.6.35 shows the cross section of Ti6Al4V after HT with 720°C heating temperature. The microstructure in the BM, HAZ and SZ is similar to that in Fig.6.27, but the structuring zone has a smaller thickness.

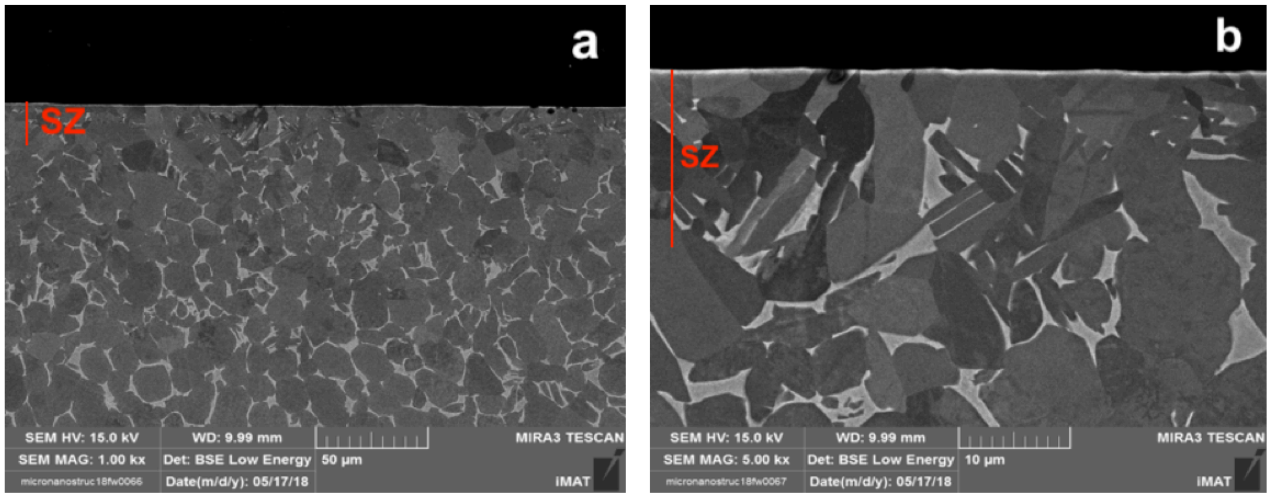


***Fig.6.36*** *Ti64_900°C (4hs)_ 10K/min and 100K/min EB10µm SZ+HAZ+BM (a FESEM image), SZ+HAZ (b FESEM image).*

Fig.6.36 the sample was heat treated with 900°C and 10K/min and 100K/min cooling rate to globularize the microstructure. The morphology of alpha is similar in all the zones. The BM and the HAZ are characterized by an equiaxed microstructure with α grains in β matrix, and some secondary α is present. In the SZ, it is possible to observe also α lamellae (due to the diffusion from martensite shape).

## SURFACE ROUGHNESS

The following table (Tab.6.1) shows the roughness, average and standard deviation measurements for each sample. At least three measurements were made for each sample in the direction perpendicular to the grooves (in the case of structured samples). In the samples in which it was not possible to distinguish well the direction of the groves, the measurements were made both parallel to the long side and to the short side, with a displacement of the machine's stylus of 3.2mm. The roughness was measured in microns.

| Ra [µm] | Short Side | Average | Dev.St. | Long Side | Average | Dev.St. |
|---|---|---|---|---|---|---|
| MP | 0,061 | 0,065 | 0,005 | 0,056 | 0,057 | 0,010 |
| | 0,068 | | | 0,070 | | |
| | | | | 0,055 | | |
| | | | | 0,046 | | |
| EB10 | 0,357 | 0,348 | 0,012 | 0,267 | 0,272 | 0,007 |
| | 0,340 | | | 0,277 | | |
| EB30 | | | | 0,286 | 0,264 | 0,020 |
| | | | | 0,269 | | |
| | | | | 0,237 | | |
| | | | | 0,262 | | |
| HT10 | 0,260 | 0,272 | 0,017 | 0,346 | 0,390 | 0,097 |
| | 0,285 | | | 0,501 | | |
| | | | | 0,323 | | |
| HT10Etch | 0,359 | 0,415 | 0,075 | 0,277 | 0,277 | 0,090 |
| | 0,366 | | | 0,405 | | |
| | 0,521 | | | | | |
| | 0,415 | | | | | |
| P10 | | | | 0,287 | 0,256 | 0,043 |
| | | | | 0,226 | | |

***Tab.6.1*** *Roughness measurements obtained by contact profilometer.*

The roughness increases compared to smooth samples MP and P10, reaching a maximum value in the samples treated with etching (HT10Etch).

In the graph below (figure 6.37) it is possible to observe the roughness, average and deviation values, obtained along the parallel or perpendicular directions to the grooves, for each type of sample, in comparison.

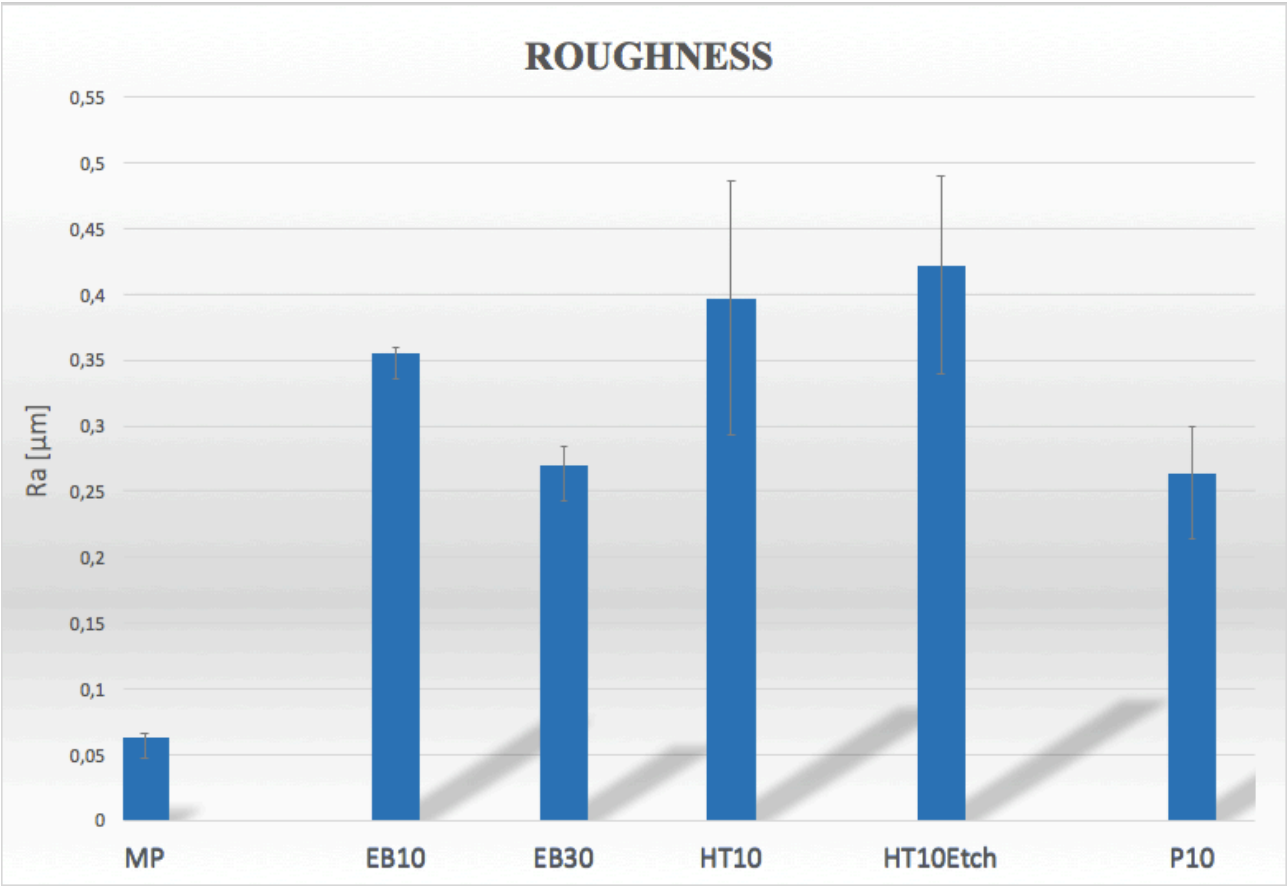


*Fig. 6.37* *Ra [µm] values.*

The following images show the 2D (Figs a) and 3D (Figs b) reconstructions of the sample surfaces.

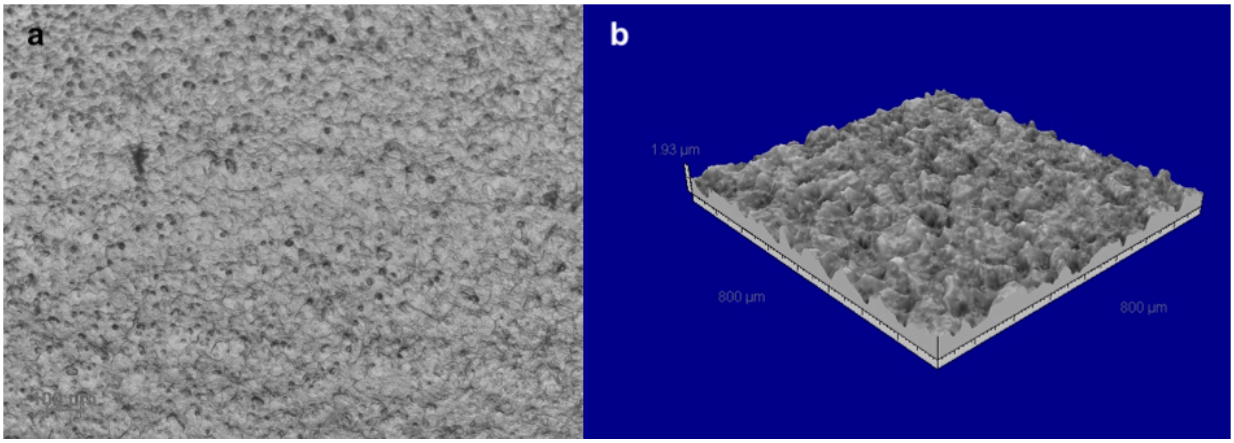


*Fig.6.38* *Ti6Al4V EB10 2D surface (a); 3D surface (b).*

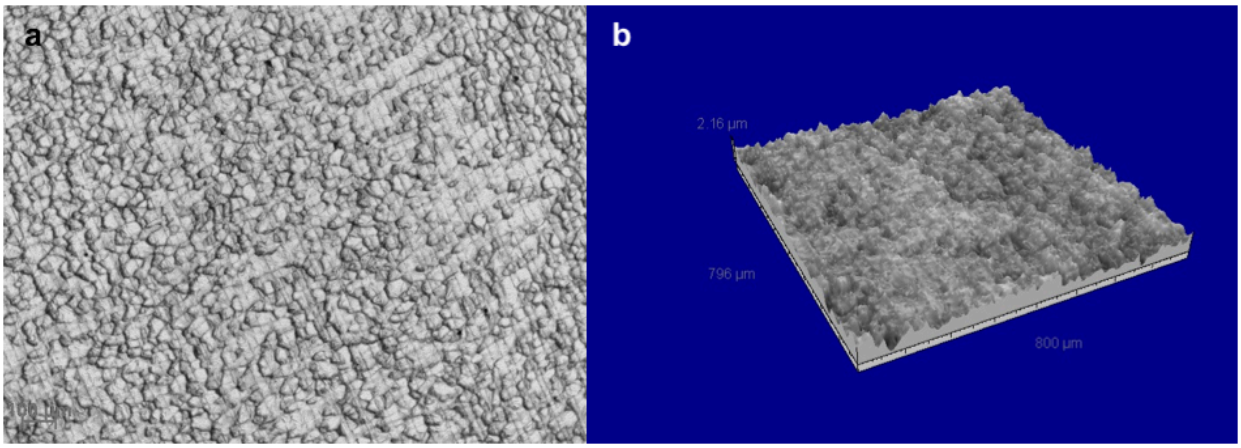


***Fig.6.39*** *Ti6Al4V EB30 2D surface (a); 3D surface (b).*

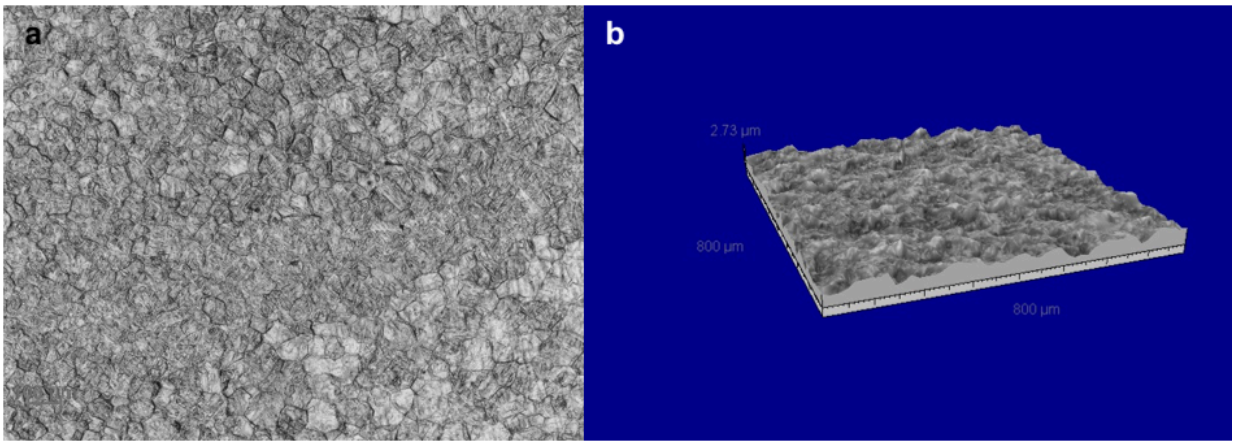


***Fig.6.40*** *Ti6Al4V HT10 (1030°C_100K/min) 2D surface (a); 3D surface (b).*

As already observed in this work, in the sample EB10 (Fig.6.38) the grooves are not visible, but they are visible in EB30 (Fig.6.39), in addiction the first one shows a greater roughness than the second one. However, both are smoother than the heat-treated sample (Fig.6.40) in which a more wrinkled surface can be observed.

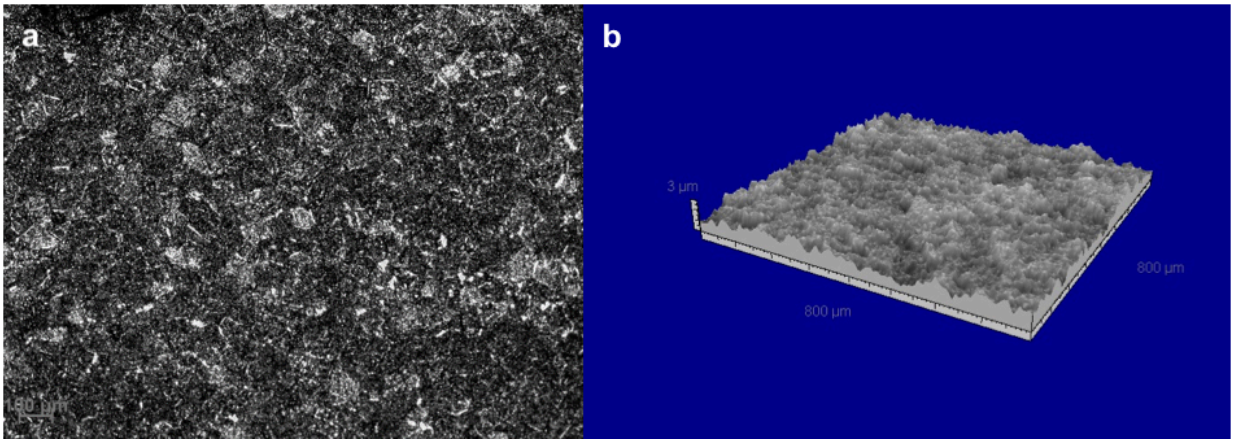


***Fig.6.41*** *Ti6Al4V HT10Etch 2D surface (a); 3D surface (b).*

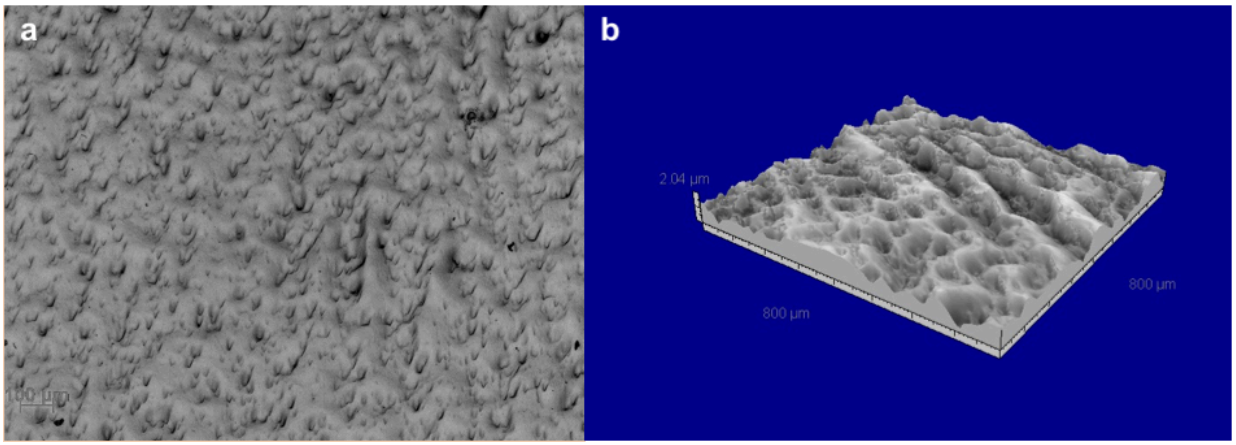


***Fig.6.42*** *Ti6Al4V P10 2D surface (a); 3D surface (b).*

The surface treated with etching (Fig.6.41) is more jagged and carved than the structured surfaces. The surface of P10 sample (Fig.6.42) presents pores and grooves due probably to the final polishing process.

In Fig.6.42 the surface shows a typical comet topography due to the presence of the diamond during the polishing step.

## CONTACT ANGLE

The following table (Tab.6.2) shows the contact angle, average and standard deviation values, and fig.6.43 shows the same results in the form of a histogram.

| | MP | EB10 | EB30 | HT10 | HT10Etch | P10 |
|---|---|---|---|---|---|---|
| | 75,4 | 77,2 | 80,1 | 67,0 | 80,3 | 72,2 |
| | 75,6 | 81,3 | 76,1 | 70,9 | 80,2 | 76,5 |
| | 68,9 | 79,5 | 86,4 | 68,4 | 76,2 | 74,8 |
| | 77,2 | 85,5 | 82,4 | 64,5 | 84,0 | |
| **Average** | 74,275 | 80,875 | 81,250 | 67,700 | 80,175 | 74,500 |
| **Dev.St.** | 3,673 | 3,510 | 4,309 | 2,675 | 3,186 | 2,166 |

***Tab.6.2*** *Contact Angle values [°].*

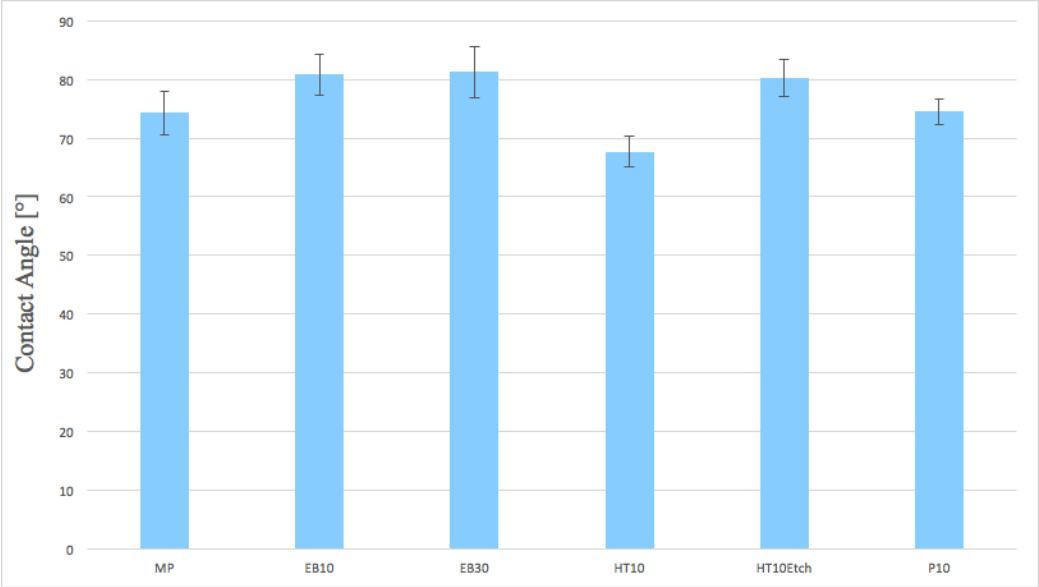


***Fig.6.43*** *Average and Standard Deviation of the Contact Angle measurements.*

All surfaces are slightly hydrophilic, in particular those with a smooth surface MP and P10 (Fig.6.44 a,f) and the HT10 (1030°C_100K/min) Heat treated one (Fig6.44 d); this could be due to a change in the surface microstructure during the heat treatment. The other surfaces show a lower value but are nonetheless hydrophilic.

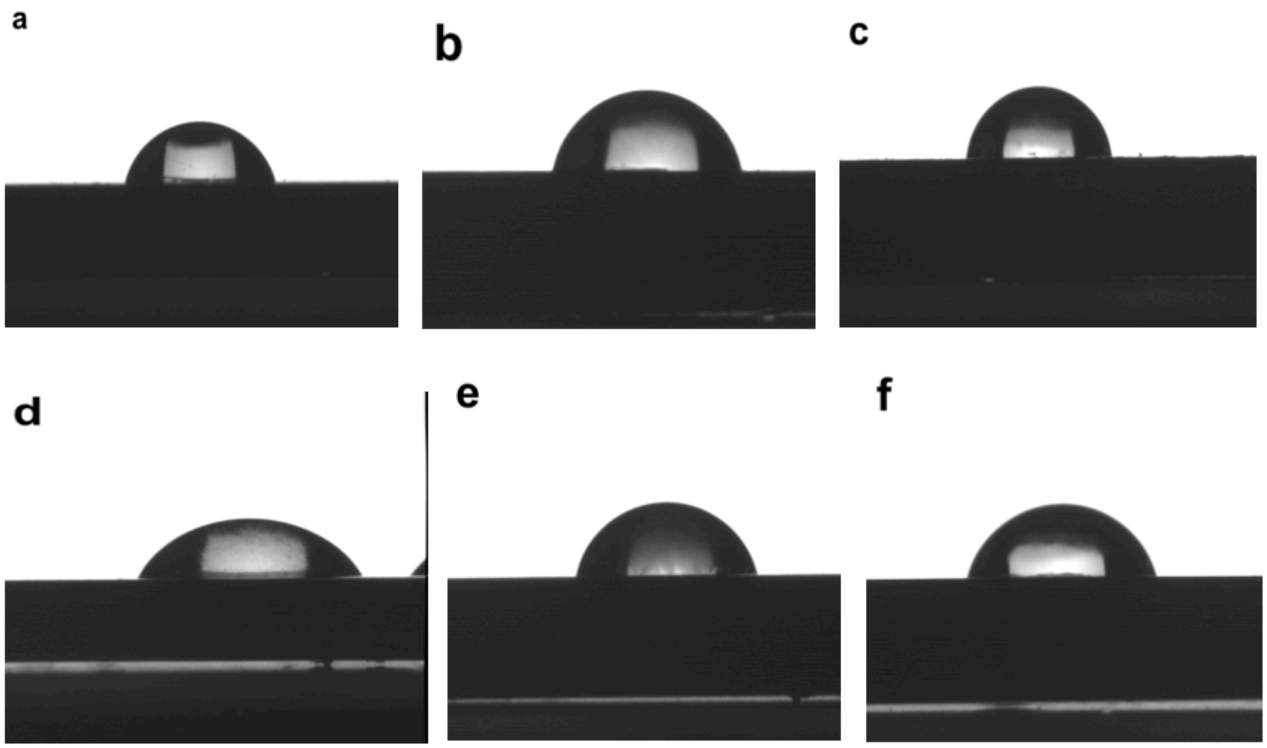


***Fig.6.44*** *Contact Angle drop. a MP; b EB10; c EB30; d HT10; e HT10Etch; f P10.*

## XRD

XRD was used to analyze and to identify the crystalline phases of the samples. The following graphs were obtained from the analysis of the diffraction spectra carried out with the *XPERT High Score* software in which the significant peaks were identified and then exported to an Excel file.
Each graph was normalized against the reference sample's main peak (MP in Fig.6.45 and Fig.6.47; EB10 in Fig.6.46) in order to compare the intensity of the other peaks.

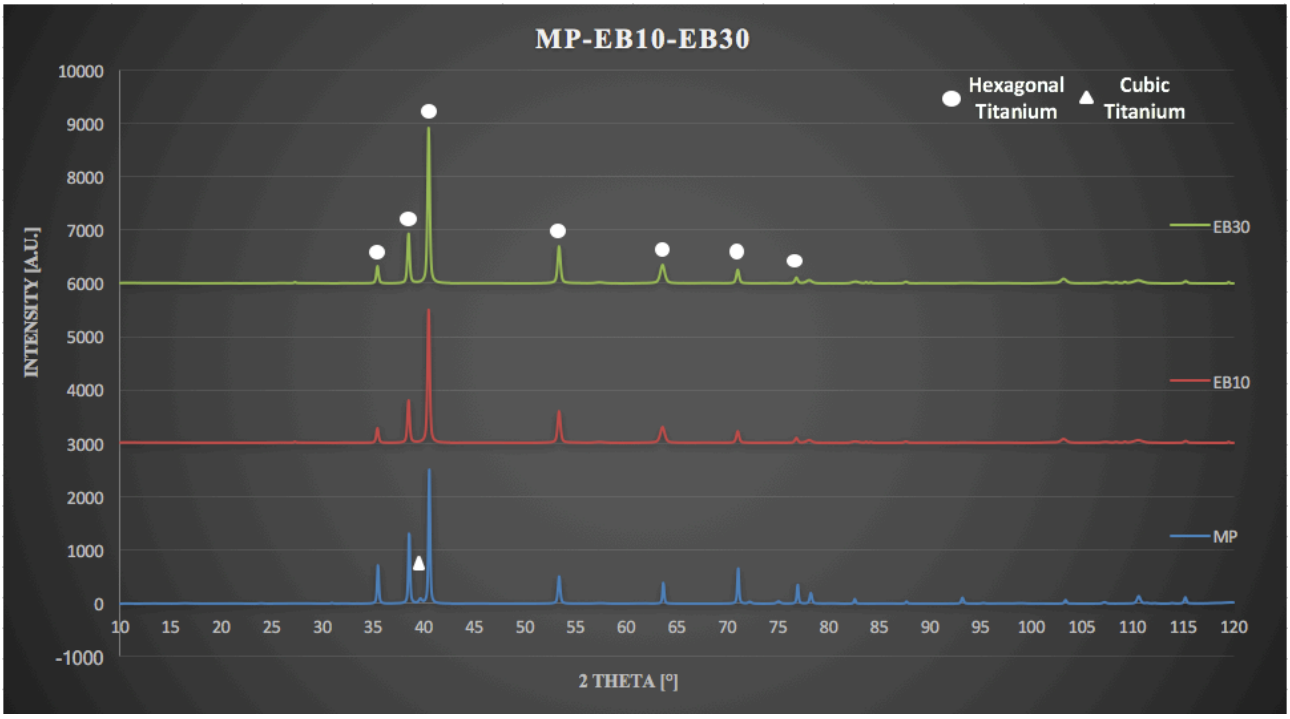


***Fig.6.45a*** *MP, EB10 and EB30 comparison.*

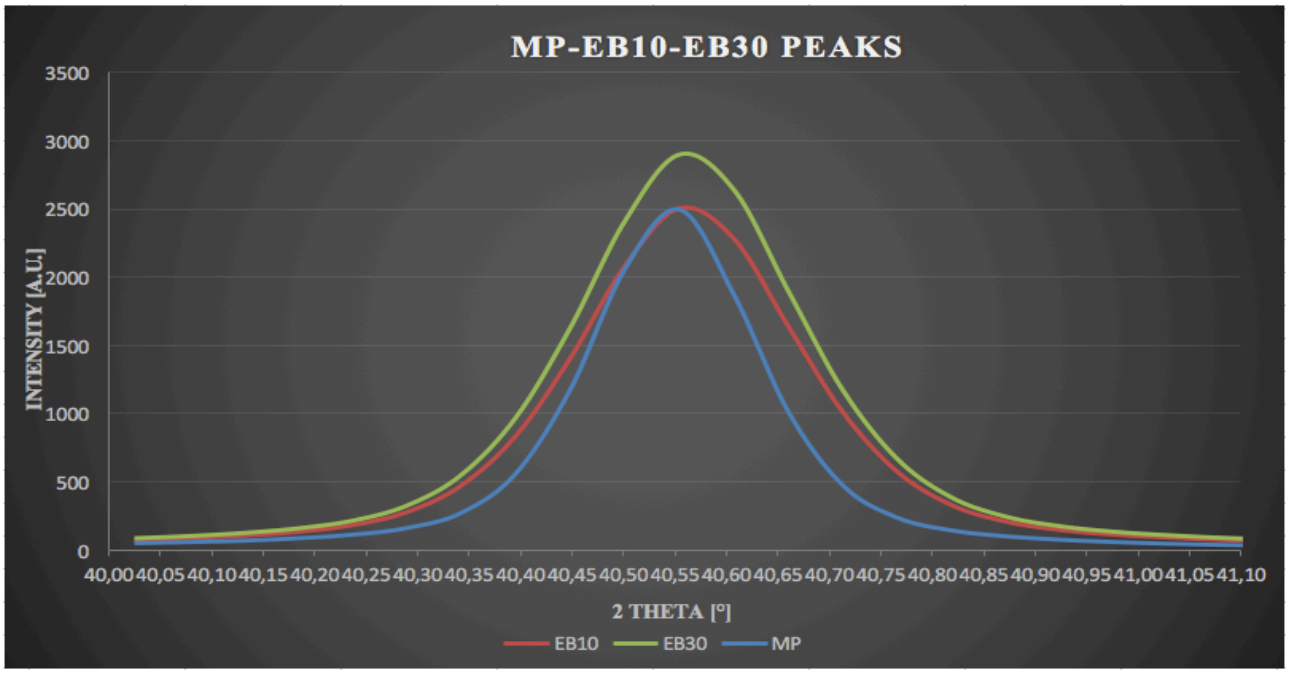


***Fig.6.45b*** *MP, EB10 and EB30 peaks comparison.*

The main peaks of XRD patterns of mirror polished samples are attributable to hexagonal titanium, cubic titanium is visible only in MP spectrum. After EB structuring, the diffraction pattern is close to what obtained before it. A small difference concerns the cubic phase that is no more detected after structuring, which means that the amount of cubic phase is decreased after EB structuring or has a different crystallographic orientation compared to mirror polishing.

A shift of the main peak to higher angles (from 40,55° to 40,56°) can be observed after electron beam structuring (EB10 and EB30) compared to the mirror polished ones (MP), it can be attributed to martensite presence, as previously observed by means of FESEM and optical microscope observations. The peaks of EB10 and EB30, after the e-beam treatment, are wider because the martensite forms smaller grains than those present in the unstructured MP sample.

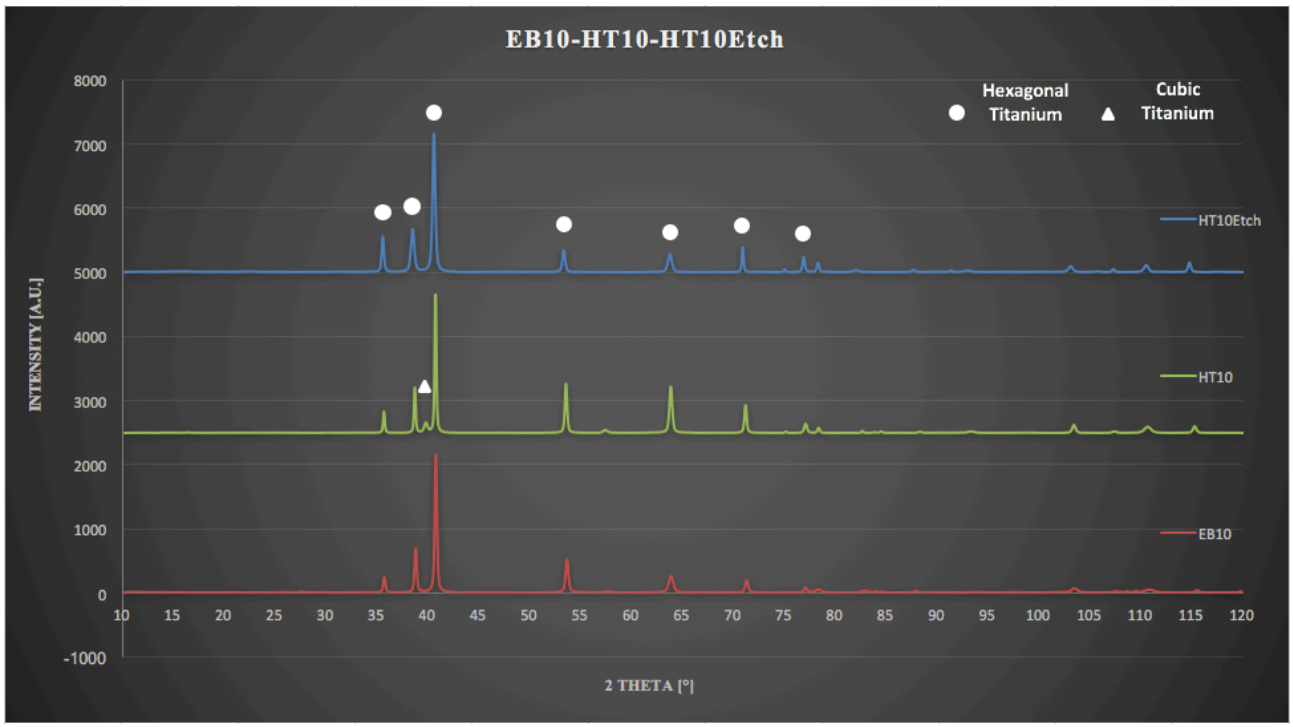


***Fig.6.46a*** *EB10, HT10 and HT10Etch comparison.*

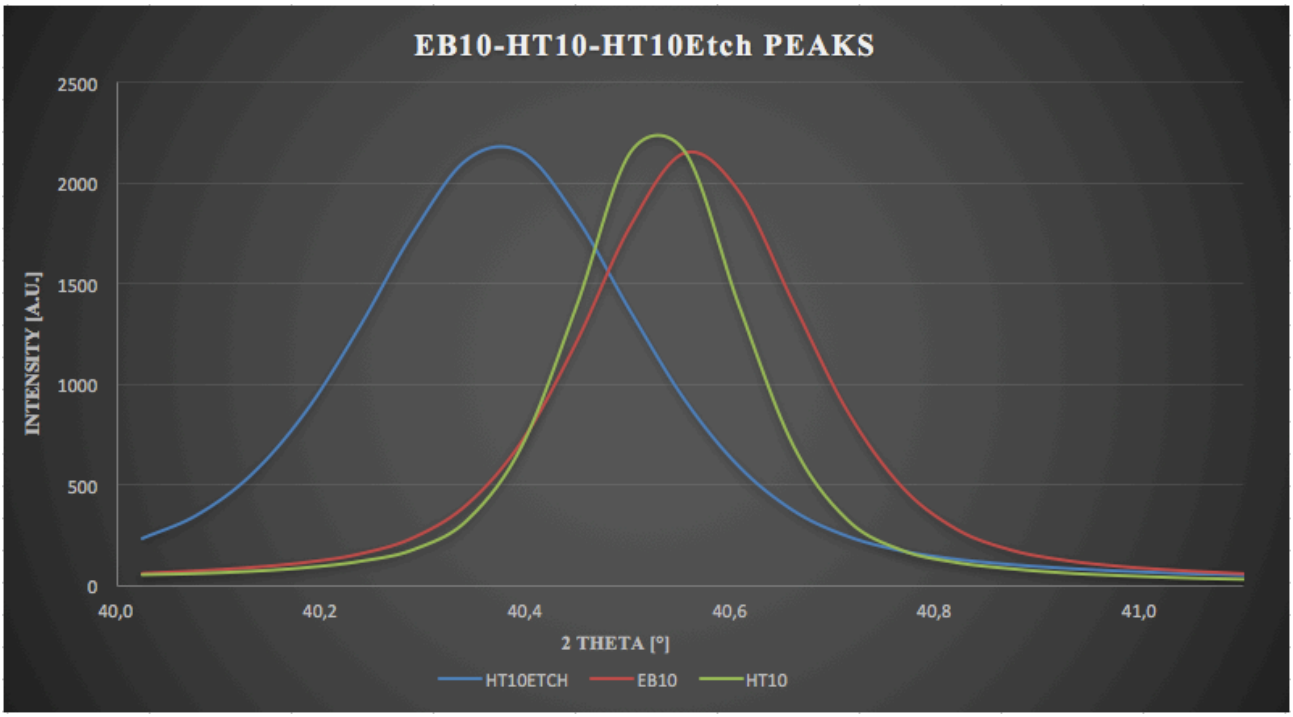


***Fig.6.46b*** *EB10, HT10 and HT10Etch peaks comparison.*

The slight peak shift registered on the main diffraction peak is recovered after thermal treatment (HT10 samples Fig.6.46b) according to martensite removal after heating. A further shift to lower angles values can be detected after etching (HT10 etch sample, Fig.6.46b) and can be attributed to the change in the focal plane due to acid selective removal of alpha phase from the surface.

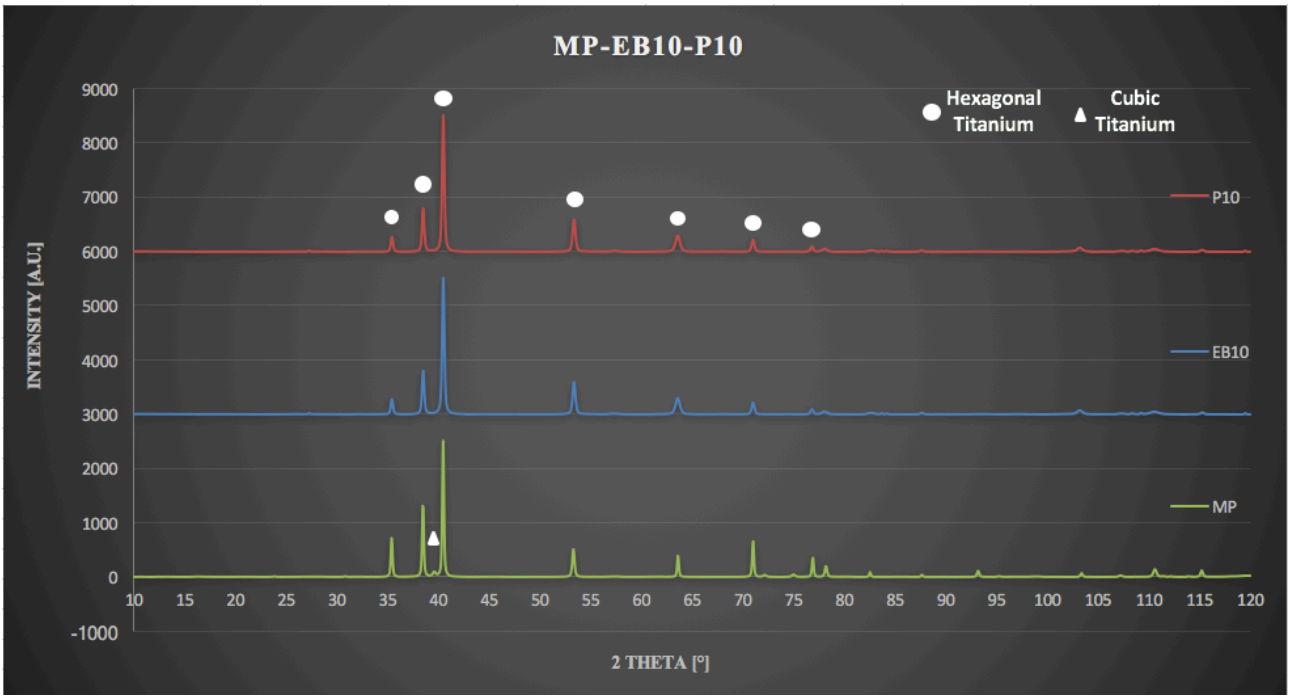


***Fig.6.47a*** *MP, EB10 and P10 comparison.*

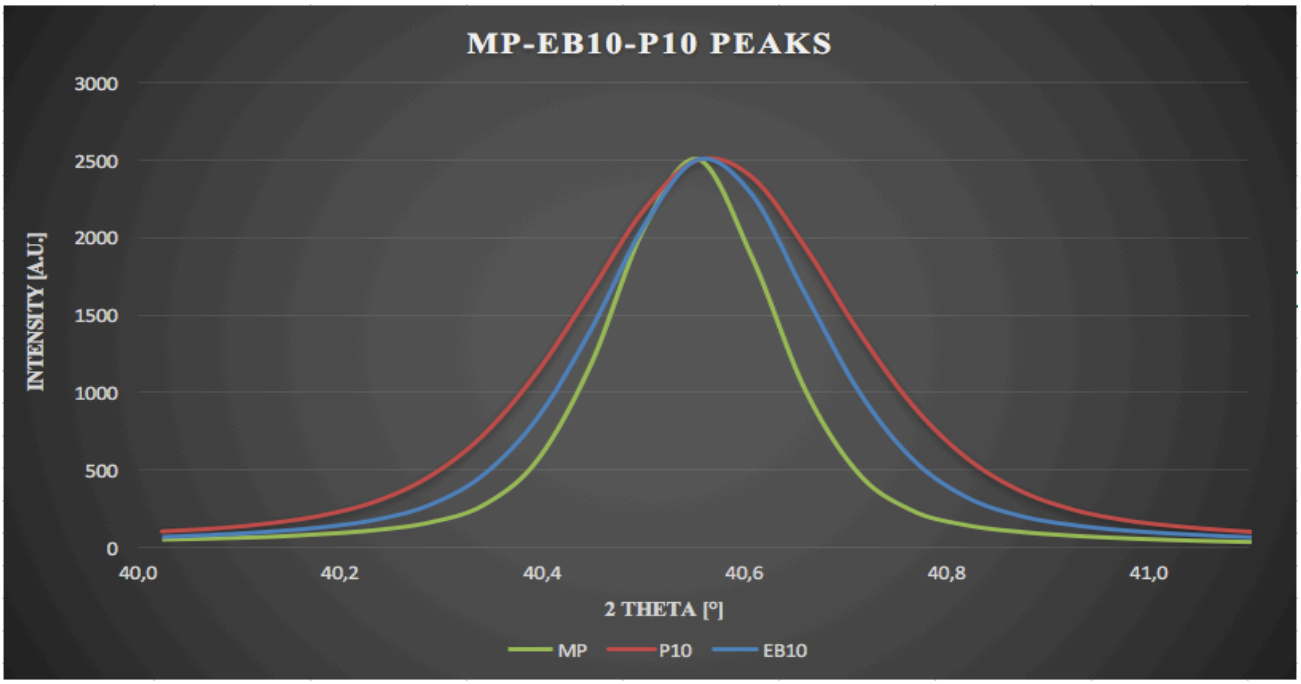


***Fig.6.47b*** *MP, EB10 and P10 peaks comparison.*

In Fig.6.47b, the samples EB10 and P10 show a slight shift of the main peak to higher angles compared to MP sample. Moreover, the peaks are wider than the MP one due to the presence of martensite on the surfaces of EB10 and P10 samples: the polishing removes (as expected) the grooves, but it leaves unchanged the crystalline structure of the SZ zone.

In Fig.6.46a, the spectrum of HT10 sample shows a small peak of beta phase, close to the main peak, a little bit more intense than the observed in spectrum of MP sample in Fig.6.47a.

The peak width of the P10 sample is probably due to an artifact linked to the roughness of the surface.

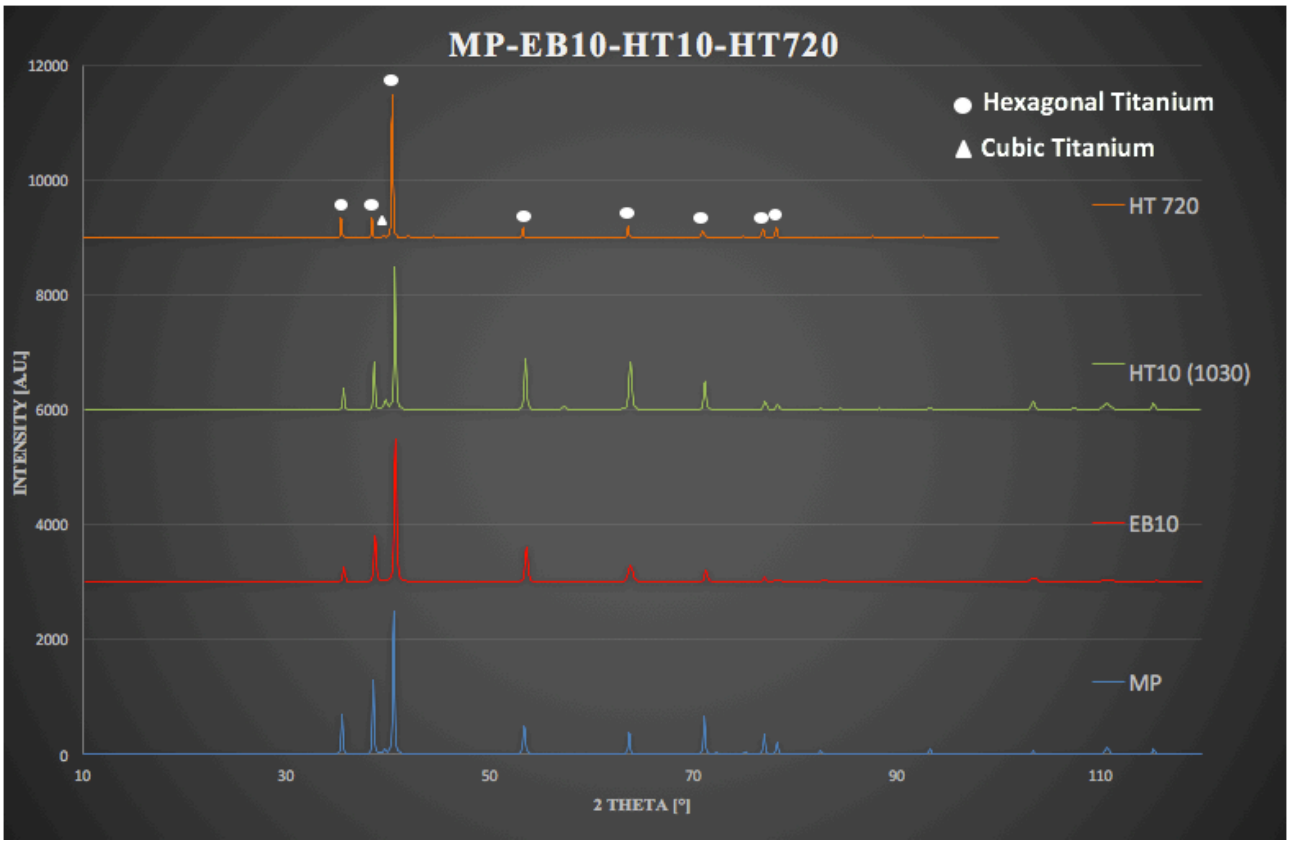


*Fig.6.48 MP, EB10, HT10, HT720 comparison.*

The figure 6.48a shows the main peak of the heat treated sample at 720°C. Also in this case as in the heat treated one at 1030°C, the spectrum shows a small peak of beta phase (cubic titanium) close to the main peak. The HT720 peak is slightly shifted towards lower values, but this is probably due to an instrumental measurement error.

The following table (Tab 6.3) shows all the treatments carried out in the samples of Ti6Al4V, Ti15Mo and Ti grade 2; while in the table 6.4 are reported the observations obtained through XRD.

| | E-BEAM STRUCTURING | | HT | | ETCHING | FINAL POLISHING |
|---|---|---|---|---|---|---|
| | Grooves Dimension | Surface Microstructure | HT parameters (heating rate-heat temperature-cooling rate) | Surface Microstructure | Parameters | |
| Ti6Al4V | 5 µm | Martensite in α grains | | | | |
| | 10 µm | | | | 1%HF; 4min | |
| | | | | | 1%HF; 2min | |
| | | | 300K/min_900°C (4hs)_10K/min_100K/min | α lamellae colonies into prior β grain | 1%HF; 4min (2nd etching) | |
| | | | 300K/min_1030°C (5min)_100K/min | α lamellae colonies into prior β grain | 1%HF; 4min (1st etching) | |
| | | | | | 1%HF; 4min (2nd etching) | |
| | | | | | | P10 |
| | 30 µm | | 300K/min_1030°C (5min)_200K/min | α lamellae colonies into β prior grain | 1%HF; 4min (2nd etching) | |
| | | | 300K/min_720°C (2hs)_200K/min | Martensite in α grains | 1%HF; 4min (2nd etching) | |
| | | | | | 1%HF; 8min (2nd etching) | |
| | | | | | 3%HF; 3min (1st etching) | |
| | | | | | | P30 |
| Ti15Mo | 5 µm | β phase | | | | |
| | 10 µm | | 300K/min_650°C (4hs)_200K/min | β grains | | |
| | | | 5K/min_650°C (4hs)_200K/min | | | |
| Ti grade2 | 10 µm | Martensite in α grains | 300K/min_950°C 5min 200K/min | Martensite in α grains | | |
| | | | 300K/min_650°C/550°C (2hs)_200K/min | | | |
| | 30 µm | | | | | |

***Tab.6.3*** *Treatments carried out in Ti6Al4V, Ti15Mo and Ti grade 2 samples.*

| | XRD | | | |
|---|---|---|---|---|
| | SAMPLE NAME | MICROSTRUCTURE COMPARED TO MP | α PHASE | β PHASE |
| Ti6Al4V | MP | | present | present |
| | EB10 | martensite | present | absent |
| | EB30 | | | |
| | HT10 (1030°C) | α lamellae | | present |
| | HT720 | not analysed through XRD | | |
| | HT10ETCH | not analysed through XRD | | absent |
| | P10 | martensite | | |

***Tab.6.4*** *Treatments carried out in Ti6Al4V, Ti15Mo and Ti grade 2 samples.*

## BIOLOGICAL RESULTS

### DIRECT METABOLIC EVALUATION

The table (Tab.7.1) and the diagram (Fig.7.1) below show the results concerning the cell viability evaluated after two days of culture on the surface of the samples.

| *Human Primary Gingival Fibroblasts Viability (48hs)* | | | | | | |
|---|---|---|---|---|---|---|
| **Sample** | **RFU replicates (@490nm)** | | | **means** | **de.st** | **% vs cnt** |
| **MP (cnt)** | 2040 | 2524 | 2354 | **2306,000** | 245,544 | **100,000** |
| **EB 10** | 2216 | 2262 | 2714 | **2397,333** | 275,204 | **103,961** |
| **EB 30** | 2716 | 2396 | 2564 | **2558,667** | 160,067 | **110,957** |
| **EB 10 HT** | 2624 | 2700 | 2698 | **2674,000** | 43,313 | **115,958** |
| **EB 10 HT ETCH** | 1546 | 1502 | 1308 | **1452,000** | 126,633 | **62,966** |
| **P10** | 2202 | 2582 | 2596 | **2460,000** | 223,544 | **106,678** |

***Tab.7.1*** *Human Primary Gingival Fibroblast Viability values.*

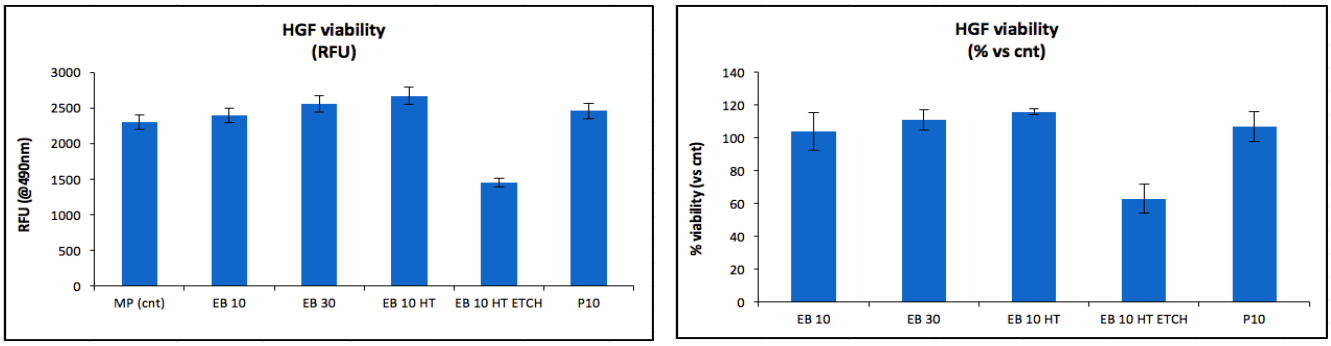


***Fig.7.1*** *HGF viability RFU and % vs cnt.*

The results are reported in the histograms (Fig.71.); in the first one they are referred to the relative fluorescence units (RFU); in the second case, they are normalized with respect to the control sample MP and shown as a percentage of viability.

Except for etched samples (HT10etch) the viability of HGF on the tested samples (EB10, EB30, HT10 and P10) is analogous to the one on control samples (MP) confirming that no cytotoxic effects are introduced by electron beam structuring nor by thermal treatments.

The lack of viability of the cells on the sample HT10Etch may be due to both toxic residues remaining from the etching treatment (although the samples were well washed before seeding the cells), and to the high surface roughness that is therefore not much appreciated by fibroblasts (HGF) that are rugophobic.

Considering one way ANOVA with post-hoc Tukey test, no significant differences can be denoted for HGF adhesion, except for a significant reduction on the etched sample ($p<0.01$)

## BIOFILM METABOLIC EVALUATION

Following are the results of the bacterial viability tests, evaluated one, two and three days after the cell cultivation. The MP sample was taken as the control sample.

Bacterial adhesion to electron beam structured samples (EB10 and EB30) as well as to thermally treated ones (HT10) is close to the one observed on mirror polished controls, evidencing at first that no increase in bacterial attachment is introduced by the grooves (Fig.7.2). Moreover, a significant reduction in bacterial adhesion can be detected on structured samples (EB10-EB30), structured and heat treated samples (EB10HT), as well as on structured heat treated and etched (HT10etch) samples up to 2 days (Fig.7.3-7.4). This phenomenon can be associated to an influence of microstructure and crystalline structure more than topography on bacterial adhesion. This point needs further investigations, but it could be related to a lower adhesion of bacteria on surfaces with a high density of sub-grains.

| ***S. aureus* biofilm Viability Day 1** | | | | | | |
|---|---|---|---|---|---|---|
| **Sample** | **RFU replicates (@490nm)** | | | **means** | **dev.st** | **% vs cnt** |
| **MP (cnt)** | 8893 | 8565 | 10043 | **9167,000** | 776,162 | **100,000** |
| **EB 10** | 7525 | 7089 | 7727 | **7447,000** | 326,074 | **81,237** |
| **EB 30** | 7808 | 7454 | 7878 | **7713,333** | 227,300 | **84,142** |
| **EB 10 HT** | 6289 | 6954 | 5919 | **6387,333** | 524,460 | **69,677** |
| **EB 10 HT ETCH** | 4452 | 5695 | 4156 | **4767,667** | 816,618 | **52,009** |
| **P10** | 3610 | 4691 | 4725 | **4342,000** | 634,158 | **47,366** |
| **P30** | 5071 | 5569 | | **5320,000** | 352,139 | **58,034** |

***Tab.7.2*** *S. aureus biofilm Viability values for Day1.*

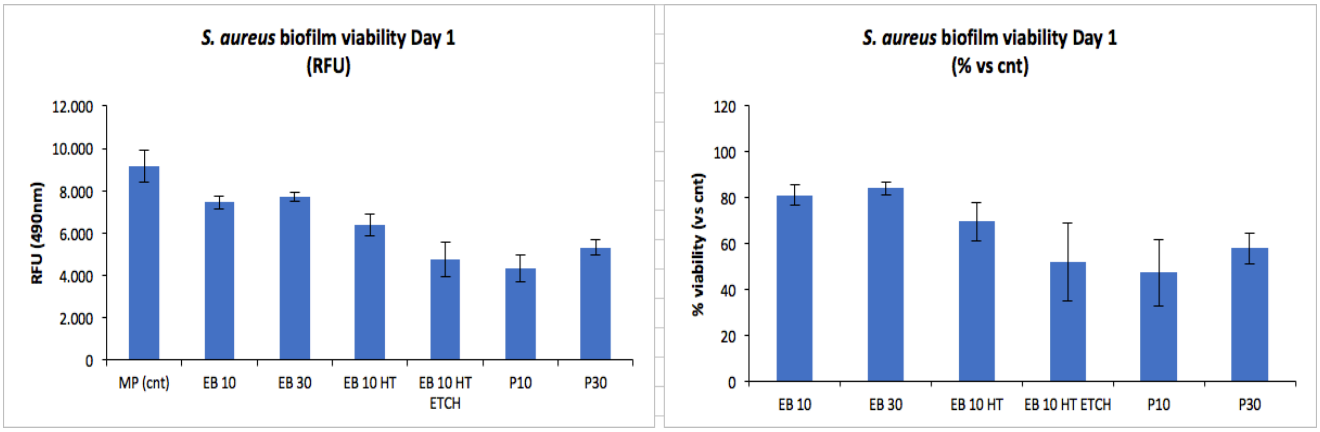


***Fig.7.2*** *S. aureus biofilm viability Day1 RFU and % vs cnt.*

Considering one way ANOVA with post-hoc Tukey test, bacterial adhesion resulted significantly lower on all the treated samples at day 1 ($p<0.05$ for EB10, $p<0.01$ for EB10HT), except for EB30. Moreover, etching and polishing further reduce bacterial adhesion, compared to EB10 samples ($p<0.01$). Analogously polishing enhances the reduction of bacterial adhesion compared to EB30 ($p<0.01$).

| *S. aureus biofilm Viability Day 2* | | | | | | |
|---|---|---|---|---|---|---|
| **Sample** | **RFU replicates (@490nm)** | | | **means** | **dev.st** | **% vs cnt** |
| **MP (cnt)** | 9478 | 9256 | 9508 | **9414,000** | 137,652 | **100,000** |
| **EB 10** | 8594 | 8858 | 9056 | **8836,000** | 231,784 | **93,860** |
| **EB 30** | 8842 | 8202 | 9604 | **8882,667** | 701,884 | **94,356** |
| **EB 10 HT** | 8258 | 8634 | 8724 | **8538,667** | 247,195 | **90,702** |
| **EB 10 HT ETCH** | 6348 | 6534 | 6458 | **6446,667** | 93,516 | **68,480** |
| **P10** | 5858 | 5950 | 5942 | **5916,667** | 50,964 | **62,850** |
| **P30** | 6098 | 6124 | | **6111,000** | 18,385 | **64,914** |

***Tab.7.3*** *S. aureus biofilm Viability values for Day2.*

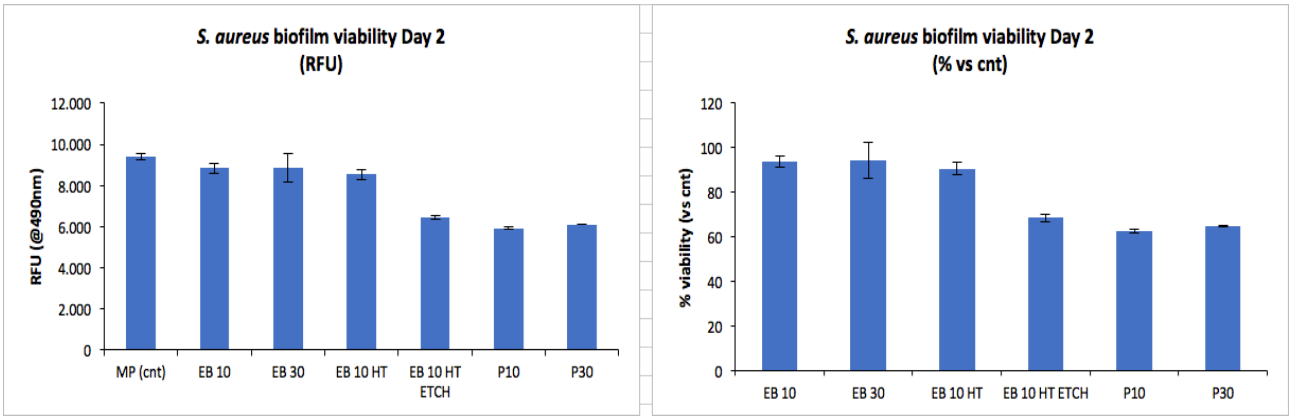


***Fig.7.3*** *S. aureus biofilm viability Day2 RFU and % vs cnt.*

After two days nor EB10 nor EB30 presented a significant reduction of bacterial adhesion compared to the control (MP). A significant reduction persists for the EB10HT sample compared to MP sample ($p<0.05$) but not to EB10 one. Etching and polishing reduced bacterial adhesion compared to EB10 samples ($p<0.01$) and polishing reduced bacterial adhesion compared to EB30 ($p<0.01$).

| *S. aureus biofilm Viability Day 3* | | | | | | |
|---|---|---|---|---|---|---|
| **Sample** | **RFU replicates (@490nm)** | | | **means** | **dev.st** | **% vs cnt** |
| **MP (cnt)** | 10387 | 9390 | 9516 | **9764,333** | 542,913 | **100,000** |
| **EB 10** | 9340 | 9592 | 9103 | **9345,000** | 244,538 | **95,705** |
| **EB 30** | 9253 | 9557 | 9499 | **9436,333** | 161,398 | **96,641** |
| **EB 10 HT** | 8327 | 8439 | 8879 | **8548,333** | 291,790 | **87,547** |
| **EB 10 HT ETCH** | 5269 | 6791 | 6021 | **6027,000** | 761,018 | **61,725** |
| **P10** | 6972 | 5751 | 7901 | **6874,667** | 1078,300 | **70,406** |
| **P30** | 6944 | 7851 | | **7397,500** | 641,346 | **75,760** |

***Tab.7.4*** *S. aureus biofilm Viability values for Day3.*

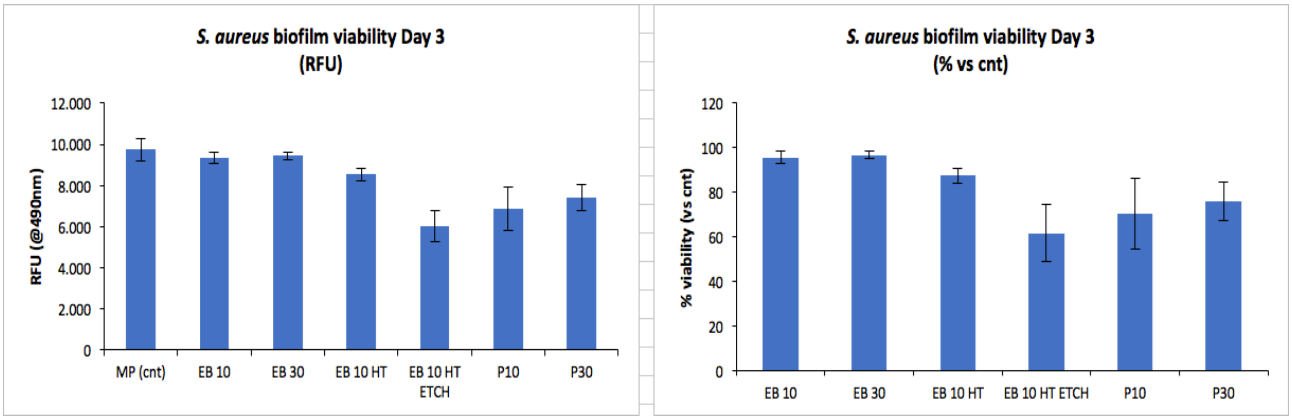


***Fig.7.4*** *S. aureus biofilm viability Day3 RFU and % vs cnt.*

At day 3 no significant differences can be noticed between bacterial adhesion on mirror polished surfaces and EB10, EB30 and EB10HT ones. On the other hand, a significantly lower bacterial adhesion can be evidenced on etched and polished samples compared to EB10 ones ($p<0.01$) and on polished samples compared to EB30 ones ($p<0.05$).

The bacterial concentration on the samples was estimated by counting the number of colonies cultured from serial dilutions of the samples. The results are shown in the following table and histogram and indicated as CFU (units forming colonies). The MP sample is taken as control sample.

| ***S. aureus biofilm viable colonies number (day 3)*** | | | | | |
|---|---|---|---|---|---|
| **Sample** | **CFU count (log10)** | | | **means** | **dev.st** |
| **MP (cnt)** | 3,00E+06 | 1,00E+06 | 9,00E+05 | **1,63E+06** | 1,18E+06 |
| **EB 10** | 3,00E+05 | 9,00E+04 | 7,00E+04 | **1,53E+05** | 1,27E+05 |
| **EB 30** | 4,00E+05 | 3,00E+04 | 5,00E+04 | **1,60E+05** | 2,08E+05 |
| **EB 10 HT** | 9,00E+04 | 7,00E+04 | 2,00E+05 | **1,20E+05** | 7,00E+04 |
| **EB 10 HT ETCH** | 2,00E+04 | 1,00E+04 | 9,00E+03 | **1,30E+04** | 6,08E+03 |
| **P10** | 8,00E+03 | 9,00E+03 | 4,00E+04 | **1,90E+04** | 1,82E+04 |
| **P30** | 5,00E+04 | 2,00E+04 | 1,00E+04 | **2,67E+04** | 2,08E+04 |

***Tab.7.5*** *S. aureus biofilm viable colonies number after Day3.*

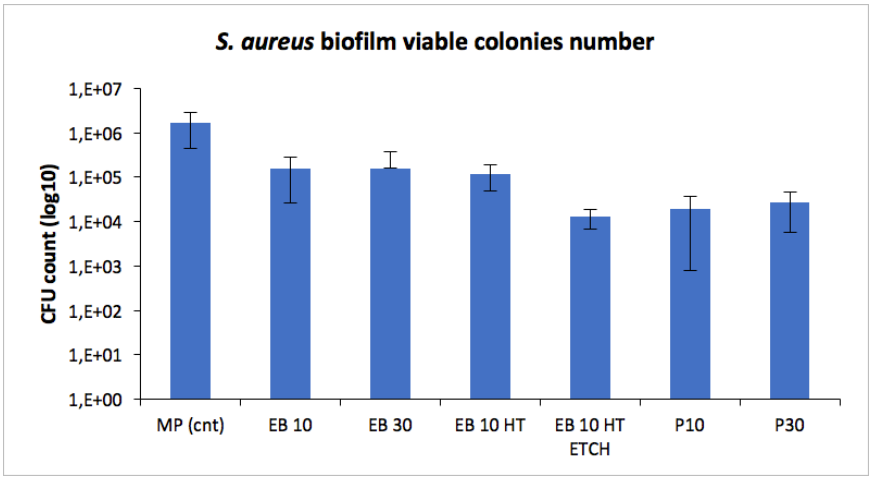


***Fig.7.5*** *S. aureus biofilm viable colonies number.*

The bacterial concentration after three days of culture is higher in the MP control sample. The samples EB10, EB30 and EB10HT show similar values, as well as EB10ETCH, P10 and P30 which show slightly lower values (Fig.7.5).

Considering the CFU count at day 3, the number of bacteria adhered to EB and EB10HT samples resulted significantly lower than that on MP samples ($p<0.05$) but non-further significant reduction can be evidenced after etching (EB10HTETCH) and polishing (P10 and P30).

## MORPHOLOGICAL EVALUATION

After 48h of direct cultivation, morphology of the cells was investigated by immunofluorescence (IF) staining by using a fluorescent microscope.

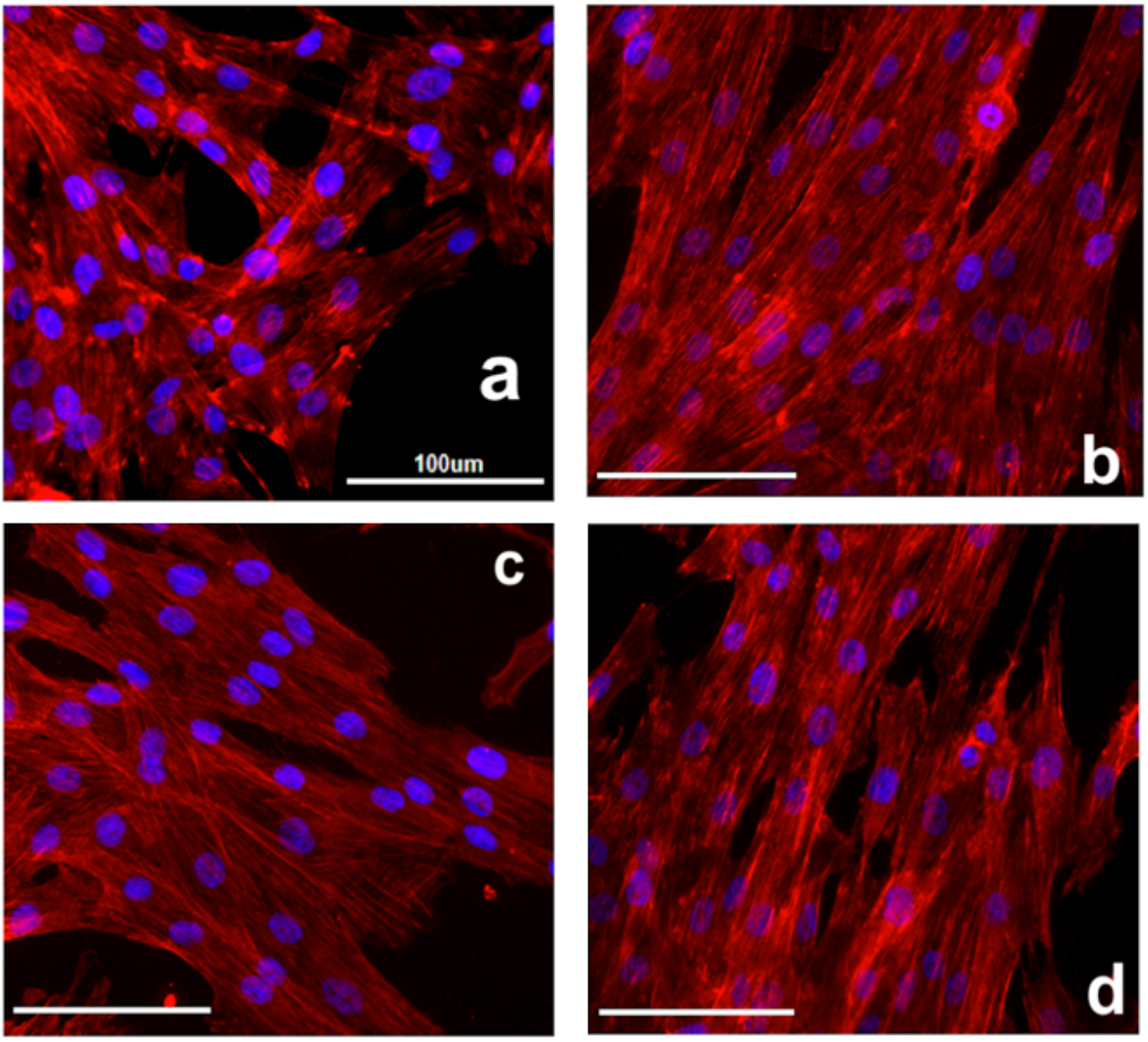


***Fig.7.6*** *Cell morphology in MP sample (a), EB10 sample (b), EB30 sample (c) and EB10HT sample (d).*

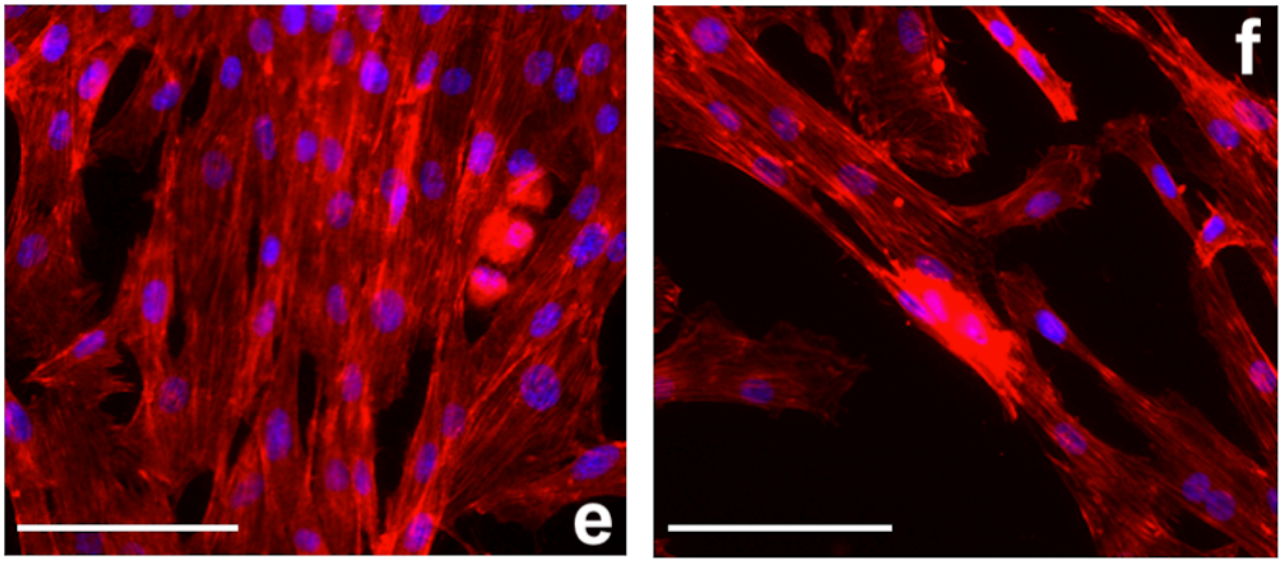


***Fig.7.8*** *Cell morphology in EB10HTETCH sample (e) and P10 sample (f).*

DAPI allows to observe the cell nuclei in blue, whereas the phalloidin makes the cytoskeleton visible in red. The cells show a good superficial spreading in all the samples, and a good alignment along a specific direction in structured samples with grooves (Fig.7.6 b; Fig.7.7 d), even after heat treatment and etching (Fig.7.8 e). In the sample characterized by 30 micron spaced grooves (Fig. 7.7 c), the cells are not as well aligned as in the sample with 10 micron spaced grooves (Fig.7.6 b), because the dimensions of the grooves are greater than the size of the cells which therefore does not feel the effect of the contact guidance.

The cells on the P10 sample (Fig.7.8 f) also appear to be aligned along one direction, because the grooves were not completely removed from the surface through the polishing.
In the MP control sample (Fig.7.6 a), the cells are not aligned as there is no topography to act as a guide.

The FESEM was used to observe the cells and bacteria fixed on the surfaces of the various samples. It was used mainly in InLens mode.

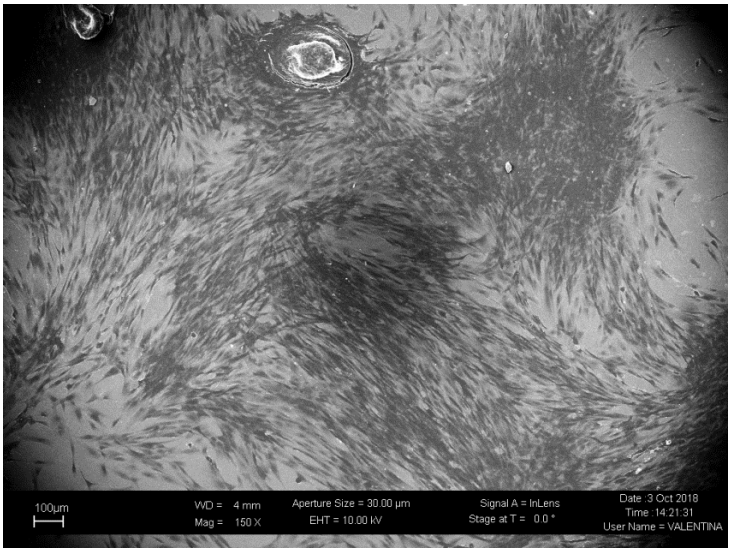


***Fig.7.9*** *MP_HGF*

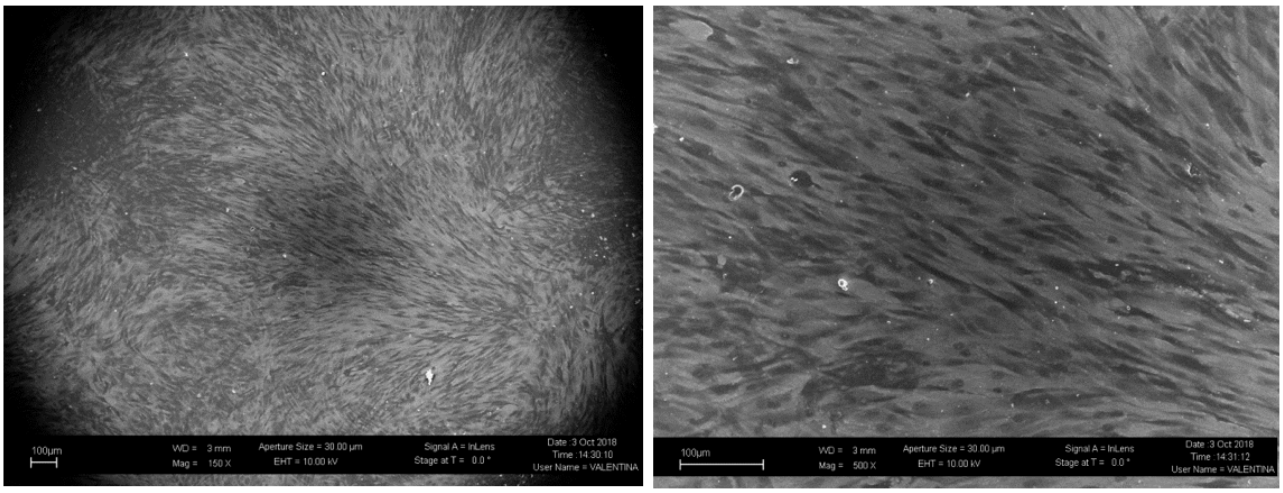


***Fig.7.10*** *EB10_HGF*

On the surface of the MP sample (Fig.7.9), the cells are arranged in circles, without being aligned in a main direction. As already seen in the previous results, this is due to the lack of grooves providing the contact guide effect.

On the contrary, the surface of EB10 sample (Fig.7.10) has 10 micron spaced grooves (in the central area), smaller in size than a fibroblast, which lead the cells to align in the direction of the grooves.

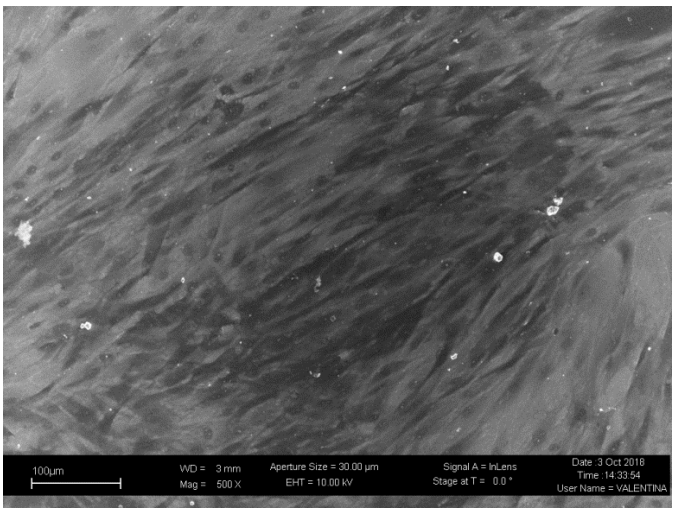


***Fig.7.11*** *EB30_HGF*

Alignment is less marked for sample EB30 (Fig.7.11), which has 30micron spaced grooves, so being larger, cells are less affected.

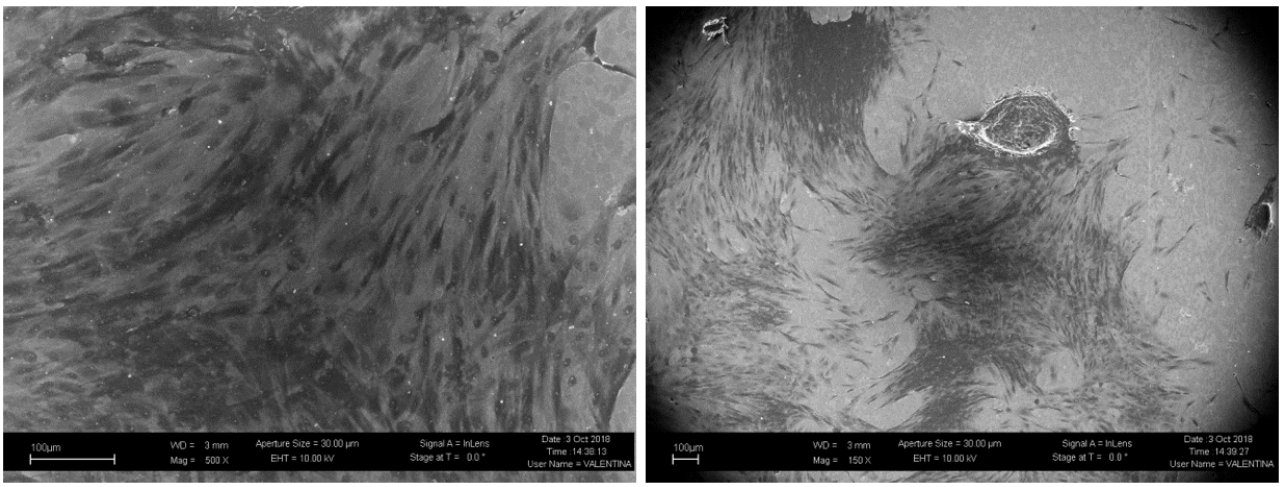


***Fig.7.12*** *EB10HT_HGF*

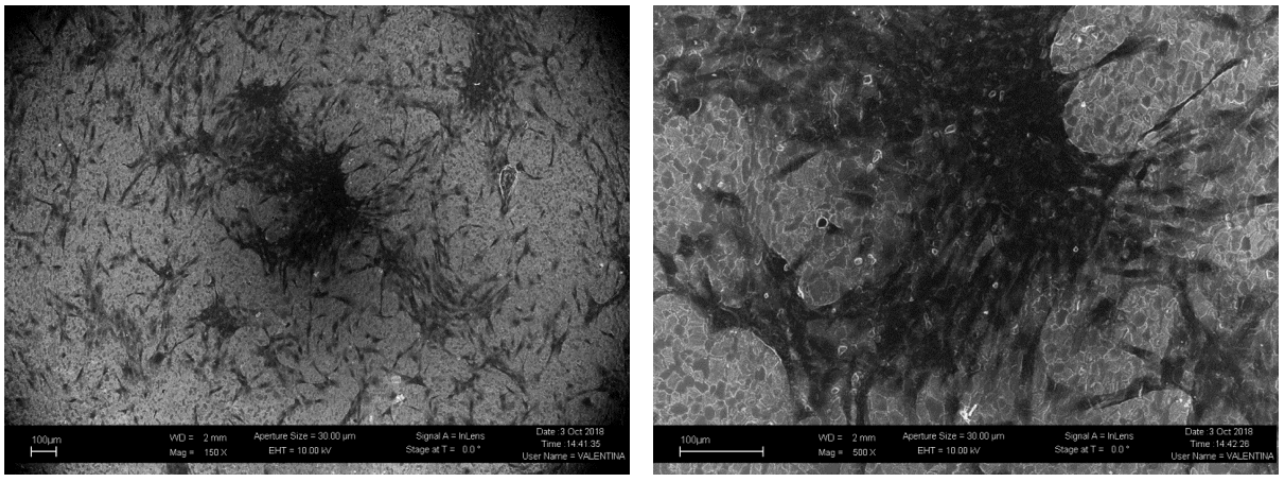


***Fig.7.13*** *EB10HTETCH_HGF*

In the case of EB10HT (Fig.7.12) and EB10HTETCH (Fig.7.13) samples, the cells are not uniformly distributed on the surfaces and it is quite difficult to observe a preferential direction.

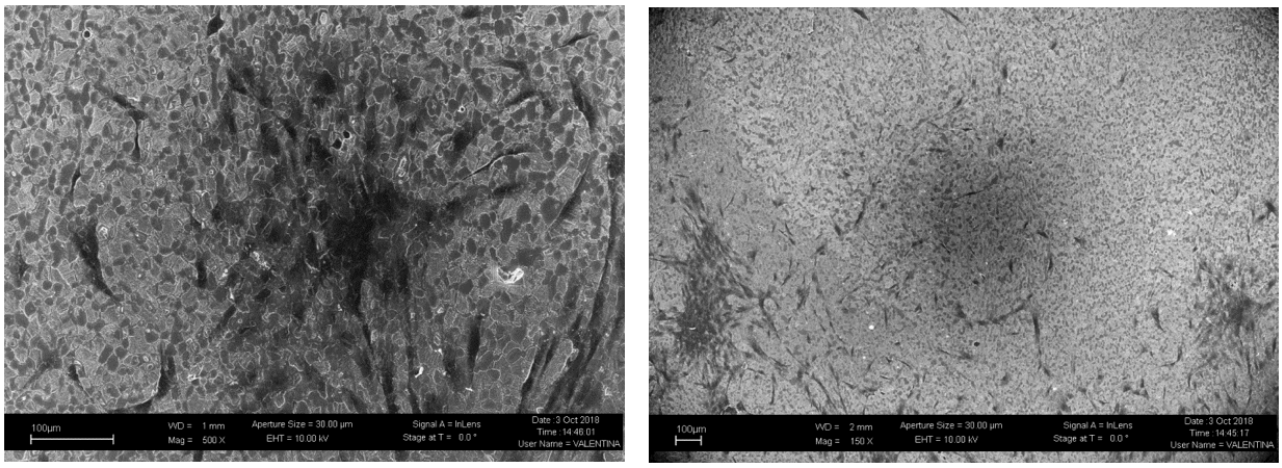


***Fig.7.14*** *P10_HGF*

The sample P10 (Fig.7.14) prepared for SEM, presents too few cells on the polished part of the surface, so it is not possible to observe some kind of alignment.

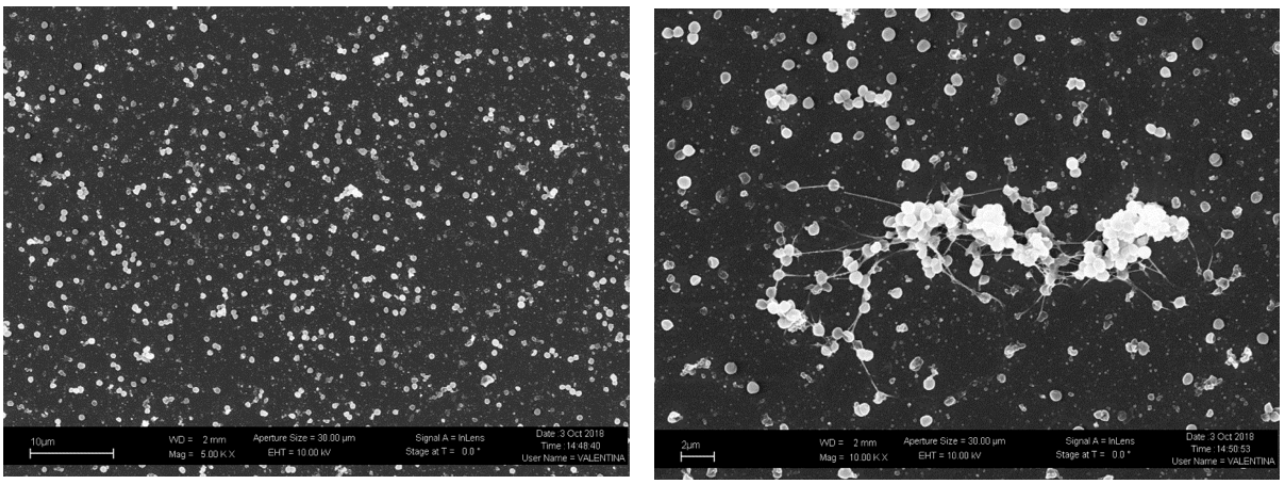


***Fig.7.15*** *MP_S.aureus*

The surface of the MP sample (Fig.7.15), 48 hours after culture, is largely colonized by the bacteria. It is also possible to observe the formation of bacterial aggregates and biofilms (Fig.7.15, right).

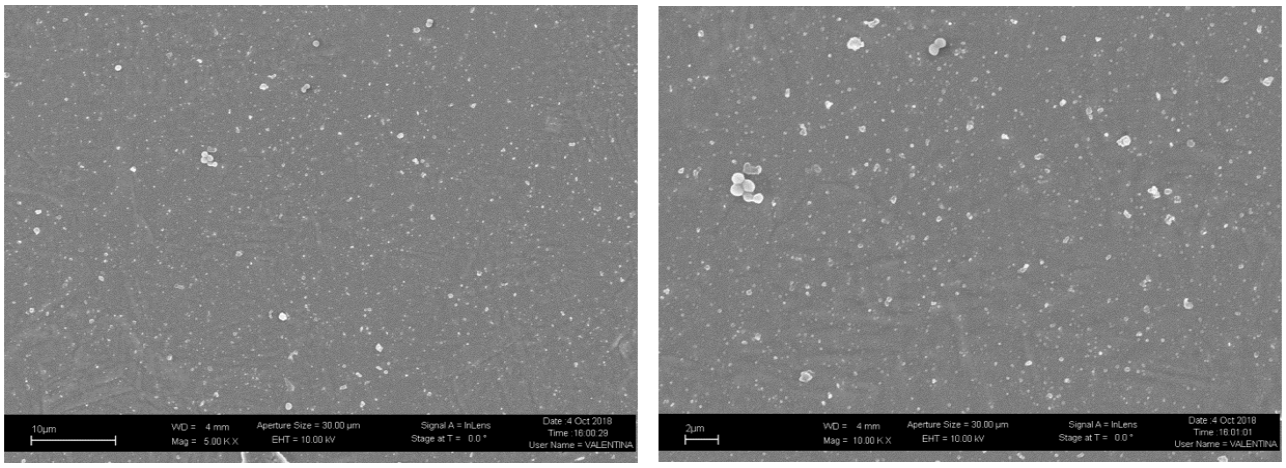


***Fig.7.16*** *EB10_S.aureus*

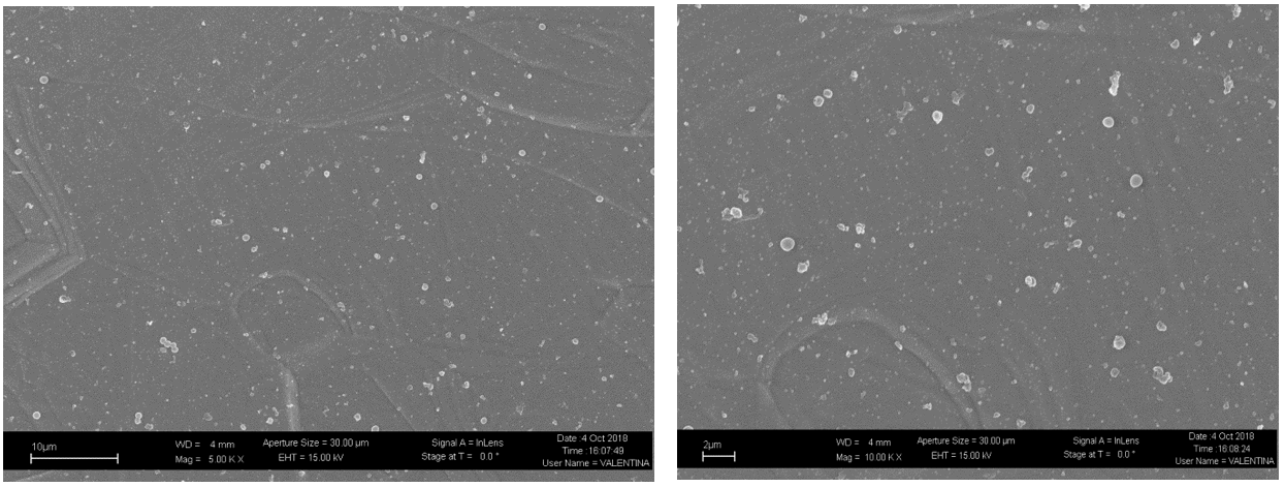


***Fig.7.17*** *EB30_S.aureus*

The surfaces EB10 and EB30, actually are less colonized by bacteria than all the others. The thermally treated (EB10HT), and polished (P10 and P30) samples prepared for SEM are probably contaminated or not well prepared and their observation is not significant.

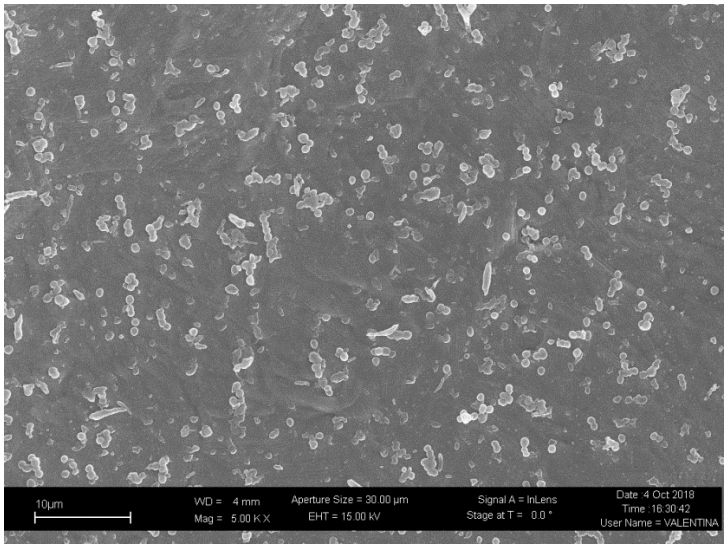


***Fig.7.18*** *EB10HT_S.aureus*

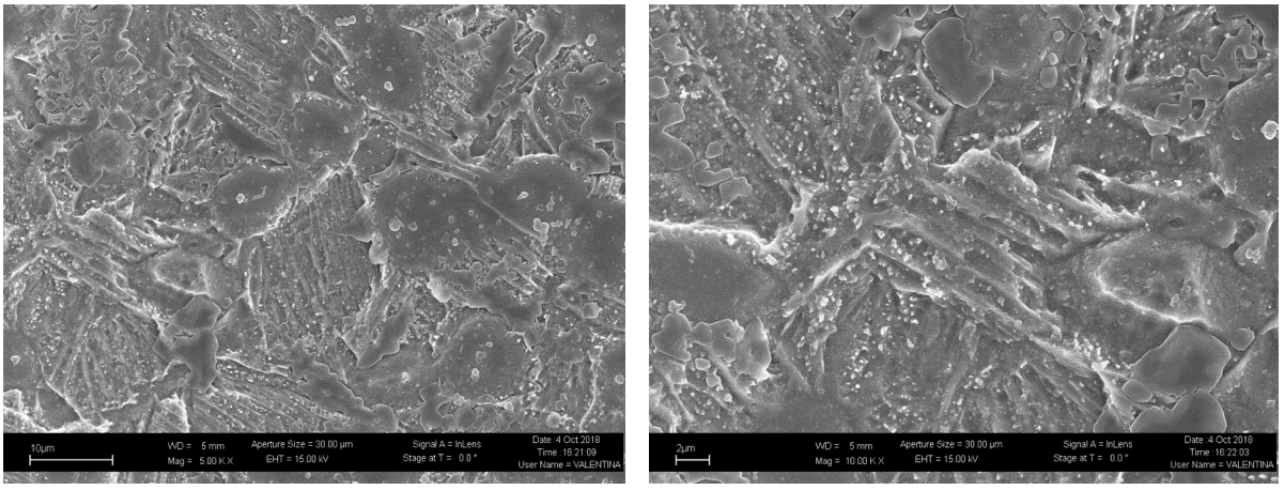


***Fig.7.19*** *EB10HTETCH_S.aureus*

From Fig.7.19, it seems that the etched surface follows the trend of CFU results. It is not very colonized by bacteria and has relatively round structures that are probably residues deriving from biological tests.

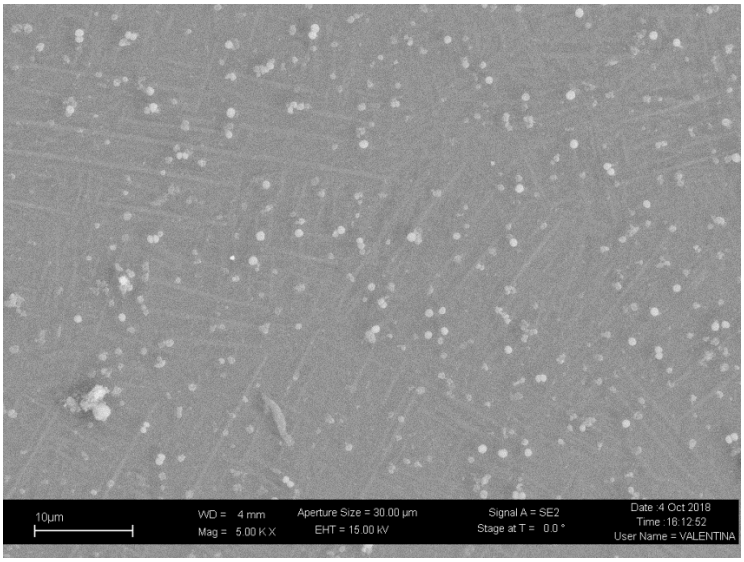


***Fig.7.20*** *P10_S.aureus*

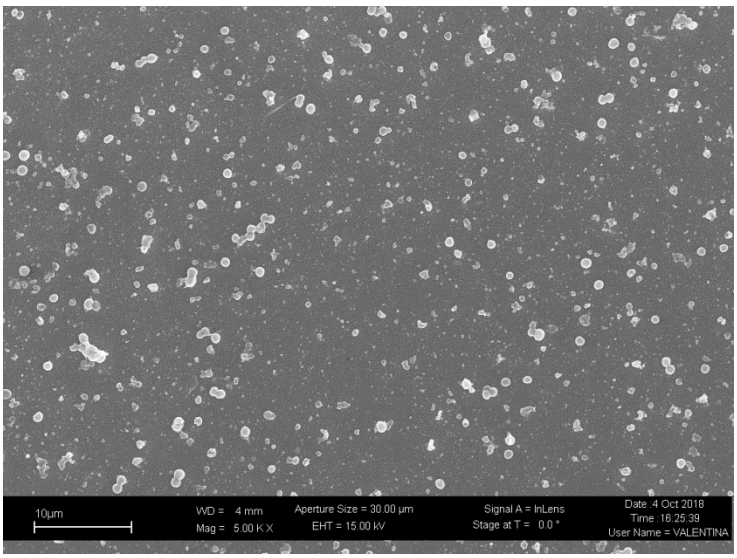


***Fig.7.21*** *P30_S.aureus*

The surfaces P10 and P30 (Fig.7.20 and Fig.7.21) show a decrease in the number of bacteria compared to the MP control surface, in particular the poor attachment to the P10 surface led to think that the bacteria can be sensitive to structure and microstructure of the surface.

## CONCLUSIONS

In the present research, 5, 10 and 30µm spaced grooves were produced on Ti6Al4V alloy, 5 and 10µm on Ti15Mo alloy and 10µm on Ti grade 2, by means of Electron Beam Structuring. It was not possible to observe the micro topography characterized by 5µm grooves on Ti6Al4V, while it was slightly visible on Ti15Mo. The 10 and 30µm spaced grooves were more noticeable, however in some cases grooves spacing was not uniform.

On some of these samples, heat treatments were carried out to obtain different crystalline structures or microstructures on the surface. After that, the etching treatments, aimed at putting grain boundaries and microstructure in evidence, and a final polishing treatment, aimed at removing the structured part of the surface, maintaining the crystalline structure and microstructure produced by the electron beam, were evaluated. The thermal treatments were carried out on Ti6Al4V, Ti15Mo and Tigrade 2, but a particular attention was paid on Ti6Al4V. The other two treatments were performed only on Ti6Al4V.

The Ti6Al4V samples were characterized by different techniques. Using the SEM and LOM it was possible to observe the presence of the grooves as well as the development of characteristic microstructures upon EB structuring, thermal and etching treatments.

The contact profiler has provided roughness values that are greater in the case of the sample treated with etching (higher value: 0, 42µm) and lower in the case of mirror polished samples (lowest value for MP sample: 0.06µm). EB10 and EB30 samples present a roughness values of 0,35µm and 0,26µm respectively. EB30 and P10 samples have a roughness values similar than the maximum value to avoid bacterial adhesion (0,2µm); EB10, HT10 and HT10ETCH have greater values than 0,2µm, while MP sample was the only one that presents a smaller values.

With the 2D and 3D reconstruction images, using an optical profiler, these differences in roughness can be observed.

The values obtained through the contact angle technique are in accordance with those found in literature for titanium alloys, so that the surfaces are slightly hydrophilic and no significant alterations are induced by EB structuring (74-81°).

The XRD technique made it possible to identify the crystalline phases of the samples. The presence of hexagonal titanium in all the samples was reported. EB structuring induces the presence of martensite that is remove by the thermal treatments. In Ti6AL4V with heat treatment at 1030°C

(HT10), and in the mirror polished (MP) spectrum, there is a small peak, next to the main one, which demonstrates the presence of cubic titanium (beta phase).

Finally cellular and bacterial tests carried out, show interesting results.
After three days of culture on the different substrates, the cells show good cell viability values, except for the sample treated with etching probably because of the rough and sharp surface profile of this sample.
As for bacteria, reduced adhesion was observed especially in the first 48 hours in all of the treated samples, compared with the mirror polished control. Furthermore, reduction of bacterial adhesion is conserved or even reduced on structured and polished surfaces, compared to the just structured ones, which leads to the belief that bacterial adhesion is actually influenced by the surface microstructure and not by the presence of the grooves.The presence of a low amount of bacteria even on the EB structured and then heat treated sample excluded a relevant influnce of the presence of martensite on bacterial adhesion. All the samples characterized by a high density of sub-grains show a reduced bacterial adhesion, making a connection between microstructure and biofilm formation.
These aspects should be further investigated.

As regards the morphology, the cells generally show good alignment on the samples characterized by the grooves, while they are not aligned on the mirror-polished sample.
In particular, the cells result aligned in EB10, while they are less aligned in EB30 because of the large dimension of the groove with respect to fibroblasts. They are not aligned on MP and P10 samples, confirming the absence of patterns able to promote the guidance phenomenon.

## BIBLIOGRAPHY


[1] D.F.Williams, "Definition in biomaterials: proceeding of a consensus conference of the Europeam Society for Biomaterials", vol. 4, Chester: Elsevier Science Ltd, 1987.

[2] F. J.O'Brien, "Biomaterials & scaffolds for tissue engineering," *Materialstoday,* vol. 14, pp. 88-95, march 2011.

[3] B. Ratner, A. Hoffman, F. Schoen and G. Lemmons, Biomaterials science, an introduction to materials in medicine, 3 ed., Elsevier inc., 2013.

[4] "Overview of Biomaterials and Their Use in Medical Devices," in *Handbook of Materials for Medical Devices*, ASM International, 2003.

[5] A. International, Overview of Biomaterials and Their Use in Medical Devices, vol. 1, 2003.

[6] J. Park, "Biomaterials: Introduction. In The Biomedical Engineering Handbook," vol. 1, CRC Press: Boca Raton, FL, USA, 2000, p. IV1–IV8.

[7] T. Hanawa, "Recent development of new alloys for biomedical use.," *Mater. Sci Forum,* vol. 512, p. 243–248, 2006.

[8] C.Ramskogler, "Surface modification of titanium alloys for orthopaedic implants," 2018.

[9] M. Long and H. Rack, "Titanium alloys in total joint replacement—A materials science perspective," *Biomaterials,* vol. 19, p. 1621–1639., 1998.

[10] K. Wang, "The use of titanium for medical applications in the USA.," *Mater Sci Eng.,* vol. 213, p. 134–137, A 1996.

[11] G. Lütjering and J. Williams, Titanium, 2nd ed., Springer: Berlin, Germany, 2003, p. 20–22.

[12] M. P. C. Leyens, Titanium and Titanium Alloys, John Wiley & Sons, 2003.

[13] Y. Oshida, Bioscience and Bioengineering of Titanium Materials, 2nd ed., Elsevier, 2013.

[14] H. Rack and J. Qazi, "Titanium alloys for biomedical applications," *Materials Science and Engineering,* 2005.

[15] [Online]. Available: http://www.arcam.com/wp-content/uploads/Arcam-Titanium-Grade-2.pdf.

[16] Niinomi and Mitsuo, "Mechanical properties of biomedical titanium alloys," *Materials Science and Engineering ,* 1998.

[17] F. Gil, M. Ginebra, J. Manero and J. Planell, "Formation of a-Widmansta¨tten structure: effects of grain size and cooling rate on the Widmansta¨tten morphologies and on the mechanical properties in Ti6Al4V alloy," *Journal of Alloys and Compounds,* vol. 329, p. 142–152, 2001.

[18] "Titanium & its Alloys," in *Materials Science & Metallurgy*.

[19] W. Mei and J. Sun, "Martensitic transformation from β to α′ and α″ phases in Ti–V alloys: A firstprinciples study," *Journal of Materials Research,* 2017.

[20] J. Zhang, C. Tasan, M. Lai, A.-C. Dippel and D. Raabe, "Complexion-mediated martensitic phase transformation in Titanium," *Nature Communications,* vol. 8, 2017.

[21] X. Liu, P. K. Chu and C. Ding, "Surface modification of titanium, titanium alloys, and related materials for biomedical applications," *Materials Science and Engineering,* vol. 47, p. 49–121, 2004.

[22] M. Kulkarni, A. Mazare, P. Schmuki and A. Iglic, "Biomaterial surface modification of titanium and titanium alloys for medical applications.," *Nanomedicine,* p. 111–136., 2014.

[23] C. Ramskogler, F. Warchomicka, S. Mostofi, W. Annelie and C. Sommitsch, "Innovative surface modification of Ti6Al4V alloy by electron beam technique for biomedical application," *Materials Science and Engineering C,* vol. 78, pp. 105-113, 2017.

[24] G. Camera, S. Spriano and S. Ferraris, *Surface structuring of a titanium alloy for contact with soft tissues,* 2018.

[25] J. Cox, A. Eisenberg and R. Lennox., "Patterned surfaces via self assembly.," *Curr Opin Colloid Interface Sci,* vol. 4, 1999.

[26] M. Sato and T. Webster, "Nanobiotechnology: implications for the future of nanotechnology in orthopedic applications," *Expert Rev Med Dev,* vol. 1, p. 105–14, 2004.

[27] K. Anselme, "Osteoblast adhesion on biomaterials.," *Biomaterials,* vol. 21, p. 667–81, 2000.

[28] C. Yang-Tse and D. Rodak, "Is the lotus leaf superhydrophobic.," *Appl Phys Lett,* vol. 86, 2005.

[29] E. Martines, K. Seunarine, H. Morgan, N. Gadegaard and C. Wilkinson, "Superhydrophobicity and superhydrophilicity of regular nanopatterns.," *Nano Lett,* vol. 5, p. 2091–103, 2005.

[30] B. Bhushan, D. Tokachichu, M. Keener and S. Lee, "Nanoscale adhesion, friction and wear suited of biomolecules on silicon based surfaces.," *Acta Biomater,* vol. 2, p. 39–49., 2005.

[31] J. Guck, F. Lautenschlager, S. Paschke and M. Beil, "Critical review: cellular mecha nobiology and amoeboid migration.," *Integr Biol (Camb),* vol. 2, p. 575e83, 2010.

[32] S. Goodman, P. Sims and R. Albrecht, "Three-dimensional extracellular matrix textured biomaterials.," *Biomaterials,* vol. 17, p. 2087e95., 1996.

[33] G. Abrams, S. Goodman, P. Nealey, M. Franco and C. Murphy, "Nanoscale topography of the basement membrane underlying the corneal epithelium of the rhesus macaque.," *Cell Tissue Res,* vol. 299, p. 39e46, 2000.

[34] E. Pamula, V. D. Cupere, Y. Dufrene and P. Rouxhet, "Nanoscale organization of adsorbed collagen: influence of substrate hydrophobicity and adsorption time.," *J Colloid Interface Sci,* vol. 271, p. 80e91, 2004.

[35] P. Rorth, "Whence directionality: guidance mechanisms in solitary and collective cell migration.," *Dev Cell,* vol. 20, p. 9e18, 2011.

[36] E. Dent and F. Gertler, "Cytoskeletal dynamics and transport in growth cone motility and axon guidance.," *Neuron,* vol. 40, p. 209e27., 2003.

[37] K. Wolf, R. Muller, S. Borgmann, E. Brocker and P. Friedl, "Amoeboid shape change and contact guidance: T-lymphocyte crawling through fibrillar collagen is independent of matrix remodeling by MMPs and other proteases.," *Blood,* vol. 102, 2003.

[38] P. Friedl., "Prespecification and plasticity: shifting mechanisms of cell migration.," *Curr Opin Cell Bio,* vol. 16, p. 14e23, 2004.

[39] H. Haga, C. Irahara, R. Kobayashi, T. Nakagaki and K. Kawabata, "Collective movement of epithelial cells on a collagen gel substrate.," *Biophys J,* vol. 88, p. 2250e6., 2005.

[40] U. Schwarz and I. Bischofs, "Physical determinants of cell organization in soft media.," *Med Eng Phys,* vol. 27, p. 763e72., 2005.

[41] A. VanDer Flier and A. Sonnenberg, "Function and interactions of integrins.," *Cell Tissue Res,* vol. 305, 2001.

[42] E. Tzima, M. Irani-Tehrani, W. Kiosses, E. Dejana, D. Schultz and B. Engelhardt, "A mechanosensory complex that mediates the endothelial cell response to fluid shear stress.," *Nature,* vol. 437, p. 426e31., 2005.

[43] K. Hayakawa, H. Tatsumi and M. Sokabe, "Actin stress fibers transmit and focus force to activate mechanosensitive channels.," *J Cell Sci,* vol. 121, p. 496e503., 2008.

[44] G. Giannone and M. Sheetz, "Substrate rigidity and force define form through tyrosine phosphatase and kinase pathways.," *Trends Cell Biol,* vol. 16, p. 213e23, 2006.

[45] C. DuFort, M. Paszek and V. Weaver, "Balancing forces: architectural control of mechanotransduction.," *Nat Rev Mol Cell Biol,* vol. 12, p. 308e19., 2011.

[46] D. Riveline, E. Zamir, N. Balaban, U. Schwarz, T. Ishizaki and S. Narumiya, "Focal contacts as mechanosensors: externally applied local mechanical force induces growth of focal contacts by an mDia1-dependent and ROCK independent mechanism.," *J Cell Biol,* vol. 153, p. 1175e85, 2001.

[47] D. Discher, P. Janmey and Y. Wang, "Tissue cells feel and respond to the stiffness of their substrate.," *Science,* vol. 310, p. 1139e43., 2005.

[48] D. Ingber, "Tensegrity: the architectural basis of cellular mechano transduction.," *Annu Rev Physiol,* vol. 59, p. 575e99, 1997.

[49] A. Rajnicek, S. Britland and C. McCaig, "Contact guidance of CNS neurites on grooved quartz: influence of groove dimensions, neuronal age and cell type.," *J Cell Sci,* vol. 110, p. 2905e13, 1997.

[50] N. Karuri, P. Nealey, C. Murphy and R. Albrecht, "Structural organization of the cytoskeleton in SV40 human corneal epithelial cells cultured on nano and microscale grooves.," *Microsc Microanal,* vol. 30, p. 405e13, 2008.

[51] A. Teixeira, G. Abrams, P. Bertics, C. Murphy and P. Nealey, "Epithelial contact guidance on well-defined micro- and nanostructured substrates.," *J Cell Sci,* vol. 116, 2003.

[52] A. Ridley, M. Schwartz, K. Burridge, R. Firtel, M. Ginsberg, G. Borisy and a. et, "Cell migration: integrating signals from front to back.," *Science,* vol. 302, p. 1704e9., 2003.

[53] R. Petrie, A. Doyle and K. Yamada, "Random versus directionally persistent cell migration.," *Nat Rev Mol Cell Biol,* vol. 10, p. 538e49, 2009.

[54] S. Li, S. Bhatia, Y. Hu, Y. Shin, Y. Li and S. Usami, "Effects of morphological patterning on endothelial cell migration.," *Biorheology,* vol. 38, p. 101e8., 2001.

[55] J. Kaiser, A. Reinmann and A. Bruinink, "The effect of topographic characteristics on cell migration velocity.," *Biomaterials,* vol. 27, p. 5230e41., 2006.

[56] E. Cavalcanti-Adam, A. Micoulet, J. Blümmel, J. Auernheimer, H. Kessler and P. S. Joachim, "Lateral spacing of integrin ligands influences cell spreading and focal adhesion assembly.," *Eur J Cell Biol,* vol. 85, p. 219–24., 2006.

[57] D. McClay, "The role of thin filopodia in motility and morphogenesis.," *Exp Cell Res,* vol. 253, p. 296–301., 1999.

[58] S. Fujita, M. Ohshima and I. H., "Time-lapse observation of cell alignment on nanogrooved patterns.," *Soc Interface,* vol. 6, p. 269–77, 2009.

[59] M. Dalby, "Topographically induced direct cell mechanotransduction.," *Med Eng Phys,* vol. 27, p. 730–42, 2005.

[60] M. Dalby, M. Riehle, D. Sutherland, H. Agheli and A. Curtis, "Use of nanotopography to study mechanotransduction in fibroblasts – methods and perspectives.," *Eur J Cell Biol,* vol. 83, p. 159–69., 2004.

[61] M. Dalby, M. Biggs, N. Gadegaard, G. Kalna, C. Wilkinson and A. Curtis, "Nanotopographical stimulation of mechanotransduction and changes in interphase centromere positioning.," *J Cell Biochem,* vol. 100, p. 326–38, 2007.

[62] M. Dalby, D. Pasqui and S. Affrossman, "Cell response to nano-islands produced by polymer demixing: a brief review.," *IEEE Proc Nanobiotechnol,* vol. 151, p. 53–61, 2004.

[63] M. Dalby, M. Riehle, H. Johnstone, S. Affrossman and A. Curtis, "Investigating the limits of filopodial sensing: a brief report using SEM to image the interaction between 10 nm high nano-topography and fibroblast filopodia.," *Cell Biol Int,* vol. 28, p. 229–36, 2004.

[64] M. Dalby, M. Riehle, D. Sutherland, H. Agheli and A. Curtis, "Fibroblast response to a controlled nanoenvironment produced by colloidal lithography.," *J Biomed Mater Res A,* vol. 69, p. 314–22, 2004.

[65] M. Dalby, M. Riehle, D. Sutherland, H. Agheli and A. Curtis, "Changes in fibroblast morphology in response to nano-columns produced by colloidal lithography.," *Biomaterials,* vol. 25, p. 5415–22, 2004.

[66] S. Oh, K. Brammer, Y. Li, D. Teng, A. Engler and S. Chien, "Stem cell fate dictated solely by altered nanotube dimension.," *Proc Natl Acad Sci USA,* vol. 106, p. 2130–5, 2009.

[67] K. Brammer, S. Oh, C. Cobb, L. Bjursten, H. VanDer Heyde and S. Jin, "Improved bone-forming functionality on diameter-controlled TiO2 nanotube surface.," *Acta Biomater,* vol. 5, p. 3215–23., 2009.

[68] M. Dalby, D. McCloy, M. Robertson, H. Agheli, D. Sutherland and S. Affrossman, "Osteoprogenitor response to semi-ordered and random nanotopographies.," *Biomaterials,* vol. 27, p. 2980–7, 2006.

[69] M. Arnold, E. Cavalcanti-Adam, R. Glass, J. Blümmel, W. Eck and M. Kantlehner, "Activation of integrin function by nanopatterned adhesive interfaces.," *Chem Phys Chem,* vol. 5, p. 383–8, 2004.

[70] T. Kunzler, C. Huwiler, T. Drobek, J. Voros and N. Spencer, "Systematic study of osteoblast response to nanotopography by means of nanoparticle-density gradients.," *Biomaterials,* vol. 28, p. 5000–6, 2007.

[71] M. Bigerelle, K. Anselme, B. Noël, I. Ruderman, P. Hardouin and A. Lost, "Improvement in the morphology of surfaces for cell adhesion: a new process to double human osteoblast adhesion on Ti-based substrates.," *Biomaterials,* vol. 23, p. 1563–77, 2002;.

[72] S. Buttiglieri, D. Pasqui, M. Migliori, H. Johnstone, S. Affrossman and L. Sereni, "Endothelization and adherence of leucocytes to nanostructured surfaces," *Biomaterials,* vol. 24, p. 2731–8, 2003.

[73] K. Kwon, S. Choi, S. Lee, B. Kim, S. Lee and M. Park, "Label-free, microfluidic separation and enrichment of human breast cancer cells by adhesion difference.," *Lab Chip,* vol. 7, p. 1461–8, 2007.

[74] D. Lehnert, B. Wehrle-Haller, C. David, U. Weiland, C. Ballestrem and B. Imhof, "Cell behaviour on micropatterned substrata: limits of extracellular matrix geometry for spreading and adhesion.," *J Cell Sci,* vol. 117, p. 41–52, 2004.

[75] J. Slater and W. Frey, "Nanopatterning of fibronectin and the influence of integrin clustering on endothelial cell spreading and proliferation.," *J Biomed Mater Res,* vol. 87A, p. 176–85, 2008.

[76] C. Oakley and D. Brunette, "The sequence of alignment of microtubules, focal contacts and actin-filaments in fibroblasts spreading on smooth and grooved titanium substrata.," *Cell Sci,* vol. 106, p. 343e54., 1993.

[77] E. Eisenbarth, J. Meyle, J. Breme and W. Nachtigall, "Influence of the surface structure of titanium materials on the adhesion of fibroblasts," *Biomaterials,* 1996.

[78] X. Wang, T. Lu, J. Wen, L. Xu, D. Zeng, Q. Wu, L. Cao, S. Lin, X. Liu and X. Jiang, "Selective responses of human gingival fibroblasts and bacteria on carbon fiber reinforced polyetheretherketone with multilevel nanostructured TiO2," *Biomaterials,* 2016.

[79] A. Varesano, S. Ferraris, F. Giachet Truffa, M. Miola, E. Bertone, C. Vineis, A. Cochis, R. Sorrentino, S. Spriano and L. Rimondini, "Nanogrooves and keratin nanofibers on titanium

surfaces aimed at driving gingival fibroblasts alignment and proliferation without increasing bacterial adhesion," *Materials Science and Engineering C,* 2017.

[80] X. Jian, W. Huang, D. Wu, D. You, Z. Lin and J. Chen, "Effect of Fibronectin-Coated Micro-Grooved Titanium Surface on Alignment, Adhesion, and Proliferation of Human Gingival Fibroblasts," *medical science,* 2017.

[81] S. SPRIANO and S. FERRARIS, "How can topographical surface features affect the interaction of implants with soft tissues?".

[82] M. T. Madigan and J. M. Martinko, Brock Biology of Microorganisms, 11 ed., Pearson Prentice Hall, 2006.

[83] S. Srivastava and P. Srivastava, "Understanding bacteria.," *Dordrecht: Kluwer Academic,* 2003.

[84] T. Proft and E. Baker, "Pili in Gram-negative and Gram-positive bacteria – structure, assembly and their role in disease.," *Cell Mol Life Sci,* vol. 66, p. 613–35, 2009.

[85] B. Smets, D. Grasso, M. Engwall and B. Machinist, "Surface physicochemical properties of Pseudomonas fluorescens and impact on adhesion and transport through porous media.," *Colloids Surf B Biointerfaces,* vol. 14, p. 121–39, 1999.

[86] M. Missirlis and Y. Katsikogianni, "Concise review of mechanisms of bacterial adhesion to biomaterials and of techniques used in estimating bacteria-material interactions," *European Cells and Materials,* vol. 8, pp. 37-57, 2004.

[87] J. Costerton, "Introduction to biofilm," *Int J Antimicrob Agents,* vol. 11, p. 217–21, 1999.

[88] L. Ploux, A. Ponche and K. Anselme, "Bacteria/material interfaces: role of the material and cell wall properties.," *J Adhesion Sci Technol.*

[89] S. Branda, A. Vik, L. Friedman and R. Kolter, "Biofilms: the matrix revisited.," *Trends Microbiol,* vol. 13, p. 20–6, 2005.

[90] D. Seyer, P. Cosette, A. Siroy, E. De, C. Lenz and H. Vaudry, "Proteomic comparison of outer membrane protein patternis of sessile and planktonic Pseudomonas aeruginosa cells.," *Biofilms,* vol. 2, p. 27–36, 2005.

[91] [Online]. Available: https://www.fxmedicine.com.au/blog-post/nac-persistent-infections.

[92] J. Otto, J. Norbeck, T. Larsson, K. Karlsson and M. Hermansson, "Adhesion of type 1-fimbriated Escherichia coli to abiotic surfaces leads to altered composition of outer membrane proteins.," *J Bacteriol,* vol. 183, p. 2445–53, 2001.

[93] C. Prigent-Combaret, O. Vidal, C. Dorel and P. Lejeune, "Abiotic surface sensing and biofilm-dependent regulation of gene expression in Escherichia coli.," *J Bacteriol,* vol. 181, p. 5993–6002, 1999.

[94] R. Van Houdt and C. Michiels, "Role of bacterial cell surface structures in Escherichia coli biofilm formation.," *Res Microbiol,* vol. 156, p. 626–33, 2005.

[95] W. Teughels, N. Van Assche, I. Sliepen and M. Quirynen, "Effect of material characteristics and/or surface topography on biofilm development.," *ClinOral Implants Res,* vol. 17, p. 68–81., 2006.

[96] W. Characklis, "Fouling biofilm development: a process analysis.," *Biotechnol Bioeng;,* vol. 23, p. 1923–60, 1981.

[97] K. Whitehead, J. Colligon and J. Verran, "Retention of microbial cells in substratum surface features of micrometer and sub-micrometer dimensions.," *Colloids Surf B Biointerfaces,* vol. 41, p. 129–38, 2005.

[98] D. Campoccia, L. Montanaro, H. Agheli, D. Sutherland, V. Pirini and M. Donati, "Study of Staphylococcus aureus adhesion on a novel nanostructured surface by chemiluminometry.," *Int J Artif Organs,* vol. 29, p. 622–9, 2006.

[99] N. Mitik-Dineva, J. Wang, V. Truong, P. Stoddart, F. Malherbe and R. Crawford, "Differences in colonisation of five marine bacteria on two types of glass surfaces.," *Biofouling,* vol. 25, p. 621–31, 2009.

[100] S. Puckett, E. Taylor, T. Raimondo and T. Webster, "The relationship between the nanostructure of titanium surfaces and bacterial attachment.," *Biomaterials,* vol. 31, p. 706–13, 2010.

[101] B. DelCurto, M. Brunella, C. Giordano, M. Pedeferri, V. Valtulina and L. Visai, "Decreased bacterial adhesion to surface-treated titanium," *Int J Artif Organs,* vol. 28, pp. 718-730, 2005.

[102] B. Yang, M. Uchida, H. Kim, X. Zhang and T. Kokubo, "Preparation of bioactive titanium metal via anodic oxidation treatment," *Biomaterials,* vol. 25, pp. 1003-1010, 2004.

[103] K. Sreekumari, K. Nandakumar and Y. Kikuchi, "Bacterial attachment to stainless steel welds: Significance of substratum microstructure," *Biofouling,* 2001.

[104] V. Truong, R. Lapovok, Y. Estrin, S. Rundell, J. Wang, C. J. Fluke, R. Crawford and E. Ivanova, "The influence of nano-scale surface roughness on bacterial adhesion to ultrafine-grained titanium," *Biomaterials,* 2010.

[105] C. Ramskogler, F. Warchomicka, S. Mostofi, A. Weinberg and C. Sommitsch, "Innovative surface modification of Ti6Al4V alloy by electron beam technique for biomedical application," *Materials Science and Engineering C,* 2017.

[106] Schultz, Electron Beam Welding, Abington Publishing Cambridge England, 2004.

[107] G. Schubert, "Electron Beam Welding," 2008.

[108] B. Dance and A. Buxton, "An introduction to Sur -Sculpt R technology - new opportunities, new challenges.," in *7th International Conference on Beam Technology*, 2007.

[109] R. M. Chemcut and C. Corporation, "Etching Titanium with HF and Nitric Acid Solutions Part 1".

[110] J. D. Stokes, Principles and Practice of Variable Pressure Environmental Scanning Electron Microscopy (VP-ESEM)., Chichester: John Wiley & Sons., 2008.

[111] [Online]. Available: http://emicroscope.blogspot.com/2011/03/scanning-electron-microscope-sem-how-it.html?view=snapshot.

[112] [Online]. Available: http://www.vcbio.science.ru.nl/public/pdf/fesem_info_eng.pdf.

[113] [Online]. Available: https://en.wikipedia.org/wiki/Optical_microscope#Lighting_techniques.

[114] [Online]. Available: https://www.edmundoptics.com/resources/application-notes/microscopy/optical-microscopy-application-darkfield-illumination/.

[115] [Online]. Available: https://en.wikipedia.org/wiki/Surface_roughness.

[116] [Online]. Available: http://www.rubert.co.uk/faqs/roughness-parameters/.

[117] [Online]. Available: https://en.wikipedia.org/wiki/Contact_angle.

[118] [Online]. Available: https://www.biolinscientific.com/measurements/contact-angle.

[119] [Online]. Available: https://www.stresstech.com/en-fi/products/x-ray-diffraction-equipment/x-ray-diffraction/.